KYUSHU INSTITUTE OF TECHNOLOGY

EXPERIMENTAL INVESTIGATION ON SILICA DUST LOFTING IN THE VACUUM CHAMBER AND PREDICTIONS OF LUNAR DUST HEIGHTS DUE TO CHARGING WITHIN MICRO-CAVITIES AND SURFACE ELECTRIC FIELD

DOCTORAL DISSERTATION

NECMI CIHAN ORGER

DEPARTMENT OF ELECTRICAL AND ELECTRONIC ENGINEERING

JULY 2018

KYUSHU INSTITUTE OF TECHNOLOGY

EXPERIMENTAL INVESTIGATION ON SILICA DUST LOFTING IN THE VACUUM CHAMBER AND PREDICTIONS OF LUNAR DUST HEIGHTS DUE TO CHARGING WITHIN MICRO-CAVITIES AND SURFACE ELECTRIC FIELD

DOCTORAL DISSERTATION

NECMI CIHAN ORGER
15595502

DEPARTMENT OF ELECTRICAL AND ELECTRONIC ENGINEERING

Thesis Advisor: Assoc. Prof. Kazuhiro Toyoda

JULY 2018

To my family and friends for always being there for me,

TABLE OF CONTENTS

Page

ABBREVIATIONS

CZL : Coronal and Zodiacal Light
IMF : Interplanetary Magnetic Field
LHG : Lunar Horizon Glow
MHD : Magnetohydrodynamics
ODE : Ordinary Differential Equation
SW : Solar Wind
VDF : Velocity Distribution Function

LIST OF SYMBOLS

Symbol	Description	Units
a	Dust radius	m
C	Capacitance of a dust particle	$A^2\ s^4\ kg^{-1}\ m^{-2}$
δ_m	Maximum secondary electron emission yield	-
δt	Time step	s
e	Electron charge	C
ε_0	Vacuum permittivity	$A^2\ s^4\ kg^{-1}\ m^{-3}$
E_0	Surface electric field	$V\ m^{-1}$
η	Enhanced charging number	-
ϕ_s	Surface potential	V
$F_{contact}$	Contact force	N
$F_{Coulomb}$	Coulomb force between charged dust grains	N
F_{EF}	Electrostatic force by surface electric field	N
$F_{gravity}$	Gravity force	N
g_{lunar}	Lunar gravity	$m\ s^{-2}$
I_e	Solar wind electron current	A
I_i	Solar wind ion current	A
I_{ph}	Photoemission electron current	A
I_{sec}	Secondary electron emission current	A
J_e	Solar wind electron current density	$A\ m^{-2}$
J_i	Solar wind ion current density	$A\ m^{-2}$
J_{ph}	Photoemission electron current density	$A\ m^{-2}$
J_{sec}	Secondary electron emission current density	$A\ m^{-2}$
k_B	Boltzmann constant	$m^2\ kg\ s^{-2}\ K^{-1}$
m_{dust}	Mass of a dust grain	kg
m_e	Electron mass	kg
m_i	Ion mass	kg
n_0	Plasma density	m^{-3}
n_h	Number of height observations	-
n_v	Number of velocity observations	-
$Q_{dust\_initial}$	Initial charge of a detached dust grain	C
$Q_{microcavity}$	Accumulated charge on a patch surface	C
$Q_{top\_surface}$	Collected charge from primary electrons	C
ρ_{dust}	Dust density	$kg\ m^{-3}$
s	Microcavity size	m
S	Surface cleanliness	-

θ_{DZ}	Dead zone location	rad
T_{ee}	Emitted electron temperature	eV
T_e	Solar Wind electron temperature	eV
T_i	Solar Wind ion tempterature	eV
T_{ph}	Photoemitted electron temperature	eV
T_{sec}	Secondary electron temperature	eV
v_{0z}	Initial vertical launching velocity	m s^{-1}
V_{the}	Thermal velocity of electrons	m s^{-1}
V_{thi}	Thermal velocity of ions	m s^{-1}
V_{SW}	Solar wind bulk velocity	m s^{-1}

LIST OF TABLES

Page

LIST OF FIGURES

Page

EXPERIMENTAL INVESTIGATION ON SILICA DUST LOFTING IN THE VACUUM CHAMBER AND PREDICTIONS OF LUNAR DUST HEIGHTS DUE TO CHARGING WITHIN MICRO-CAVITIES AND SURFACE ELECTRIC FIELD

SUMMARY

There is a soil-like layer above the bedrock of the Moon that is produced by the small meteoroid impacts on the lunar surface, which is also called as the lunar regolith. The size of the regolith particles ranges from several centimeters to submicron size, and the small-scale particles are also referred as the lunar dust, which can be transported by the electrostatic forces above the lunar surface.

Electrostatically lofted and/or levitated dust grains were detected while scattering the sunlight above the lunar terminator region, and this physical phenomenon has been called the lunar horizon glow (LHG). TV cameras of Surveyor missions first monitored the LHG in 1966 and 1968, and the excessive brightness to coronal and zodiacal light (CZL) indicated that the dust population was considerably denser than the levels that can be produced by micrometeorite ejecta on the lunar surface. In addition, all observations of the LHG were under the solar wind plasma, and the lunar surface directly interacts with the charged particles in the absence of a global magnetic field and a dense atmosphere. Even though the solar wind plasma has a lower temperature and higher density than the magnetospheric plasma, enhanced fluxes of charged particles can be observed in some cases such as solar energetic particle events or coronal mass ejections (CMEs).

In this research, the purpose can be described as (1) predicting the maximum height variation of the dust grains above the lunar terminator under various ambient plasma conditions and (2) experimentally investigating the silica dust lofting in the vacuum chamber under the electron beam. Therefore, the equations that are used in the simulations are compared to the experimental results, and the significance of the surface parameters such as the presence of the horizontal electric field and the increased packing density on the electrostatical dust launching are investigated as well.

The LHG observations, the lunar dust exosphere measurements, and the previous studies on the lunar dust simulations and experiments are presented in chapter 1. In addition, the simulation method of the lunar surface charging and the results of the surface potential, the electric field and Debye length are discussed for the plasma parameters of the regular solar wind and three selected geoeffective CME events in chapter 2.

In chapter 3, the initial separation of the dust particles and the maximum height calculations are presented in detail. The simulation results show that the surface potential is highly variable on the lunar terminator region, and the dust launching rates are significantly controlled by the secondary electron emission and the dust sizes. Even though the micron-sized dust grains are launched from the surface more frequently than the submicron-sized dust particles, their heights are less influenced by the surface electric field in all cases. The simulations are performed for the dust particles with 0.1, 1 and 5 μm radius, and the uncertainty range of the height predictions are represented as well.

In chapter 4, the experiments on the silica dust grains are explained in detail. The experiments are performed under 4×10^{-3} Pa pressure in a general-purpose vacuum chamber. In addition, an electron beam is produced from a cathode ray tube, and the electron current density is measured as approximately 2.87×10^{-4} Am^{-2}. Different from the previous dust lofting experiments, the initial launching velocities of the grains are detected by the microscopic telescope and the high-speed camera by focusing on the near-surface area above the dust sample. Three different types of experiments are performed on the silica dust grains. First, the dust grains are loaded on the graphite plate without applying additional pressure or external horizontal electric field during the experiment. Therefore, it is called the simple case, and the measurements are compared with the estimated values. Second, the separate dust samples are compressed after loading on to the graphite plate with approximately 781 and 3780 Pa in order to increase the contact surface areas among the dust grains while decreasing the number of the microcavities. Third, the graphite plate is placed between two parallel aluminum plates that are separated by 5 and 12 cm distance and biased to 240 V in both cases. Therefore, it is expected to increase the number of the rolling particles over the surface while increasing the number of the inter-particle collisions.

Finally, all of the results are discussed for the simulations and the experiments in chapter 5. First, the dust grains with 5 μm radius reach significantly similar heights with the LHG observations of Surveyor mission in the simulations. Second, the dust grains 0.1 μm in radius are lofted to the heights similar to the Lunokhod-2 astrophotometer observations under the regular solar wind. Third, the laboratory experiments point out that several factors are determinative to estimate the dust lofting such as the contact surface areas between the dust grains, the packing density, the existence of the microcavities, and the inter-particle collisions in the presence of the horizontal electric field. Most of the particles are launched within the estimated range for the simple case. Furthermore, increased packing density reduces the number of the lofted dust grains; however, their vertical launching velocities are increased due to stronger electrostatic potential energy built-up between the dust grains. In addition, strong horizontal electric field contributes to the dust release from the surface by potentially increasing the inter-particle collisions; and the current results suggest lower launching velocities than the previous cases. Finally, the aggregates are lofted as well as the single particles, and some of them separated during the lofting motion. Therefore, the separation of charged dust grains on the flight can be an additional source for the smaller grains.

In chapter 6, the conclusions and the recommendations are explained, and the future tasks are determined as the investigation of the correlation between the micrometeorite impact regions and the electrostatic transportation of the dust grains.

1. INTRODUCTION

1.1 Lunar Environment

The lunar surface experiences extreme temperature variations, micrometeoroid bombardment, and solar and cosmic irradiation while the Moon orbits the Earth at a distance of 384,000 km, which corresponds to approximately 60 Earth radii. The Moon has no global magnetic field; instead, mini-magnetospheres are present on the lunar surface. In addition, it has a radius of 1738 km and a mean density of 3.34 g/cm^3 (French et al., 1991), and most of the lunar surface is covered with the lunar regolith that is composed of the rock fragments and the fine-grains with varying sizes.

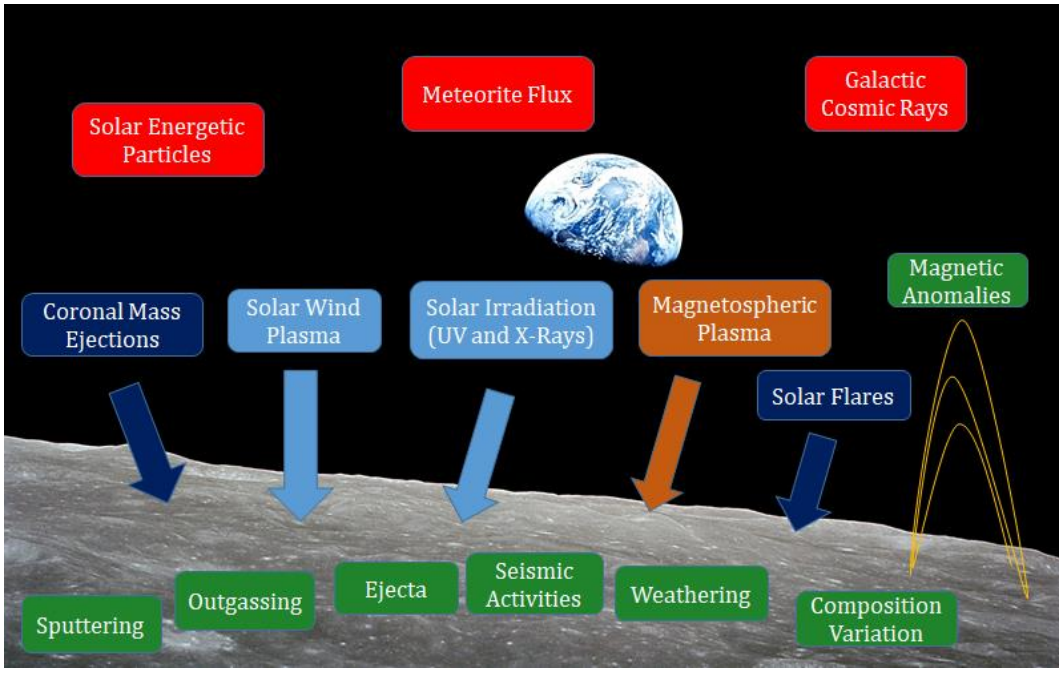

Figure 1.1 : Lunar surface interactions with the space environment.

The lunar surface is a particular environment to study the dusty-plasma physics since the Moon interacts directly with the space weathering effects in the absence of a global magnetic field and a dense atmosphere (Fig. 1.1). For instance, the exposure to the micrometeorite bombardments, the intense solar radiation and the flux of the incoming charged particles from the Sun or the geomagnetic tail are consistently present in the vicinity of the Moon. While it orbits the Earth, the lunar surface is

under the influence of the incoming charged particles from the Sun most of its time, and it interacts with the Earth's magnetospheric plasma while passing through the geomagnetic tail (Fig. 1.2). Therefore, the surrounding ambient plasma environment is highly variable, and the lunar dayside emits photoelectrons due to the solar irradiation. Even though non-monotonic potentials on the lunar dayside, where the electron sheath is formed dominantly by the photoelectron emission, have been predicted for some cases (Poppe and Horányi, 2010; Halekas et al., 2011; Poppe et al., 2012), non-monotonic surface potentials are not observed above the lunar terminator region.

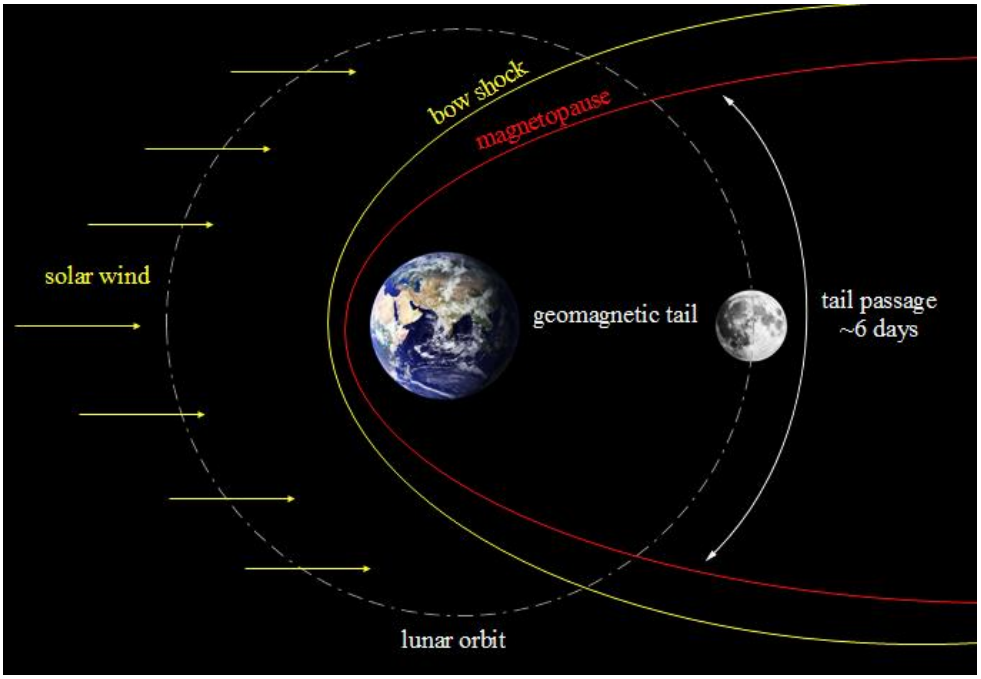

Figure 1.2 : Lunar orbit around the Earth.

Since the Moon can be considered as an insulated sphere for the interaction with the upstream plasma, the interplanetary magnetic field (IMF) is almost undisturbed while passing through the Moon (Lianghai et al., 2013; Xie et al., 2015). A lunar wake is present behind the Moon since the solar wind (SW) plasma is absorbed by the lunar dayside region (Fig. 1.3). As a result, the surface potential values differ with the location on the Moon such as subsolar point, nightside or the lunar terminator as well as the interaction with the incoming charged particles. During the Apollo missions, the lunar surface potential was determined as approximately +10 V on the dayside and -100 V near the terminator and the lunar night side under the SW (Freeman and Ibrahim, 1975; Whipple, 1981). The lunar surface potential ranging from +10 V to -4 kV by various ambient plasma parameters were reported previously (Walbridge,

1969), and the theoretical model predictions are roughly in agreement with the previous observations (Freeman and Ibrahim, 1975; Manka, 1973; Harada et al., 2013; Stubbs et al., 2014).

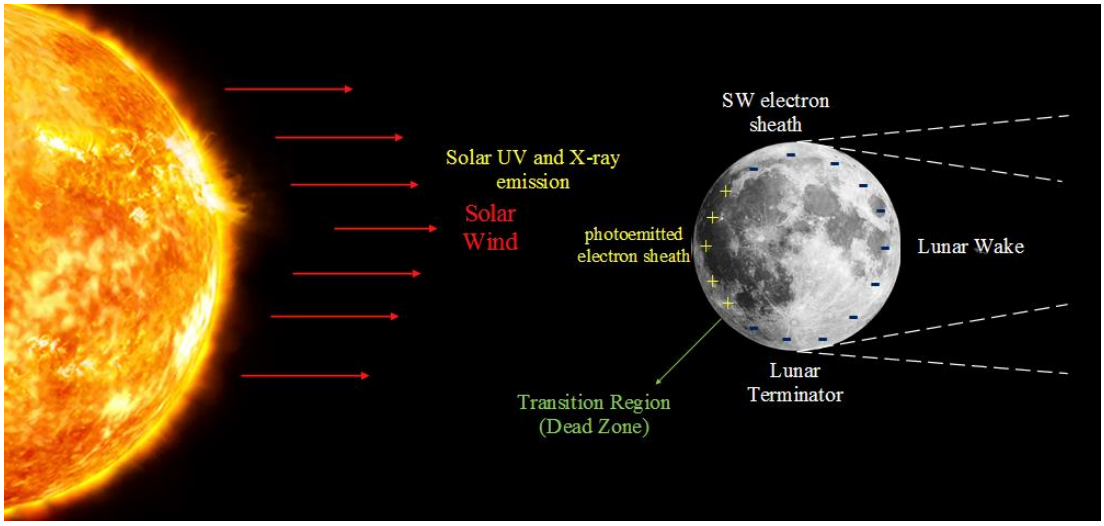

Figure 1.3 : Lunar surface interaction with the solar wind.

1.2 Lunar Dust Particles

The lunar regolith material is produced due to the micrometeorite impacts and the space weathering processes with a wide range of particle sizes and properties (Fig. 1.4).

Figure 1.4 : Lunar regolith material (Image Credit: NASA, Apollo 16 photograph).

The soil-like layer above the bedrock of the Moon contains a high number of particles with sizes from several centimeters to a submicron range as well as the larger rocks and boulders (Stubbs et al., 2014; Popel et al., 2016). The smallest component of the lunar regolith can be easily transported above the surface with

several physical mechanisms. For instance, a high-velocity impact with 100 m/s or higher can form a significant amount of ejecta, and these particles can be thrown away from the impact region at velocities on the same order of the projectile.

Figure 1.5 : Apollo 17 mission commander Gene Cernan (1934-2017) and his spacesuit covered with lunar dust inside the lunar module (Image Credit: NASA, Published: October 5, 2017).

Even though the lunar dust was anticipated before Apollo missions (Jaffe, 1965), its influence on the astronauts and the spacecraft were not easily foreseen. For instance, the dust grains easily entered to the spacesuits of the astronauts and the strongly sealed interiors of the landers (Fig. 1.5). First, one of the astronauts had health problems due to inhaling the dust even though their time on the surface of the Moon was significantly brief. On the other hand, the seal mechanisms were not able to insulate the dust from the outer regions; therefore, the area inside the lander became contaminated by the dust grains, and they cannot be easily removed due to the strong adhesive forces.

The entire surface of the Moon accommodates a thick layer of the lunar soil, which is composed of fragmented and shattered rocks as well as the dust grains. The regolith layer has a thickness as approximately 4-5 m in mare regions and 10-15 m in highland territories (McKay et al., 1991). Even though the lunar dust is not clearly defined within the lunar soil components, it is generally assumed as the particles with the sizes smaller than approximately 10 μm (Fig. 1.6). There are four noticeable shapes of the lunar dust grains such as (1) spherical, (2) angular blocks, (3) glass

fragments, and (4) irregular that are determined via scanning electron microscopy images (Park et al., 2006).

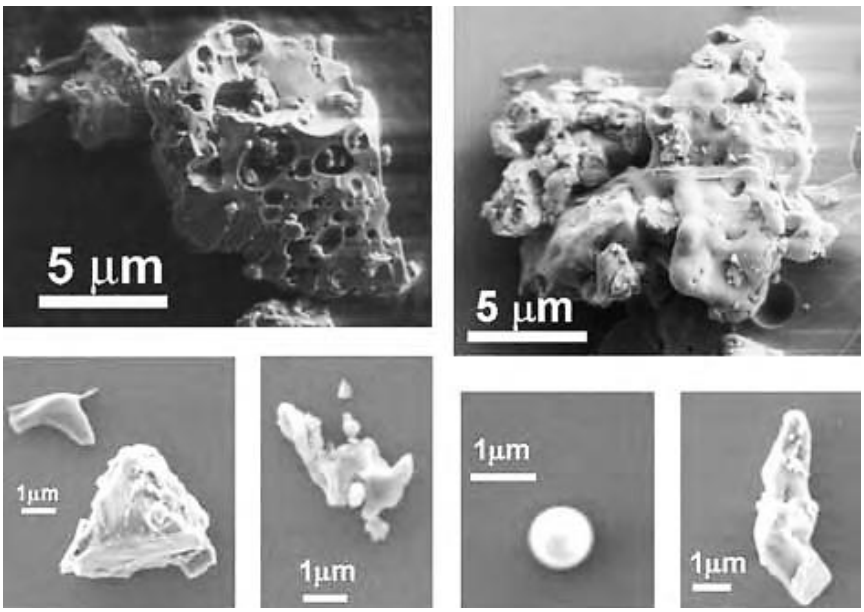

Figure 1.6 : Scanning electron microscopy images of Apollo 17 lunar dust 70051 (Park et al., 2006).

Figure 1.7 : Japanese lunar simulant separated by sifting process in the laboratory.

The formation of the lunar soil is different from the terrestrial soil that is produced by the biological and chemical interactions and contains organic matter. In addition, the humidity is extremely low on the lunar surface, and the lunar dust grains are remarkably adhesive. Even though the similar processes can be tested in the laboratory experiments, the impact-generated lunar regolith grains are particularly sharper than the particles within the lunar simulants produced on the Earth (Fig 1.7) since they have the fragmented edges without any wearing down process due to the wind or water (Fig. 1.8) (Noble, 2009).

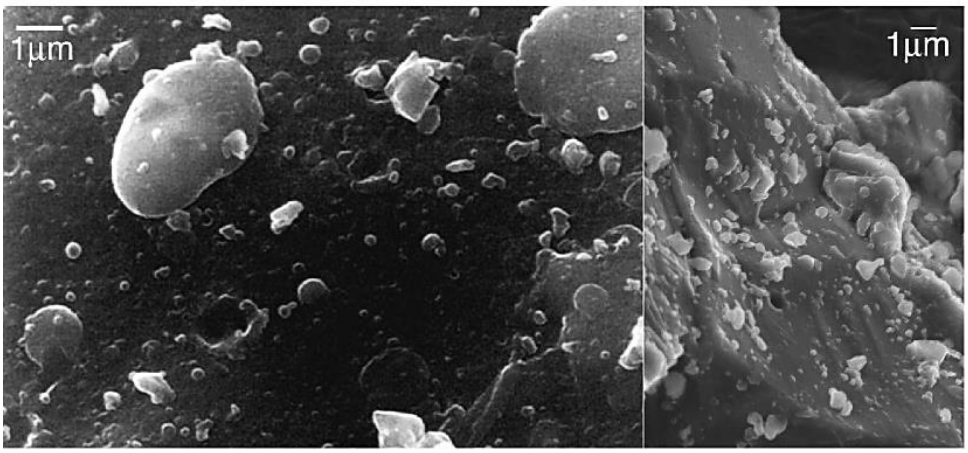

Figure 1.8 : Electron microscope images of a surface of a rock and a soil particle with submicron-sized grains attached on the surfaces (Wentworth et al, 1999).

Dust particles can be transported by the electrostatic forces, the meteoroid impacts and the external forces caused by humans, robotic missions or any other physical process such as seismic activity (Colwell et al., 2007). Considering the physical mechanisms, many processes act simultaneously as a dust transportation source such as:

1. Dust transport solely by the electrostatic forces.
    a. Dust grains accumulating sufficient charges to be detached from the surface by overcoming the contact forces and gravity.
    b. Single particle lofting from the surface, levitation by the surface electric field due to the electrostatic forces, and rolling motion on the surface.
    c. Transporting smaller-sized grains that are attached on the mobilized larger particles.
    d. Mobilizing as a group of dust grains (aggregates).
2. Dust grains that are ejected by the micrometeorite impacts
    a. Being launched with high velocities from the close region to an impact epicenter.
3. Dust transportation from the outer part of the elastic deformation regions of the micrometeorite impacts
    a. Being mobilized from the surface in a sufficient distance to cancel contact forces initially.

b. Potentially advancing by the electrostatic forces after the initial separation by the micrometeorite impacts.

1.3 Literature Review

1.3.1 Lunar Dust Measurements

1.3.1.1 Surface Observations

There are several missions that detected the lunar dust transportation in the vicinity of the surface such as Surveyor, Apollo, and Lunokhod-2. Even though Apollo used an instrument to detect the particles directly, Surveyor and Lunokhod-2 inspected the light scattering related to the dust abundance above the surface.

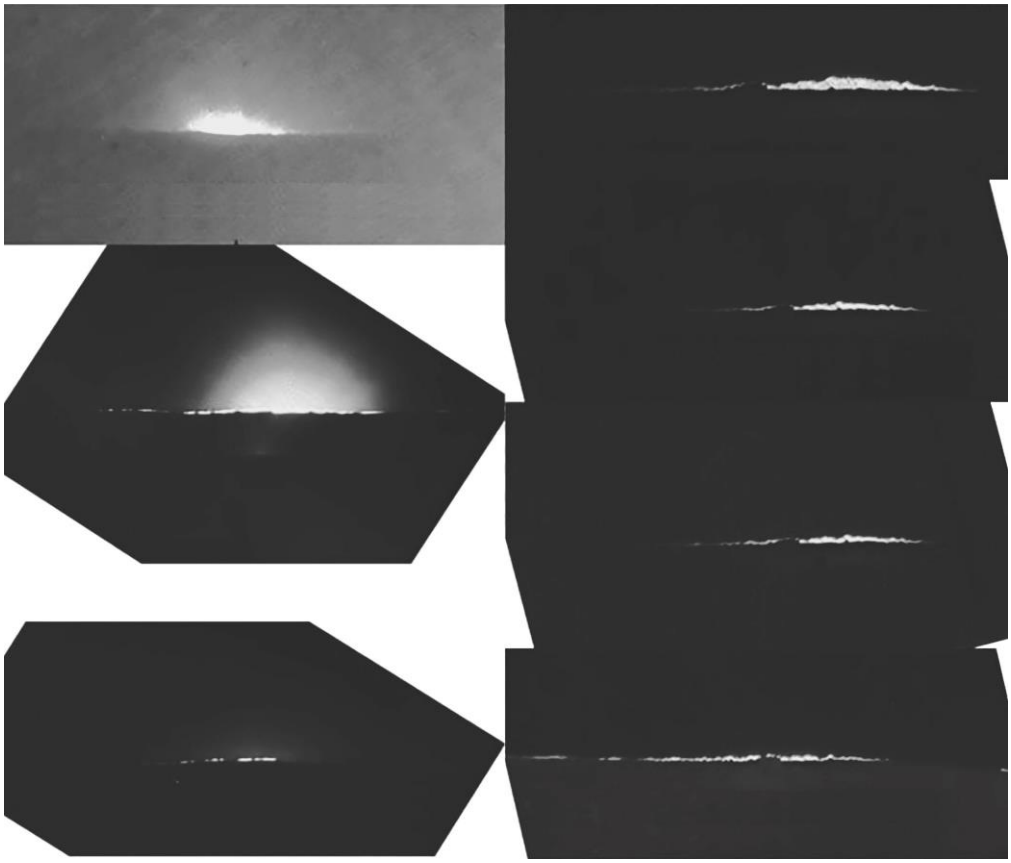

Figure 1.9 : Lunar horizon glow detected by the TV cameras of the Surveyor 5, 6, and 7 landers (Colwell et al., 2007).

Surveyor onboard TV cameras performed the most consistent observations of the forward-scattering of the sunlight by the lunar dust particles. All observations of the LHG were related to the lunar terminator on the western horizon, and lofted and/or levitated dust grains by the electrostatic forces were proposed to be the reason of

forward-scattering of the sunlight. It was first spotted by the TV cameras of Surveyor missions in 1966 and 1968 prior to the Apollo missions, and the excessive brightness to the CZL indicated that the dust population was considerably higher than the levels that can be produced by the micrometeorite ejecta from the lunar surface. Moreover, the image analysis indicated that the dust particles 5-6 μm in radius reach up to approximately 30 cm height while following the passage of the lunar terminator (Criswell, 1973; Rennilson and Criswell, 1974). Surveyor 7 was able to start monitoring the western horizon earlier than the other Surveyor missions. As a result, it detected the highest brightness level since the lunar terminator was in a close distance to the spacecraft and moving away continuously; hence the brightness was decreasing gradually. For this reason, all other detections can be compared to Surveyor 7 (Fig. 1.9).

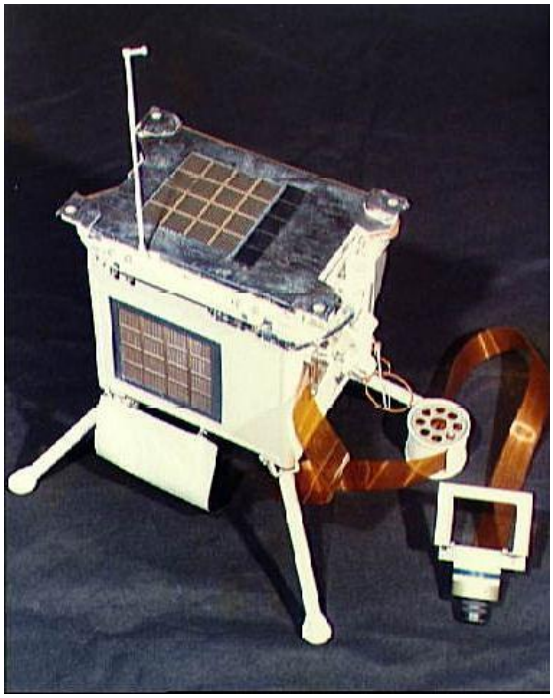

Figure 1.10 : Apollo 17 Lunar Ejecta and Meteorites (LEAM) Experiment (Image Credit: NASA).

Following the Surveyor missions, Apollo 17 Lunar Ejecta and Meteorites (LEAM) Experiment was able to measure the mobilized dust particles on the lunar surface (Fig. 1.10). It was designed to measure the velocity, direction, and total kinetic energy of the particles, which were supposed to be the result of the micrometeorite impacts on the lunar surface. It was set up by the astronauts at the Apollo 17 landing site as a part of the Apollo Lunar Surface Experiment Package (ALSEP). The objectives were to determine the variation of the cosmic dust influxes in cislunar

space, the nature of the impact ejecta, the relative contribution of comets and asteroids, the correlation between the ejecta events and times of the meteorite streams, the extent of the contribution of interstellar particles toward the maintenance of the zodiacal cloud and to investigate the existence of an effect called “Earth focusing of dust particles” (Berg, Wolf and Rhee, 1973). The LEAM instrument detected a high number of dust grains that were moving slower than the micrometeorite ejecta. For this reason, the electrostatic dust transportation was suspected to be the physical mechanism behind the detection of the slower dust particles. In addition, the observations had two peaks for the dust detections, which are before and after the terminator passage that is pointing out the surface electric field enhancements. Fig.1.11 shows a three-hour interval counting rate for 22 lunations that demonstrate strong dust transportation enhancements near the sunrise region (Berg et al., 1976).

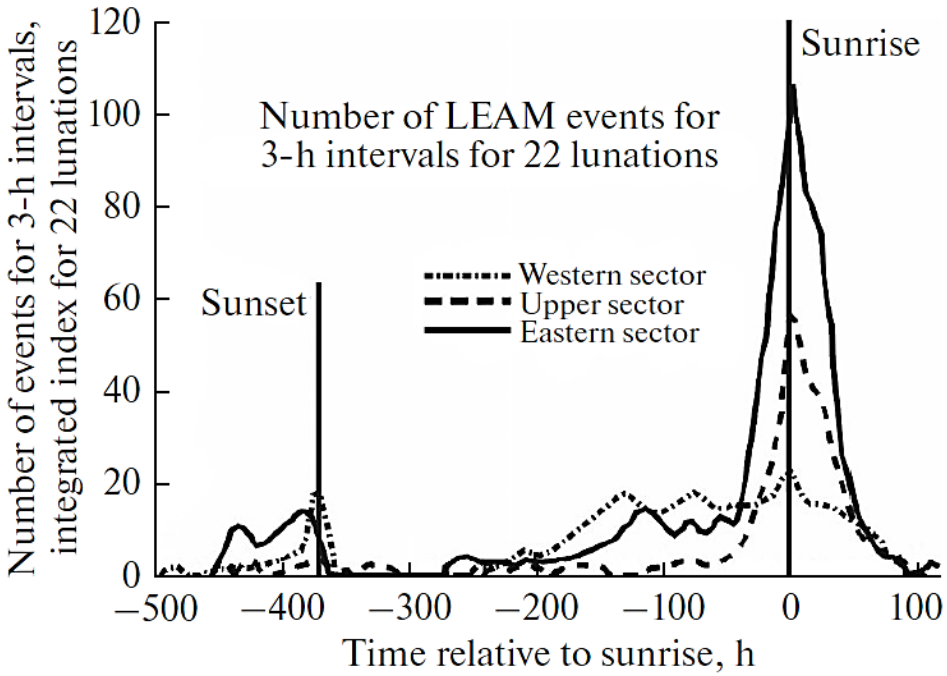

Figure 1.11 : Apollo 17 LEAM dust transportation detections (Berg et al., 1976).

Following the previous measurements, Lunokhod-2 carried an onboard instrument to detect the light scattering above the lunar surface (Fig. 1.12). Onboard astrophotometer performed the measurements in the shadow region when the solar limb was 17 mrad below the lunar horizon (Severny et al., 1975). The estimated dust cloud due to the light scattering was at an altitude approximately 260 m above the lunar surface (Severny et al., 1975; Popel et al., 2018).

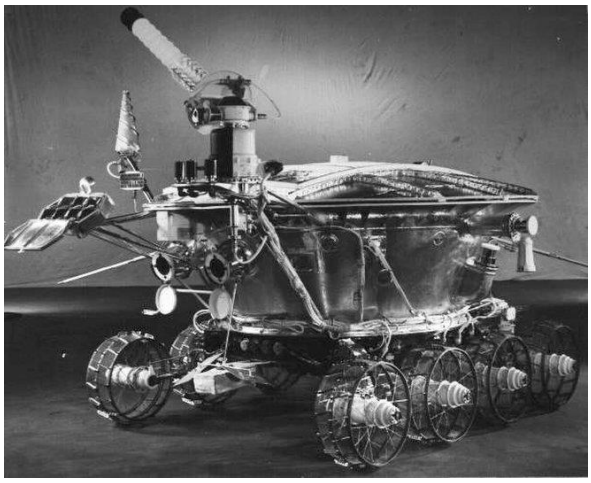

Figure 1.12 : Roving remote-controlled robot Lunokhod (Image Credit: NASA).

1.3.1.2 Orbital Observations

The presence of the exospheric dust cloud was also detected at high altitudes above the lunar surface following the surface observations. Direct measurements are performed as well as indirect detections due to the sunlight scattering and the radio wave reflections due to the charged dust grains in the lunar exosphere. These measurements of the exospheric dust cloud showed that the dust population at high altitudes is exceptionally variable.

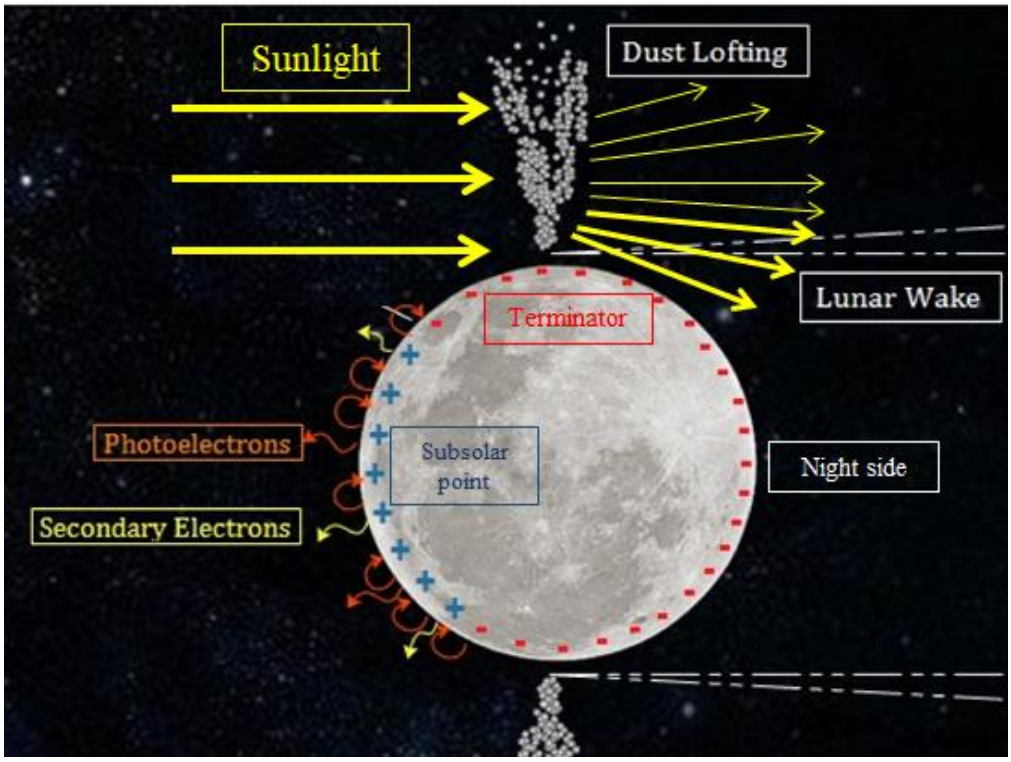

Figure 1.13 : Light scattering by the dust grains above the lunar terminator region.

Apollo 15 orbital image sequences indicated the excessive brightness over the lunar terminator while orbiting around 100 km altitude. In addition, the Apollo 17 astronauts sketch some of the observations as well. For instance, the blue line shows the boundary of the LHG in Fig 1.14, whereas the red line shows the boundary of the light-scattering by the interplanetary dust particles that is called CZL. Since the light-scattering observations corresponded to several kilometers above the lunar terminator region (Fig. 1.13), it is called as "high-altitude LHG". However, it appears that the high-altitude LHG is a variable phenomenon since it was present during the image sequences of Apollo 15 on orbit, whereas there was no trace of excessive brightness to the CZL during Apollo 16 mission (McCoy, 1976; Glenar et al., 2011; Stubbs et al., 2006). The dust population during Surveyor observations is estimated as micron-sized, whereas it is suspected to be submicron-sized (0.1 – 1 μm in radius) during Apollo missions.

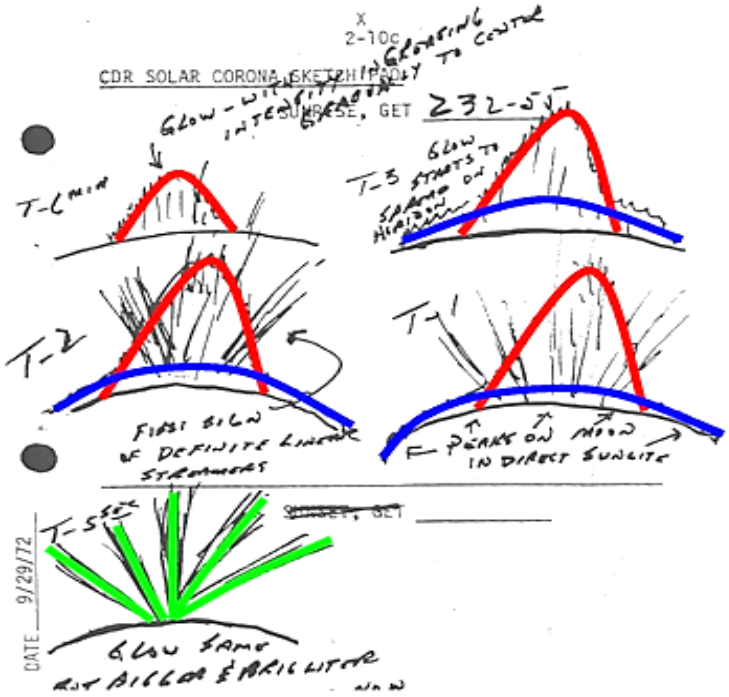

Figure 1.14 : A sketch by Apollo 17 astronaut Eugene Cernan (Stubbs et al., 2006).

The Soviet Luna-19 and Luna-22 spacecraft performed a series of measurements to detect the electron concentration around the Moon (Vasil'ev et al., 1974; Vyshlov, 1976). These radio measurements pointed out that an ionosphere is present above the sunlit part of the lunar surface, where the highest values of electron density shows indirect evidence for the presence of the charged dust grains in the lunar exosphere (Stubbs et al.,2011).

Figure 1.15 : Lunar Orbiter Luna-19 (Image Source: Wikipedia).

Previously, Clementine star tracker navigation cameras searched for the forward-scattering of the sunlight in order to observe the high-altitude LHG similar to the Apollo 15 (Fig. 1.16). However, the high-altitude LHG was not detected during these measurements, and it suggested that the dust abundances are not influenced by the electrostatic transportation at the altitudes that are detectable during an orbital mission (Glenar et al., 2014). In addition, it pointed out that the dust density related to the Apollo 15 LHG observations can be infrequent in nature even though the measured dust heights suggested the dust exosphere extending several kilometers above the surface.

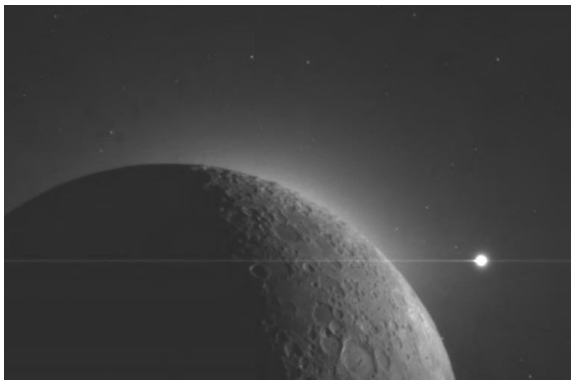

Figure 1.16 : Star tracker image by Clementine spacecraft (Image Credit: NASA).

LRO (Lunar Reconnaissance Orbiter) the Lyman-Alpha Mapping Project (LAMP) UV spectrograph measurements could not measure any distinguishable dust densities suggesting any excessive brightness above the lunar horizon (Feldman et al., 2014). During the measurements, the SW plasma parameters were unremarkable; however, the annual meteor showers were present. These results concluded that any detection

of the LHG with the present dust heights would be a challenge due to the CZL from the interplanetary dust clouds since the brightness of the CZL conceals the LHG that is with lower brightness levels (Fig. 1.17).

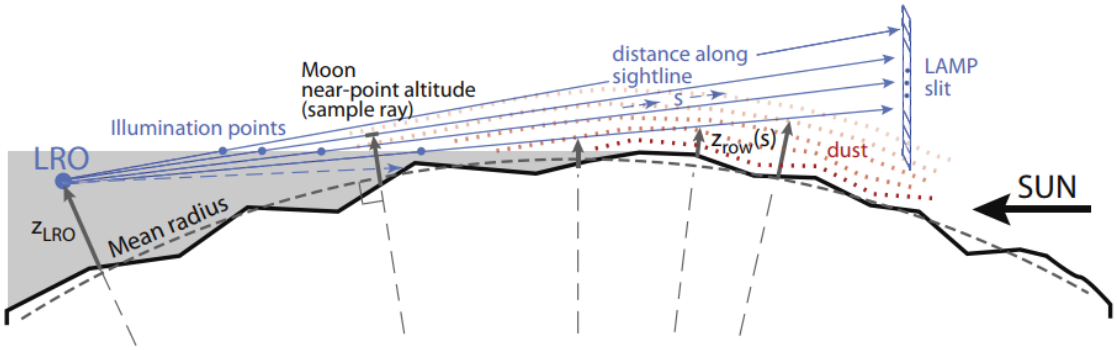

Figure 1.17 : The LAMP's line-of-sight showing the center of each pixel above the lunar surface (Feldman et al., 2014).

The Lunar Atmosphere and Dust Environment Explorer (LADEE) mission measured the dust particles between 3-250 km altitudes around the Moon. The results concluded that the dust densities of 0.1 micron sized grains suggested by the LHG observations during the Apollo 15 orbit sequences were not present similar to the LRO and Clementine measurements (Horányi et al., 2015; Szalay and Horányi, 2015). In addition, it observed a dust density enhancement due to the micrometeorite influx to the lunar surface (Fig. 1.18).

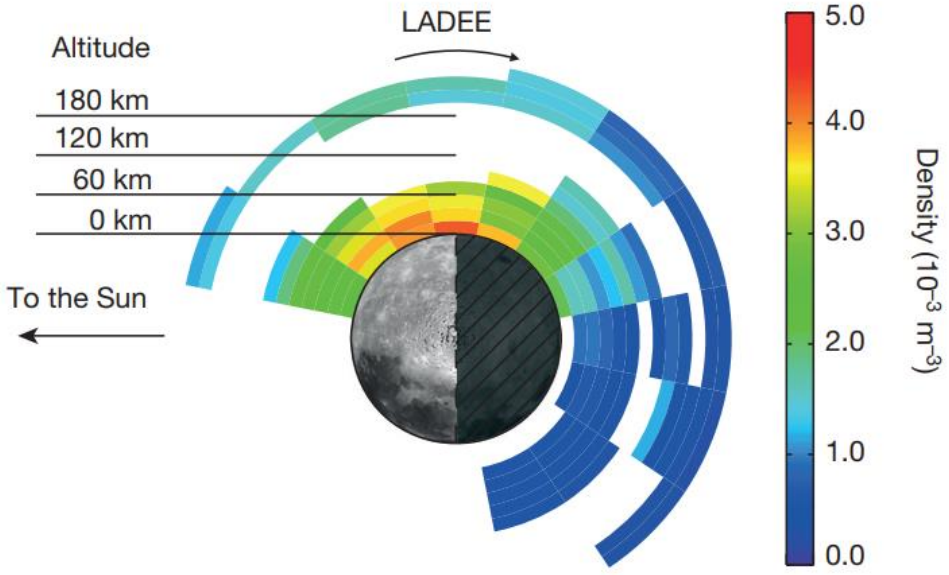

Figure 1.18 : Lunar dust distribution measured by LADEE mission (Horányi et al., 2015).

According to these measurements, it can be said that the lunar dust exosphere can reach several kilometers above the lunar surface; however, it is considerably infrequent at high altitudes compared to the observations near the surface. Therefore, it can be summarized as:

1. The dust grains with 5-6 μm radius are consistently lofting up to approximately 30 cm height above the lunar terminator region.
2. The high-altitude LHG is a highly variable phenomenon, and it was observed above the lunar terminator region similarly to the Surveyor observations. Even though the light scattering near the lunar surface was monitored throughout the Surveyor missions, any other orbital mission has not repeated Apollo 15 brightness observations yet.
3. The altitudes suggested by the LADEE mission for the lunar dust exosphere indicated that electrostatic dust lofting could be an additional source to the dust abundances at lower altitudes than the observations during the Apollo missions.
4. The LEAM measurements showed that the number of dust detections increased significantly near the lunar terminator region, where strong horizontal electric fields could be present and contribute to the dust release.
5. It can be a challenging task to observe the LHG from orbit since the particularly bright CZL can overlap with the low brightness of the high-altitude LHG.

1.3.2 Simulation Studies

Singer and Walker (1962) calculated the velocity distribution of the dust particles that are ejected by the impacts while considering the electrostatic dust erosion under the solar irradiation, and they estimated the surface density of the lofted particles on the sunlit surfaces of the Moon. In addition, Rennilson and Criswell (1973) analyzed the horizon glow images of Surveyor 5, 6 and 7, and they concluded that the light scattering dust cloud must have formed by the grains with approximately 10 μm diameter. Their analysis showed that the charged dust particles could be levitated by the intensified local electric fields between the sunlit/shadow boundaries near the lunar terminator region. Furthermore, the dust cloud requires 10^7 times more dust particles that are launched from the lunar surface than the micrometeorite ejecta (Rennilson and Criswell, 1973).

Manka (1973) used the current balance method to calculate the surface potential values of the subsolar point and the lunar terminator throughout the orbit of the Moon. In addition, Freeman and Ibrahim (1975) investigated the surface potential and the electric field of the lunar dayside and the terminator region under the SW plasma, and they concluded that the electric fields, which are limited to several meters above the lunar surface, could be stronger than the SW electric field at least 3 orders of magnitude.

Goertz (1989) showed that the charge magnitudes of the small-sized dust grains respond to the fluctuating plasma parameters slower than the large particles. Therefore, submicron-sized dust grains require longer periods than the micron-sized particles in order to reach the equilibrium potential. Moreover, Nitter et al. (1998) studied the levitation and dynamics of the charged dust particles within a photoelectron sheath, and they indicated that a high number of parameters control the electrostatic levitation such as initial charge and velocity, grain shape, mass density, charging properties of the dust, other main forces, and the ambient plasma parameters.

Since the Apollo observations indicated the presence of the dust cloud at the altitudes that are orders of magnitude greater than the electron sheath thickness on the lunar terminator, a dynamic fountain model for the lunar dust was proposed to estimate the maximum potential heights of the lofted dust grains (Stubbs et al., 2006). It calculated the electrostatic acceleration of the dust particles within the surface electric field by assuming one-dimensional Debye shielding and deceleration with the lunar gravity after exiting the electron sheath.

Sternovsky et al. (2008) showed that the solar activity could significantly modify the surface conditions that control the electrostatic dust transportation by comparing the solar minimum, solar maximum, and a solar flare. Furthermore, Halekas et al. (2009) compared the models and Lunar Prospector measurements for solar energetic particle events, and they concluded that the secondary electron emission yield is approximately 3 times smaller than the previous laboratory experiments with the lunar soil samples, which potentially indicates the re-absorption of the emitted electrons by the surface features or roughness.

Poppe and Horanyi (2010) used a one-dimensional particle-in-cell (PIC) for the lunar surface in order to study the levitation and charging of the dust particles within the photoelectron sheath. In addition, Glenar et al. (2011) reanalyzed the Apollo 15 light scattering observations by a Mie-scattering simulation code, and they concluded that the relationship between the solar activity and the exospheric dust was not determined by using the Kp index, $F_{10,7}$ flux, and the high energy proton flux.

Vaverka et al. (2012) calculated the equilibrium dust potentials, and they pointed out the importance of the secondary electron emission by the energetic electrons during the plasma sheet crossings within the geomagnetic tail. In addition, Farrell et al. (2013) investigated the response of the lunar surface and the trapping of the photoelectrons by the surface potential during a solar storm event, and Stubbs et al. (2014) showed that the lunar surface potential could be estimated as a two-current problem for the fast and slow stream SW conditions. Vaverka et al. (2016) used the real plasma parameters from ARTEMIS in order to estimate the lunar surface and the dust grain potentials during the geomagnetic tail passages, and they determined that the secondary electron emission increases the positive potentials particularly in the magnetosphere.

1.3.3 Experimental Investigations

The electrostatical dust lofting was demonstrated for the alumina grains in the vacuum chamber experiments that were observed via the laser light scattering by a photomultiplier tube (Sheridan et al., 1992). Furthermore, levitation of the dust grains was investigated in a low-density plasma, and three types of dust grains were used in these experiments such as polystyrene divinylbenzene microspheres, glass microballoons, and JSC-1 lunar regolith simulant (Sickafoose et al., 2002). In these experiments, the dust particles levitated individually or jointly while supporting the model of the electrostatic transportation for the levitation. Wang et al. (2009) conducted experiments on the JSC-Mars-1 simulant on a conductive surface. The dust grains were isolated particles with a particle size smaller than 25 μm, and the dust lofting was demonstrated via the particles transported from the conductive surface to an isolated block near the dust sample. Hartzell et al. (2011, 2013) indicated the determinative characteristics of the adhesive forces for the dust grains in the laboratory experiments; consequently, they concluded that the required surface

electric field strength to detach a dust grain is minimum for intermediate-sized particles.

Wang et al. (2016) proposed a new “patched charge model” by conducting experiments on the insulating dust particles while demonstrating the importance of the emission and re-absorption of the emitted electrons. Furthermore, Champlain et al. (2016) investigated the limits of the cohesive force between the dust grains while indicating that the electrostatic dust lofting process could be an additional source to the interplanetary dust impacts for the lunar dust exosphere at low altitudes. Finally, Schawn et al. (2017) measured the charge magnitudes of the dust particles from the regolith simulant and the silica microspheres. As a result, the corresponding enhanced charging numbers for the patched charge model were reported.

1.4 Purpose of Thesis

As stated previously, the observation of the LHG is a challenging task due to its infrequent occurance at high altitudes. Since La SEINE (Laboratory of Spacecraft Environment Interaction Engineering) plans to have a future lunar CubeSat mission aiming to monitor the light scattering above the lunar horizon, it is critical to estimate the expansion of the lunar dust exosphere related to the space environment conditions near the Moon. In addition, the electrostatic transportation of the dust particles over the airless planetary bodies such as the Moon and the astreoids are not entirely understood yet.

This dissertation presents the research on the electrostatic dust transportation over the lunar terminator region as:

1. Simulations of the lunar surface charging and the electrostatic dust lofting above the lunar terminator
    a. Estimating the lunar surface potential, the electric field, the electron sheath thickness and the location of the dead zone.
    b. Developing a code that uses the actual SW data and predicts the dust heights above the lunar terminator region.

c. Including the charging mechanisms on the surfaces exposed to the incoming SW and the patch surfaces within the gaps (microcavities) between the dust grains exposed to the emitted secondary electrons.

d. Including the effects of the lunar gravity and the contact forces on the dust lofting depending on the particle size and the surface cleanliness parameter.

e. Calculating the initial charging of the dust grains over the lunar terminator region by considering the time dependence and the ambient plasma conditions.

f. Estimating the initial vertical launching velocities of the dust grains related to the LHG observations.

g. Calculating the charge variation of the dust grains related to the ambient plasma conditions and the solar irradiation during the lofting motion.

h. Reporting the maximum height predictions reachable by the dust grains above the lunar terminator.

2. Experimental investigation of silica dust lofting inside the vacuum chamber under the electron beam current

a. Demonstrating dust lofting due to the charging on the patch surfaces within the microcavities between the dust grains.

b. Investigating the capability to estimate the dust lofting results by the proposed equations for the simulations.

c. Observing the dust transportation mechanisms by the microscopic telescope and high-speed camera.

d. Developing a particle trajectory tracing code for the video output of the high-speed camera.

e. Investigating three different experimental conditions such as (1) the simple case without the compression of the dust sample or horizontal electric field, (2) the increased packing density case after the dust sample is pressurized, and (3) the experiment with additional horizontal electric field.

2. LUNAR SURFACE CHARGING SIMULATIONS

2.1 Introduction

The Moon directly interacts with dynamic plasma conditions in the absence of a global magnetic field and a dense atmosphere. It spends most of its time under the SW influence, and it travels through the magnetotail, magnetosheath and bow shock while it orbits the Earth. Even though the SW plasma has lower temperature and higher density than the magnetospheric plasma, enhanced fluxes of charged particles can be observed in some cases such as solar energetic particle events (SEPs) (Halekas et al., 2009) and CMEs (Farrell et al., 2013). In addition, the fluxes of energetic particles can be present during geomagnetic storms and substorms (Colwell et al., 2007; Asano et al., 2010; Vaverka et al., 2016). In all of these cases, the lunar surface potential is controlled by the surrounding plasma conditions and the photoemission of electrons from the dayside of the Moon due to solar UV and X-ray radiation. The main current sources can be expressed as the collection of ambient plasma electrons and ions, the photoemission of electrons and the secondary electron emission from the lunar surface.

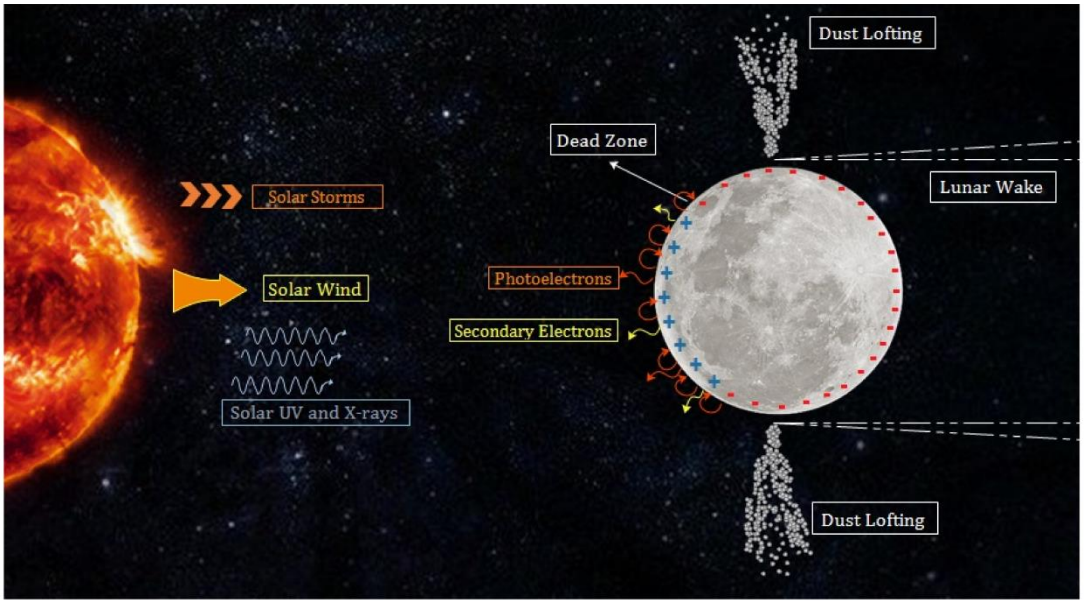

Figure 2.1 : Lunar surface charging and dust lofting above the terminator.

The measurements and the simulation results point out that the lunar surface potential is highly variable, and the range of the potential values differs according to the location on the Moon such as subsolar point, night side or the terminator region as well as the ambient plasma conditions. During the Apollo missions, the lunar surface potential was determined as approximately +10 V on the dayside and -100V near the terminator and night side regions under the SW (Freeman and Ibrahim, 1975; Whipple, 1981). Manka (1973) reported approximately +10 V on the dayside and -38 V on the lunar terminator under the average SW conditions by the current balance calculation. Furthermore, +2.85 V on the subsolar point and -47.4 V on the terminator region have been determined for the slow stream SW conditions, whereas +4.22 V on the subsolar point and -44.9 V on the terminator region were calculated for the fast stream SW (Stubbs et al., 2014).

The current balance approach is used to calculate the surface potential from the subsolar point to the lunar terminator, which is the boundary between the sunlit surface of the Moon and the lunar nightside, by the flowing plasma equations in the simulations (Manka, 1973; Stubbs et al., 2014). Since the plasma parameters are highly variable during the passage of CMEs compared to the regular SW, the influence of different parameters on the surface potential, the electric field and the electron sheath above the lunar surface can be investigated. These parameters are the temperatures of the upstream ions and electrons, the plasma density and the SW bulk velocity as well as the photoemission current. Several assumptions are applied for simplification such as:

- The shape of the Moon is a perfect sphere, and the lunar radius is 1737 km.
- The surface potential and the electric field are in the equilibrium state for each step of the simulation (5-min intervals), and the lunar surface electric field is estimated by a one-dimensional Debye shielding (Stubbs et al., 2006).
- The lunar surface material conductivity is almost zero. Therefore, the Moon can be regarded as an insulated sphere.
- Plasma sheath is collisionless above the lunar surface.
- The secondary electron temperature is 2.5 eV (Vaverka et al., 2016), and the maximum secondary electron yield δ_m is assumed as 1.2 (Halekas et al., 2008).
- The mean kinetic energy of the photoemission electrons is 2.2 eV (Farrell et al., 2013).

- Plasma population has Maxwellian velocity distribution in the vicinity of the Moon.
- All ions are assumed as protons, and the plasma carries no magnetic field.
- Potentials above the charged surfaces are monotonic.

Even though non-monotonic potentials on the dayside of the Moon have been predicted for some cases (Poppe and Horányi, 2010; Halekas et al., 2011; Poppe et al., 2012), there is no observation of non-monotonic surface potential above the lunar terminator. In addition, the interplanetary magnetic field (IMF) is almost undisturbed while passing through the Moon (Lianghai et al., 2013; Xie et al., 2015), and its effect will not be studied in this thesis.

In steady state, the net equilibrium current to the lunar surface can be given as:

$$J_{Pe} + J_i + J_e + J_{sec} = 0 \tag{2.1}$$

By using this equation, the surface potential $\emptyset_s$ can be calculated according to the surrounding plasma conditions and solar irradiation. The elements of this equation can be described as the photoemission electron current J_{Pe}, ion collection current from surrounding plasma J_i, electron collection current from surrounding plasma J_e and the secondary electron emission J_{sec}.

One assumption can be made for the dayside region that the secondary emission of electrons from the surface and the dust particles is negligible under the SW conditions while determining the surface potential. The primary electron thermal energies T_e are significantly smaller under the regular SW conditions than the maximum yield of secondary electrons, which is approximately 400 eV, whereas colder electrons generally accompany the CME events. Therefore, it reduces to the three-current problem on the lunar dayside as:

$$J_{Pe} + J_i + J_e = 0 \tag{2.2}$$

Under the regular SW it is expected to see the relationship between the SW bulk velocity V_{SW} and the thermal velocities of ions and electrons as $V_{th_e} >> |V_{SW}| >> V_{th_i}$. Stubbs et al. (2014) show that fast and slow stream SW conditions can be estimated as a two-current problem, $J_{Pe} + J_e = 0$ since the currents of photoemission and incoming electrons charge the surface dominantly (Stubbs et al., 2014). Due to

the regular SW conditions of 10.4 eV ion temperature, 12.1 eV electron temperature and 400 km/s SW bulk velocity, the ratio between the velocities can be given as $V_{th_i}/V_{th_e} = 0.022$, $V_{SW}/V_{th_i} = 8.961$ and $V_{SW}/V_{th_e} = 0.194$.

The analytical model by Stubbs et al. (2014) assumes that ion currents can be ignored on the dayside as well as the secondary electron emission for the certain upstream plasma conditions. For instance, if close values for the thermal energies of electrons and ions are present for an ambient plasma population, it means that the thermal velocities have a relation as $V_{th_i} \ll V_{th_e}$ because of the difference between the particle masses as $m_i \gg m_e$. Stubbs et al. (2014) state that their assumption is rational under the regular SW case, and it allows to reduce the three-current problem presented in Equation 2.2 as:

$$J_{Pe} + J_e = 0 \tag{2.3}$$

Another assumption is that the plasma sheath is collisionless above the surface; therefore, Liouville's Theorem is valid, which means that phase space density is conserved for the charged particles species. The following equations are solved by using the isotropic Maxwellian velocity distribution function (VDF) (Baumjohann and Treumann, 1997), and the photoelectron VDF can be expressed as:

$$f_{Pe}(x, \vec{v}) = n_{Pe0} \left(\frac{m_e}{2\pi k_B T_{Pe}}\right)^{3/2} exp\left\{-\frac{[(1/2)m_e \vec{v}^2 - e(\emptyset(x) - \emptyset_s)\,]}{k_B T_{Pe}}\right\} \tag{2.4}$$

where n_{Pe0} is photoelectron number density at the lunar surface; m_e is the electron mass; k_B is the Boltzmann constant; T_{Pe} is the photoemission electron temperature; $\vec{v}$ is the electron velocity vector; x is the distance from the surface. In addition, the VDFs for the upstream ions and electrons can be expressed for the stationary and flowing plasma population as:

$$f_s(x, \vec{v}) = n_s \left(\frac{m_s}{2\pi k_B T_s}\right)^{3/2} exp\left\{-\frac{[(1/2)m_s \vec{v}^2 + q\emptyset(x)]}{k_B T_s}\right\} \tag{2.5}$$

$$f_s(x, \vec{v}) = n_s \left(\frac{m_s}{2\pi k_B T_s}\right)^{3/2} exp\left\{-\frac{[(1/2)m_s (\vec{v} - \vec{V}_b)^2}{k_B T_s}\right\} \tag{2.6}$$

where n_s is particle species (ion or electron) number density outside of Debye shield; m_s is the electron or ion mass; T_s is the temperature of the particle species; $\vec{V}_b$ is the plasma bulk velocity vector.

2.2 Positively Charged Surfaces on the Lunar Dayside

Stubbs et al. (2014) showed that the surface potential of the attractive surfaces for the electrons can be estimated by the two-current problem as:

$$\emptyset_s = -\frac{k_B T_{Pe}}{e} \ln\left(-\frac{e n_0}{J_{Pe0} \cos\theta} \sqrt{\frac{k_B T_e}{2\pi T_e}}\right) \tag{2.7}$$

The derivation of Equation 2.7 can be shown for the attractive surfaces ($\emptyset_s > 0$) for the electrons. The photoemission current can be expressed as:

$$J_{Pe} = -e \int_{(2|e\emptyset_s|/m_e)^{1/2}}^{\infty} f_{Pe}(v_x)\, v_x\, dv_x \tag{2.8}$$

The lower limit of integral is determined as $(2|e\emptyset_s|/m_e)^{0.5}$ since the emitted photoelectrons require initial kinetic energy in order to escape the attractive potential of the lunar surface.

$$J_{Pe} = -e \int_{\left(\frac{2|e\emptyset_s|}{m_e}\right)^{0.5}}^{\infty} n_{Pe0} \left(\frac{m_e}{2\pi k_B T_{Pe}}\right)^{0.5} exp\left\{-\frac{[(1/2) m_e \vec{v}_x{}^2 - e(\emptyset(x) - \emptyset_s)\,]}{k_B T_{Pe}}\right\} v_x\, dv_x \tag{2.9}$$

$$J_{Pe} = -e\left[-\frac{k_B T_{Pe}}{m_e} n_{Pe0} \left(\frac{m_e}{2\pi k_B T_{Pe}}\right)^{0.5} exp\left\{-\frac{[(1/2) m_e \vec{v}_x{}^2 - e(\emptyset(x) - \emptyset_s)\,]}{k_B T_{Pe}}\right\}\right]_{(2|e\emptyset_s|/m_e)^{0.5}}^{\infty} \tag{2.10}$$

$$J_{Pe} = -e\left[-n_{Pe0}\left(\frac{k_B T_{Pe}}{2\pi m_e}\right)^{0.5} \left(e^{-\infty} - e^{-\frac{[|e\emptyset_s| - e(\emptyset(x) + \emptyset_s)]}{k_B T_{Pe}}}\right)\right] \tag{2.11}$$

Since $\emptyset(0)$ is equal to $\emptyset_s$ at lunar surface (x = 0), the solution can be given as:

$$J_{Pe} = -e n_{Pe0}\left(\frac{k_B T_{Pe}}{2\pi m_e}\right)^{0.5} \exp\left\{-\frac{|e\emptyset_s|}{k_B T_{Pe}}\right\} \tag{2.12}$$

The second term of equation 2.3 can be derived for the incoming upstream electrons to the surfaces with the attractive surface potential ($\emptyset_s > 0$) as:

$$J_e = -e \int_{-\infty}^{0} f_e(v_x)\, v_x\, dv_x \tag{2.13}$$

$$J_e = e \int_{-\infty}^{0} n_e \left(\frac{m_e}{2\pi k_B T_e}\right)^{0.5} exp\left\{-\frac{[(1/2)m_e \vec{v}_x{}^2 - e\emptyset(x)]}{k_B T_s}\right\} v_x\, dv_x \tag{2.14}$$

$$J_e = e\left[-\frac{k_B T_e}{m_e} n_0 \left(\frac{m_e}{2\pi k_B T_e}\right)^{0.5} exp\left\{-\frac{[(1/2)m_e \vec{v}_x{}^2 - e\emptyset(x)]}{k_B T_e}\right\}\right]_{-\infty}^{0} \tag{2.15}$$

$$J_e = e\left[\left(\frac{k_B T_e}{2\pi m_e}\right)^{0.5} n_0\, exp\left\{-\frac{[(1/2)m_e \vec{v}_x{}^2 - e\emptyset(x)]}{k_B T_e}\right\}\right]_{-\infty}^{0} \tag{2.16}$$

$$J_e = e n_0 \left(\frac{k_B T_e}{2\pi m_e}\right)^{0.5} (e^0 - e^{-\infty}) = e n_0 \left(\frac{k_B T_e}{2\pi m_e}\right)^{0.5} \tag{2.17}$$

Equation 2.7 can be retrived from the solutions in equation 2.12 and 2.17 as below:

$$-e\, n_{Pe0} \left(\frac{k_B T_{Pe}}{2\pi m_e}\right)^{0.5} \exp\left\{-\frac{|e\emptyset_s|}{k_B T_{Pe}}\right\} + e n_0 \left(\frac{k_B T_e}{2\pi m_e}\right)^{0.5} = 0 \tag{2.18}$$

$$n_{Pe0} \left(\frac{k_B T_{Pe}}{2\pi m_e}\right)^{0.5} \exp\left\{-\frac{|e\emptyset_s|}{k_B T_{Pe}}\right\} = n_0 \left(\frac{k_B T_e}{2\pi m_e}\right)^{0.5} \tag{2.19}$$

$$\ln\left(\frac{n_0}{n_{Pe0}}\sqrt{\frac{T_e}{T_{Pe}}}\right) = -\frac{|e\emptyset_s|}{k_B T_{Pe}} \tag{2.20}$$

$$\emptyset_s = -\frac{k_B T_{Pe}}{e} \ln\left(\frac{n_0}{n_{Pe0}}\sqrt{\frac{T_e}{T_{Pe}}}\right) \tag{2.21}$$

Equation 2.21 shows an expression to calculate the equilibrium surface potential of the attractive surfaces to the electrons on the dayside of the Moon for the reduced problem represented in equation 2.21 as the two-current problem. On the other hand, the function of the photoelectron emission current requires to be improved in order to include the dependence on the solar zenith angle θ for our simulations; therefore, the following equations are solved to include this term such as:

$$J_{Pe} = -e\, n_{Pe0}\left(\frac{k_B T_{Pe}}{2\pi m_e}\right)^{\frac{1}{2}} = \frac{-e\, n_{Pe0} v_{tPe}}{2\sqrt{\pi}} = \frac{J_{Pe0} cos\theta}{D^2} \tag{2.22}$$

$$n_{Pe0} = -\left(\frac{2\pi m_e}{k_B T_{Pe}}\right)^{\frac{1}{2}} \frac{J_{Pe0} cos\theta}{D^2} \tag{2.23}$$

Equation 2.21 can be improved by assuming D equals to 1 at 1 AU distance from the Sun as (Stubbs et al., 2014):

$$\emptyset_s = -\frac{k_B T_{Pe}}{e} ln\left(\frac{n_0}{n_{Pe0}}\sqrt{\frac{T_e}{T_{Pe}}}\right) = -\frac{k_B T_{Pe}}{e} ln\left(-\frac{n_0 e}{J_{Pe0} cos\theta}\sqrt{\frac{k_B T_e}{2\pi m_e}}\right) \tag{2.24}$$

Even though equation 2.24 can be used to estimate the surface potential of the positively charged areas of the lunar dayside under the nominal SW conditions, the flowing plasma equations must be applied when the flowing components of the charging current equations develop into considerable levels. For instance, the SW bulk velocity V_{SW} and the thermal velocities of the upstream electrons and ions can become comparable during the passages of CMEs since colder electrons generally accompany these events. In addition, the thermal velocities of the SW ions increase during the post-shock plasma passages while the SW bulk velocity throughout the CME can be enhanced significantly. As a result, the surface charging calculations turn into a three-current problem that includes the emission of photoelectrons from the surface, the incoming SW electrons, and the incoming SW ions (equation 2.2). Therefore, the flowing plasma equations must be applied in the simulations for the current balance method in order to introduce the contribution of the increased ion tempterature and the enhanced SW bulk velocity.

Manka (1973) reported the results of the surface potential and electric field, which are obtained for the isotropic plasma population surrounding the Moon, and the plasma sheath is considered as thin compared to the lunar radius. In addition, the calculated equilibrium conditions can point out the local surface potential independently since the electrical conductivity is significanly low for the lunar soil material. These equations can be expressed as:

$$J_e = -\frac{n_0 e v_{th_e}}{2\sqrt{\pi}}\left[e^{-U_e{}^2} + U_e\sqrt{\pi}(1 + \mathrm{erf}(U_e))\right] \tag{2.25}$$

$$J_i = \frac{n_0 e v_{th_i}}{2\sqrt{\pi}}\left[e^{-X_i{}^2} + \frac{V_{SW}\, cos\theta\sqrt{\pi}}{v_{th_i}}(1 + \mathrm{erf}(X_i))\right] \tag{2.26}$$

As a result, the following simulations on the lunar dayside is performed for three-current problem where $X_i = \frac{V_{bulk}\, cos\theta}{v_{th_i}} - \sqrt{\frac{e\emptyset}{kT_i}} = U_i - \sqrt{\frac{e\emptyset}{kT_i}}$. The dominant charging currents are the collection of electrons and ions from the upstream plasma, and the photoemission of electrons due to the solar UV and X-ray emission and solar flares, whereas the secondary emission is considerably weaker than the other current sources for the plasma conditions considered in this study.

2.3 Negatively Charged Surfaces on the Lunar Dayside and Terminator

The lunar surface becomes positively charged on the lunar dayside near the subsolar point, where the solar zenith angle is equal to 0, since the photoemission of electrons is the dominant charging current. On the other hand, the solar zenith angle increases while approaching to the lunar terminator. Therefore, the incidence angle of the solar irradiation becomes wider while decreasing the photoelectron emission. As a result, the positively charging currents such as J_i and J_{Pe} develop into the levels of the incoming SW electron current, and the positive surface potential starts to reach at zero voltage. On the lunar dayside, a transition region is referred as the "Dead Zone" between positively charged ($\emptyset_s > 0$) and negatively charged ($\emptyset_s < 0$) surfaces by Stubbs et al. (2006). Therefore, it is important to determine the location of this zone since the probe equations are different for the repulsive surfaces to the ambient plasma electrons as well as the photoemission electrons.

For the negatively charged surfaces on the dayside, the surface potential equation is given by Stubbs et al. (2014) as:

$$\emptyset_s = -\frac{k_B T_e}{e} ln\left(\frac{n_{Pe0}}{n_0}\sqrt{\frac{T_{Pe}}{T_e}}\right) = -\frac{k_B T_e}{e} ln\left(\frac{J_{Pe0} cos\theta}{n_0 e}\sqrt{\frac{2\pi m_e}{k_B T_e}}\right) \tag{2.27}$$

The derivation of Equation 2.27 can be shown for the repulsive surfaces ($\emptyset_s \leq 0$) for electrons as:

$$J_{Pe} = -e \int_0^{\infty} f_{Pe}(v_x)\, v_x\, dv_x \tag{2.28}$$

The lower limit of integral is taken as zero since the photoelectrons do not require an initial thermal velocity in order to escape an attractive surface potential in this case.

$$J_{Pe} = -e \int_0^{\infty} n_{Pe0} \left(\frac{m_e}{2\pi k_B T_{Pe}}\right)^{0.5} exp\left\{-\frac{[(1/2) m_e \vec{v}_x{}^2 - e(\emptyset(x) - \emptyset_s)\,]}{k_B T_{Pe}}\right\} v_x\, dv_x \tag{2.29}$$

$$J_{Pe} = -e \left[-\frac{k_B T_{Pe}}{m_e} n_{Pe0} \left(\frac{m_e}{2\pi k_B T_{Pe}}\right)^{0.5} exp\left\{-\frac{[0.5 m_e \vec{v}_x{}^2 - e(\emptyset(x) - \emptyset_s)\,]}{k_B T_{Pe}}\right\}\right]_0^{\infty} \tag{2.30}$$

$$J_{Pe} = -e \left[-n_{Pe0} \left(\frac{k_B T_{Pe}}{2\pi m_e}\right)^{0.5} \left(e^{-\infty} - e^{-\frac{[-e(\emptyset(x) + \emptyset_s)]}{k_B T_{Pe}}}\right)\right] \tag{2.31}$$

Since $\emptyset(0)$ is equal to $\emptyset_s$ at lunar surface (x = 0), the solution can be derived as:

$$J_{Pe} = -e\, n_{Pe0} \left(\frac{k_B T_{Pe}}{2\pi m_e}\right)^{0.5} \tag{2.32}$$

The upper limit of the integral must be $-(2|e\emptyset_s|/m_e)^{0.5}$ for the incoming SW electrons since the negative surface potential repels the incoming electrons. As a results, the electrons must have a certain level of energy in order to reach the lunar surface (equation 2.33). Therefore, the second term of equation 2.3 can be solved for the repulsive surfaces to the electrons as:

$$J_e = -e \int_{-\infty}^{-(2|e\emptyset_s|/m_e)^{0.5}} f_e(v_x)\, v_x\, dv_x \tag{2.33}$$

$$J_e = e \int_{-\infty}^{-(2|e\emptyset_s|/m_e)^{0.5}} n_e \left(\frac{m_e}{2\pi k_B T_e}\right)^{0.5} exp\left\{-\frac{[0.5 m_e \vec{v}_x{}^2 - e\emptyset(x)]}{k_B T_s}\right\} v_x\, dv_x \tag{2.34}$$

$$J_e = e \left[-\frac{k_B T_e}{m_e} n_0 \left(\frac{m_e}{2\pi k_B T_e}\right)^{0.5} exp\left\{-\frac{[(1/2) m_e \vec{v}_x{}^2 - e\emptyset(x)]}{k_B T_e}\right\}\right]_{-\infty}^{-(2|e\emptyset_s|/m_e)^{0.5}} \tag{2.35}$$

$$J_e = e\left[\left(\frac{k_B T_e}{2\pi m_e}\right)^{0.5} n_0\, exp\left\{-\frac{[0.5 m_e \vec{v}_x{}^2 - e\emptyset(x)]}{k_B T_e}\right\}\right]_{-\infty}^{-(2|e\emptyset_s|/m_e)^{0.5}} \tag{2.36}$$

$$J_e = e n_0 \left(\frac{k_B T_e}{2\pi m_e}\right)^{0.5} \exp\left\{-\frac{|e\emptyset_s|}{k_B T_e}\right\} \tag{2.37}$$

Equation 2.3 can be expressed by the combination of equation 2.32 and 2.37 as:

$$-e\, n_{Pe0}\left(\frac{k_B T_{Pe}}{2\pi m_e}\right)^{0.5} + e n_0 \left(\frac{k_B T_e}{2\pi m_e}\right)^{0.5} \exp\left\{-\frac{|e\emptyset_s|}{k_B T_e}\right\} = 0 \tag{2.38}$$

$$n_{Pe0}\left(\frac{k_B T_{Pe_0}}{2\pi m_e}\right)^{0.5} = n_0 \left(\frac{k_B T_e}{2\pi m_e}\right)^{0.5} \exp\left\{-\frac{|e\emptyset_s|}{k_B T_e}\right\} \tag{2.39}$$

$$\ln\left(\frac{n_{Pe0}}{n_0}\sqrt{\frac{T_{Pe0}}{T_e}}\right) = -\frac{|e\emptyset_s|}{k_B T_{Pe}} \tag{2.40}$$

$$\emptyset_s = -\frac{k_B T_e}{e} \ln\left(\frac{n_{Pe0}}{n_0}\sqrt{\frac{T_{Pe0}}{T_e}}\right) \tag{2.41}$$

Equation 2.41 represents an expression for the surface charging of the repulsive surfaces to the electrons on the dayside of the Moon for the reduced problem showed in equation 2.3 under the regular SW conditions. However, we require retrieving an electron photoemission current function depending on the solar zenith angle θ for the simulation; therefore, this term is added similar to the attractive surfaces such as:

$$\emptyset_s = -\frac{k_B T_e}{e} ln\left(-\frac{J_{Pe0} cos\theta}{n_0\, e}\sqrt{\frac{2\pi m_e}{k_B T_e}}\right) \tag{2.42}$$

Furthermore, these equations must be updated according to the flowing plasma equations outside of the regular SW conditions. Therefore, the following equations are included to the current balance code (Manka, 1973), where $X_i = \frac{V_{bulk}\, cos\theta}{v_{th_i}} - \sqrt{\frac{e\emptyset}{kT_i}} = U_i - \sqrt{\frac{e\emptyset}{kT_i}}$ as:

$$J_e = -\frac{n_0 e v_{th_e}}{2\sqrt{\pi}}\left[e^{-X_e{}^2} + U_e\sqrt{\pi}(1 + \mathrm{erf}(X_e))\right] \tag{2.43}$$

$$J_i = \frac{n_0 e V_{SW}\, cos\theta}{2}\left[1 + \mathrm{erf}(U_i) + \frac{1}{U_i\sqrt{\pi}} e^{-U_i{}^2}\right] \tag{2.44}$$

For the surface charging simulations, the secondary electron emission current is not included in this step. When the secondary electron emission is used to calculate the surface potential and the electric field above the lunar terminator, the difference with the three-current problem is calculated as 0.169%. On the other hand, the secondary electron emission is a critical charging mechanism within the empty spaces between the dust particles for the mobilization of the charged grains. Therefore, it is explained in the following section for the dust charging.

2.4 Dead Zone Location

The photoemission current drops rapidly while approaching the lunar terminator since the solar zenith angle becomes 90^o similar to the flowing component of the charging equations related to the SW bulk velocity. The positively charging currents such as the photoemission electrons and the collection of ions reach the same level as the electron current between the subsolar point and the lunar terminator; therefore, a transition region is expected on the lunar surface, which is referred as “dead zone”. The variation of its location is investigated in order to observe its response together with the dust heights above the lunar terminator.

Strong electron currents from the upstream plasma, which are controlled by the plasma density and the electron temperature, can move the dead zone location closer to the subsolar point while expanding the negatively charged surfaces on the lunar dayside. In addition, it can increase the heights of the lofted dust grains since they are negatively charged as well, and the charged dust grains are repelled by the negative surface potential. Since the CME post-shocks are accompanied with warm and dense plasma, they are expected to move the dead zone away from the terminator region. On the other hand, high plasma density has a similar effect on the dead zone during the late CME passages, which can be referred as CME-driver gas, even though it co-occurs with cold electrons.

Equation 2.45 is derived for a quick estimation of its response by the stationary plasma equations:

$$\theta_{DZ} = cos^{-1}\left(\frac{n_0[\sqrt{T_e/m_e} - \sqrt{T_i/m_i}]}{n_{p0}\sqrt{T_{Pe}/m_e}}\right) \quad (2.45)$$

When the relationship between the solar wind bulk velocity and the thermal velocities of ions and electrons is present as $V_{th_e} >> |V_{SW}| >> V_{th_i}$, equation 2.45 can be used to estimate the location of the dead zone under the regular SW conditions of 10.4 eV ion temperature, 12.1 eV electron temperature and 400 km/s SW bulk velocity. On the other hand, high values of the SW bulk velocity and the plasma density are present during the post-shock plasma and CME-driver gas passages of three CME events that are studied in the following sections, which contribute to the flowing component of the charging current equations. Therefore, the difference between equation 2.45 and the solution of the flowing plasma equations can increase up to approximately 10 degree. On the other hand, it can be used for a quick estimation of the dead zone location when the density and the SW flow velocity are unremarkable. The difference between equation 2.45 and the solution of the flowing plasma equations are calculated as low as 6.830×10^{-6} degree, 4.303×10^{-4} degree and 4.781×10^{-5} degree during the early-CME passages of the three CME events in the following section, respectively.

2.5 Lunar Surface Charging Predictions

2.5.1 Solar Wind Cases

Solar wind observations affirm that there is a wide range of variation of physical properties in temporal and spatial scales, which passes throughout the heliosphere including the Earth-Moon system. One of the large-scale observations is slow and fast stream SW, which are originated from the different parts of the Sun. Fast stream SW is radiated from the coronal holes on the Sun, and it has typical velocities of approximately 500-800 km/s. On the other hand, slow stream SW has average velocities of approximately 300-400 km/s, and its origin is not completely determined currently (Denton et al., 2008). Fast stream SW originates from the dark areas that are called coronal holes with lower surface temperature due to higher

charged particle emission, whereas slow stream SW could be emitted from the regions with higher density.

The following results are retrieved from the simulations that are performed on Matlab for the equilibrium conditions of the surface potential, the electric field and Debye length. Debye length is calculated for the photoemission electron sheath above the positively charged surface, whereas the incoming electrons form the electron sheath above the negatively charged surfaces on the lunar dayside and terminator region.

2.5.1.1 Slow Stream Solar Wind

The average parameters for the slow stream SW are given in Table 2.1 (Baumjohann and Treumann, 1997).

Table 2.1: Slow stream SW parameters.

Parameters	Values
Plasma density (#/cm^3)	10.0
Electron temperature (eV)	12.1
Ion temperature (eV)	8.6
SW bulk velocity (km s^{-1})	400
Photoelectron current (A m^{-2})	-4.5 x 10^{-6}

On the subsolar point, the positive surface potential accelerates the incoming electrons approaching to the lunar surface, and the photoemission electrons are trapped near the dayside surface. Since the incoming electron current limits the positive charging of the dayside region, it has a controlling effect on the trapping of photoemission electrons near the dayside region.

The currents of the photoelectron emission and the incoming SW electrons are the dominant sources for the lunar surface charging as well as controlling the location of the dead zone. The subsolar point has a surface potential of +4.267 V, and the lunar terminator surface potential is determined as -47.53 V (Fig 2.2). In addition, the surface electric field values are +4.150 V/m on the subsolar point -5.813 V/m on the terminator region (Fig. 2.4).

Since the subsolar point has a photoelectron sheath above the surface, its thickness is determined as 1.028 m, whereas the incoming SW electrons produce the electron sheath above the lunar terminator with 8.177 m thickness (Table 2.2). While the electron sheath above the surface is dominated by the photoelectron emission on the

subsolar point, the photoelectron sheath disappears when the surface potential alters from positive to negative, and the electron sheath becomes composed of the incoming SW electrons (Fig. 2.3). Fig. 2.5 represents the location of the dead zone as well as the variation of the surface potential and the electric field, where the Sun is in the direction of +x axis.

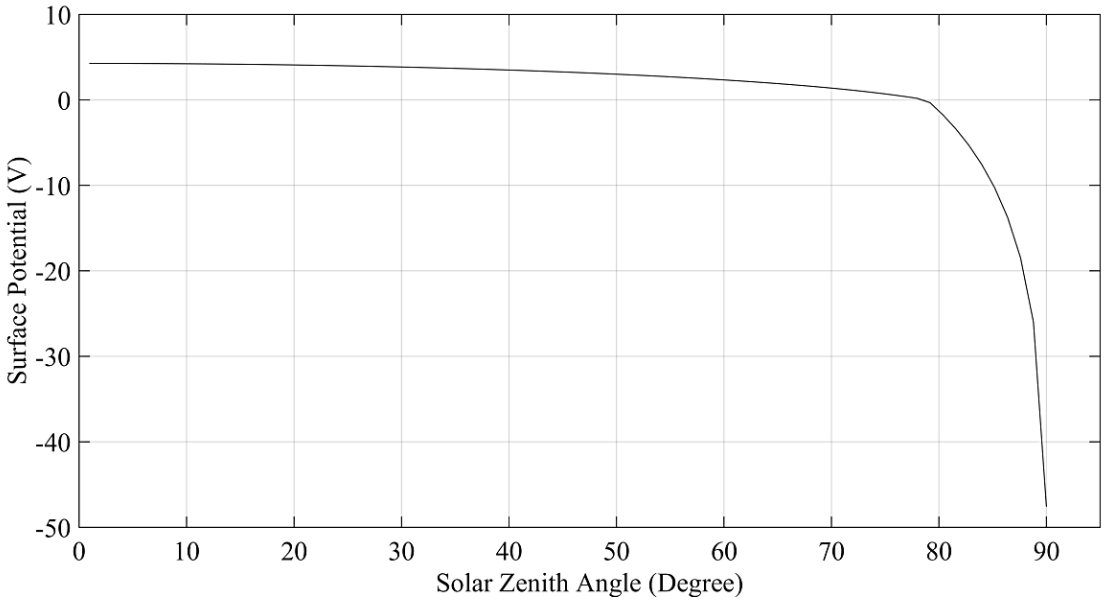

Figure 2.2 : Lunar surface potential from the subsolar point to the terminator region.

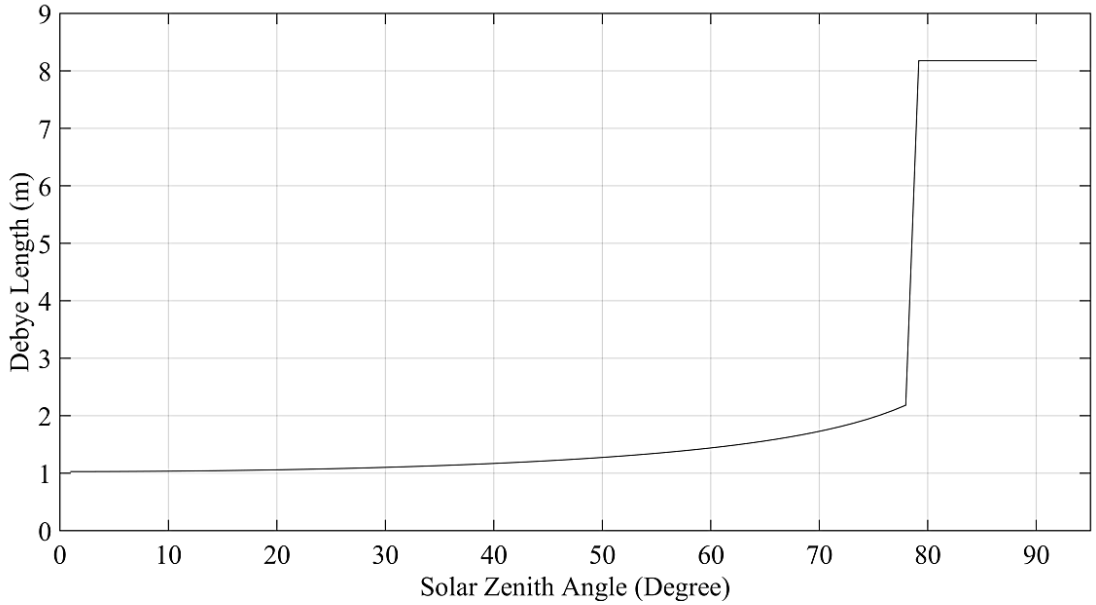

Figure 2.3 : Debye length from the subsolar point to the terminator region.

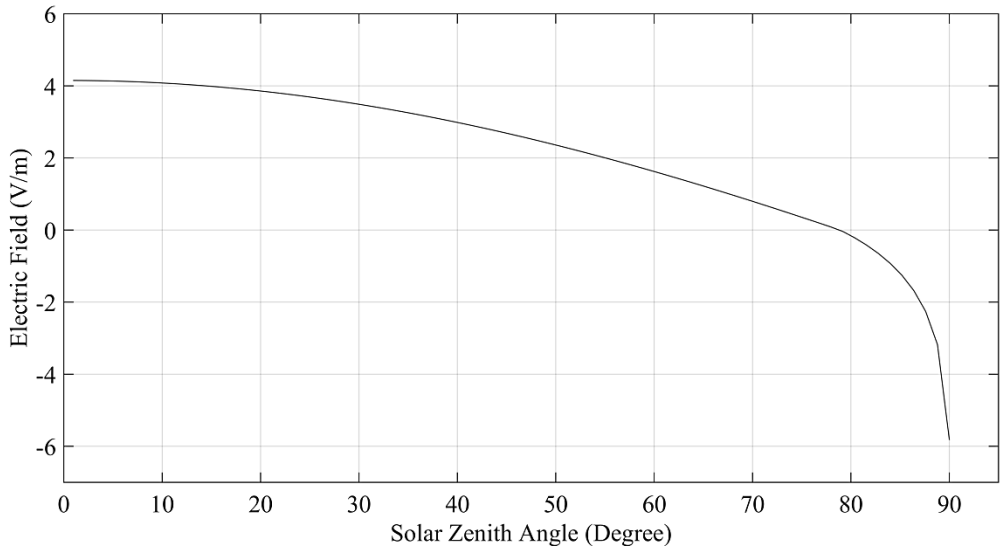

Figure 2.4 : Electric field from the subsolar point to the terminator region.

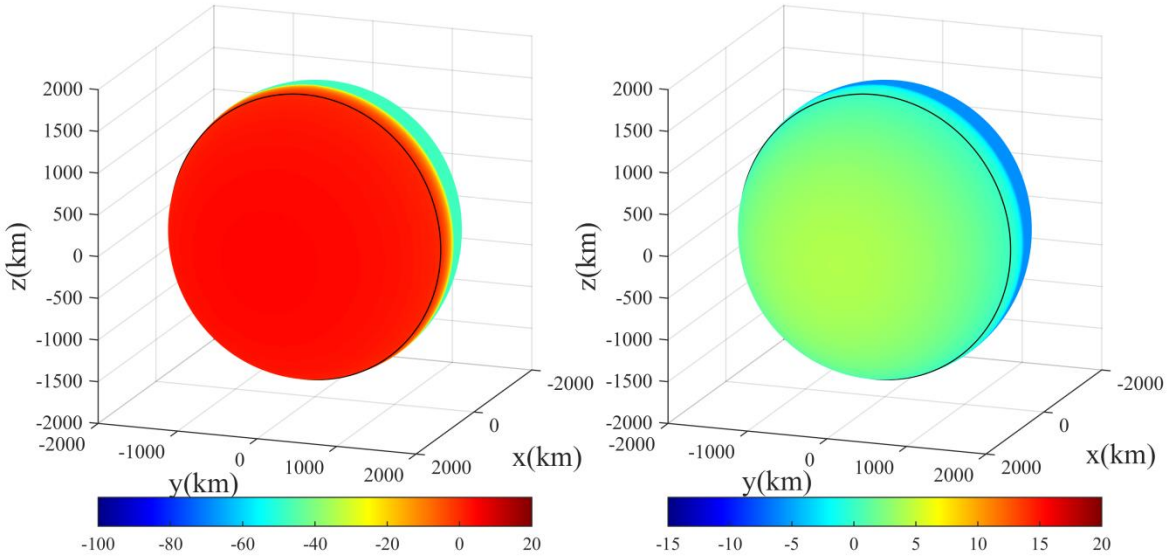

Figure 2.5 : Lunar surface potential (left), electric field (right) and the dead zone location (black line) under slow stream SW.

Table 2.2: The results for the slow stream SW.

Regions	Parameter	Value
Subsolar Point ($\theta=0^o$)	Surface Potential (V)	+4.267
	Debye Length (m)	1.028
	Electric Field (V/m)	+4.150
Intermediate region ($\theta=45^o$)	Surface Potential (V)	+3.259
	Debye Length (m)	1.219
	Electric Field (V/m)	+2.674
Terminator ($\theta=90^o$)	Surface Potential (V)	-47.53
	Debye Length (m)	8.177
	Electric Field (V/m)	-5.813
Dead Zone	Solar Zenith Angle (^{o})	78.83

2.5.1.2 Fast Stream Solar Wind

As it is mentioned before, the fast stream SW has typical velocities of approximately 500-800 km/s and lower plasma density than the slow stream SW. The average parameters for the fast stream SW are given in Table 2.3 (Baumjohann and Treumann, 1997).

Table 2.3: Fast stream SW parameters.

Parameters	Values
Plasma density (#/cm^3)	5.0
Electron temperature (eV)	12.1
Ion temperature (eV)	12.9
SW bulk velocity (km s^{-1})	650
Photoelectron current (A m^{-2})	-4.5 x 10^{-6}

The subsolar point has a surface potential of +6.347 V, and the lunar terminator surface potential is determined as -45.08 V (Fig 2.6). The subsolar surface potential increase due to the enhanced flow velocity of the SW, the warmer ion temperature and the lower plasma density. Since the electron current decreases due to the plasma density, it allows the dayside surface to have stronger positive potential by the photoelectron emission.

It is observed that the density is a critical parameter for the subsolar point potential, whereas the electron temperature is the dominant factor for the surface charging of the terminator region. Since the electron temperature is the same, the results are significantly similar for the lunar terminator surface potential compared to the slow stream SW (Table 2.4).

Table 2.4: The results for the fast stream SW.

Regions	**Parameter**	**Value**
Subsolar Point	Surface Potential (V)	+6.347
(θ=0^o)	Debye Length (m)	1.032
	Electric Field (V/m)	+6.148
Intermediate region	Surface Potential (V)	+ 5.158
(θ=45^o)	Debye Length (m)	1.226
	Electric Field (V/m)	+4.209
Terminator	Surface Potential (V)	-45.08
(θ=90^o)	Debye Length (m)	11.56
	Electric Field (V/m)	-3.898
Dead Zone	Solar Zenith Angle (^{o})	84.38

The surface electric field values are determined as +6.148 V/m on the subsolar point -3.898 V/m on the terminator region (Fig. 2.8). Since the subsolar point has a stronger positive potential, it traps a high number of photoelectrons above the surface. Therefore, the surface potential is stronger than the slow stream SW case. On the other hand, the lunar terminator electric field becomes weaker due to the lower plasma density. Therefore, the electron sheath becomes thicker above the surface.

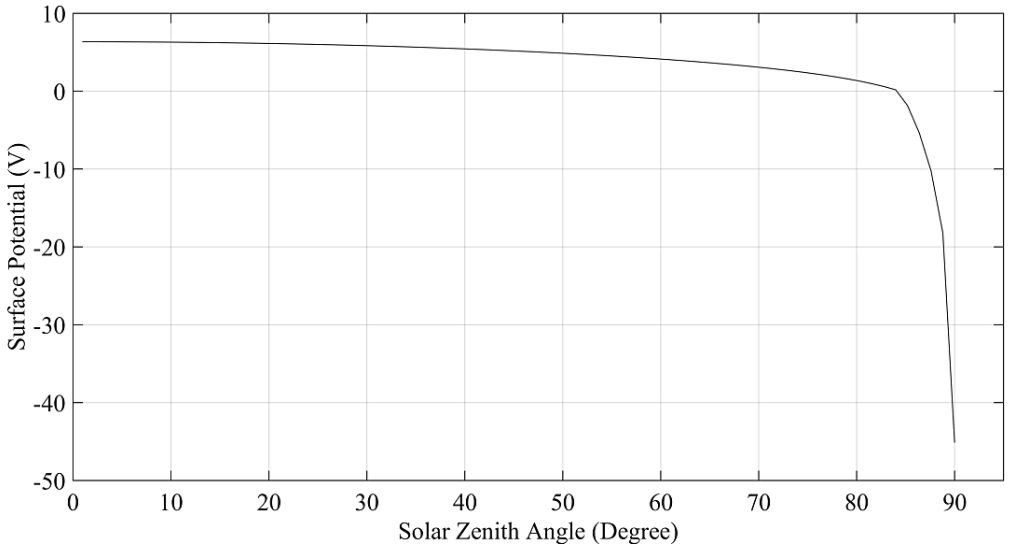

Figure 2.6 : Lunar surface potential from the subsolar point to the terminator region.

Since the subsolar point has a photoelectron sheath above the surface, its thickness is determined as 1.032 m, whereas the incoming SW electrons produce the electron sheath above the lunar terminator with 11.56 m thickness (Fig. 2.7). Fig. 2.9 represents the location of the dead zone as well as the variation of the surface potential and the electric field, where the Sun is in the direction of +x axis.

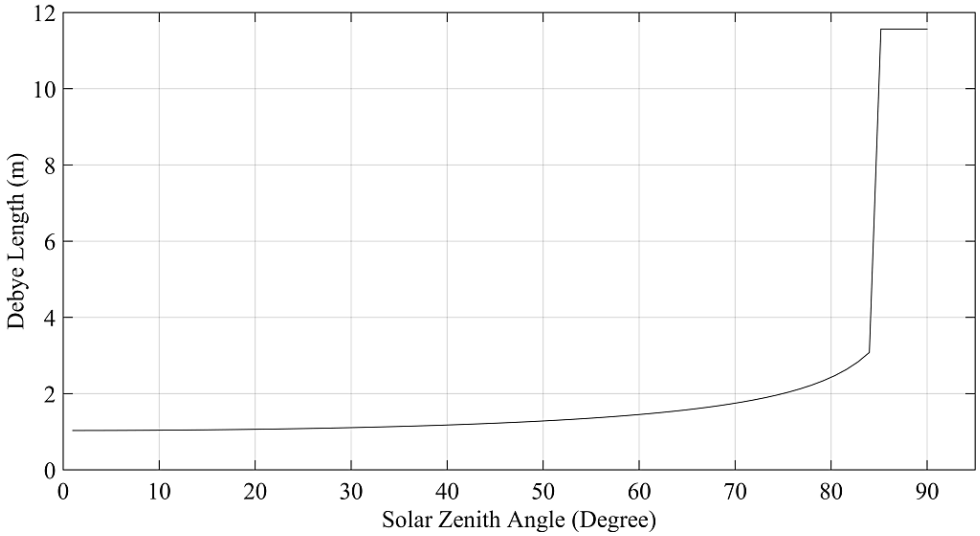

Figure 2.7 : Debye Length from the subsolar point to the terminator region.

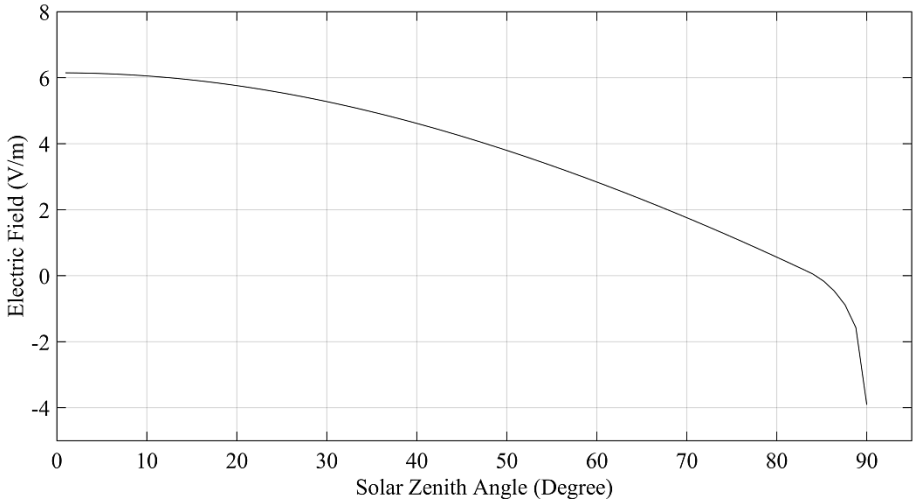

Figure 2.8 : Electric field from the subsolar point to the terminator region.

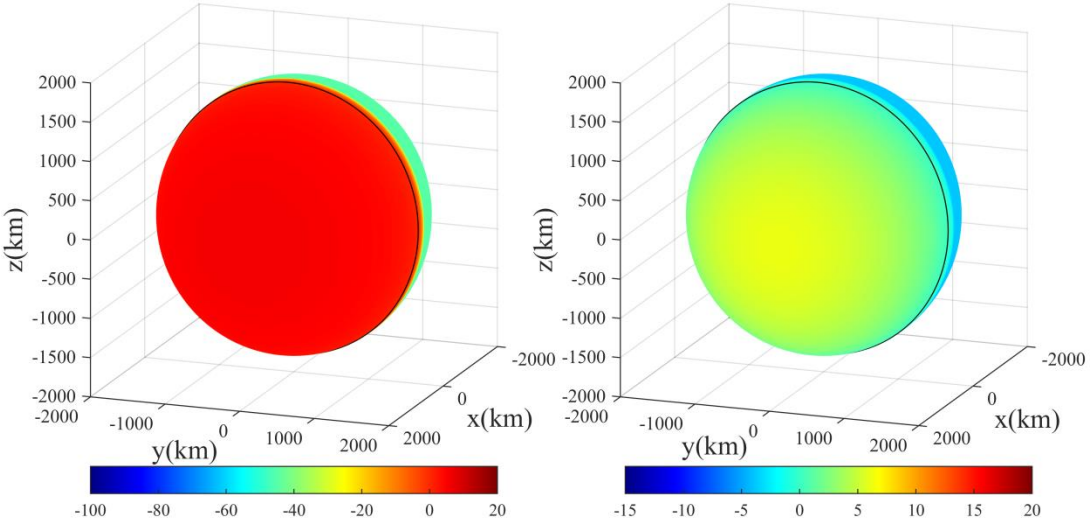

Figure 2.9 : Lunar surface potential (left), electric field (right) and the dead zone location (black line) under the slow stream SW.

2.5.2 Coronal Mass Ejection Events

CMEs are immense releases of plasma and magnetic field from the solar corona, and the lunar surface potential undergoes considerable changes during the CME passages. In addition, CMEs are one of the geomagnetic activity sources as well as their accompanying interplanetary shocks and high-speed SW streams (Brueckner et al., 1998), and solar flares and type II bursts are generally correlated to the fastest CMEs (Sheeley et al., 1999). Since CMEs run into the slower SW flow during their propagation, their speed is not as high as that near the Sun when they reach the Earth-Moon system (Tsurutani and Lakhina, 2014). A high number of CMEs are accompanied by solar flares (Zhang et al., 2001); therefore, lunar dayside charging is affected accordingly by higher photoemission current. Three geo-effective CME

events on 8-13 February 1997, 1-3 May 1998 and 8-12 March 2012 are selected and compared through their charging effect on the lunar surface for the average plasma parameters in this section. These parameters are selected from the intervals of the post-shock plasma passage with high density and temperature, the early-CME with low density and cold plasma, and the late-CME with high density and low temperature that can be referred as CME-driver gas. There was no solar flare occurrence during the first event. On the other hand, the second event was accompanied by an X1 type solar flare during the early CME passage, and there were two X1 type solar flare occurrences during the third event. Their influence on photoemission current is included as described by Farrell et al. (2013).

2.5.2.1 CME Event 1

A geo-effective CME passage is selected from 8 to 13 February 1997 (Bruecker et al., 1998) since its post-shock plasma has higher density than the following CMEs and SW cases. The density reaches the minimum level compared to the other events during the early CME passage with significantly low temperatures. There was no solar flare occurrence as mentioned before. The average plasma parameters are given in Table 2.5 for the CME intervals for the post-shock plasma passage, the early CME and the late CME.

Table 2.5: Average SW parameters of CME event from 8 to 13 February 1997.

Parameters	Post-shock Plasma	Early CME	Late CME
Plasma density (#/cm^3)	49.7	0.2	43.3
Electron temperature (eV)	9.8	4.0	3.5
Ion temperature (eV)	41.7	2.0	1.0
SW bulk velocity (km s^{-1})	477	462	390
Photoelectron current (A m^{-2})	-4.5 x 10^{-6}	-4.5 x 10^{-6}	-4.5 x 10^{-6}

The post-shock plasma passage is accompanied by higher density compared to the regular SW conditions even though the electron temperature is slightly colder. Therefore, the subsolar point potential is +1.230 V, whereas the terminator region has -29.73 V surface potential. Both values are weaker than the SW cases. First, high density of incoming SW electrons limits the positive charging of the dayside. Second, the influence of the SW flow disappears near the lunar terminator, and the electrons reach the surface with their thermal energies. Therefore, it is lower due to colder temperatures compared to the SW electrons.

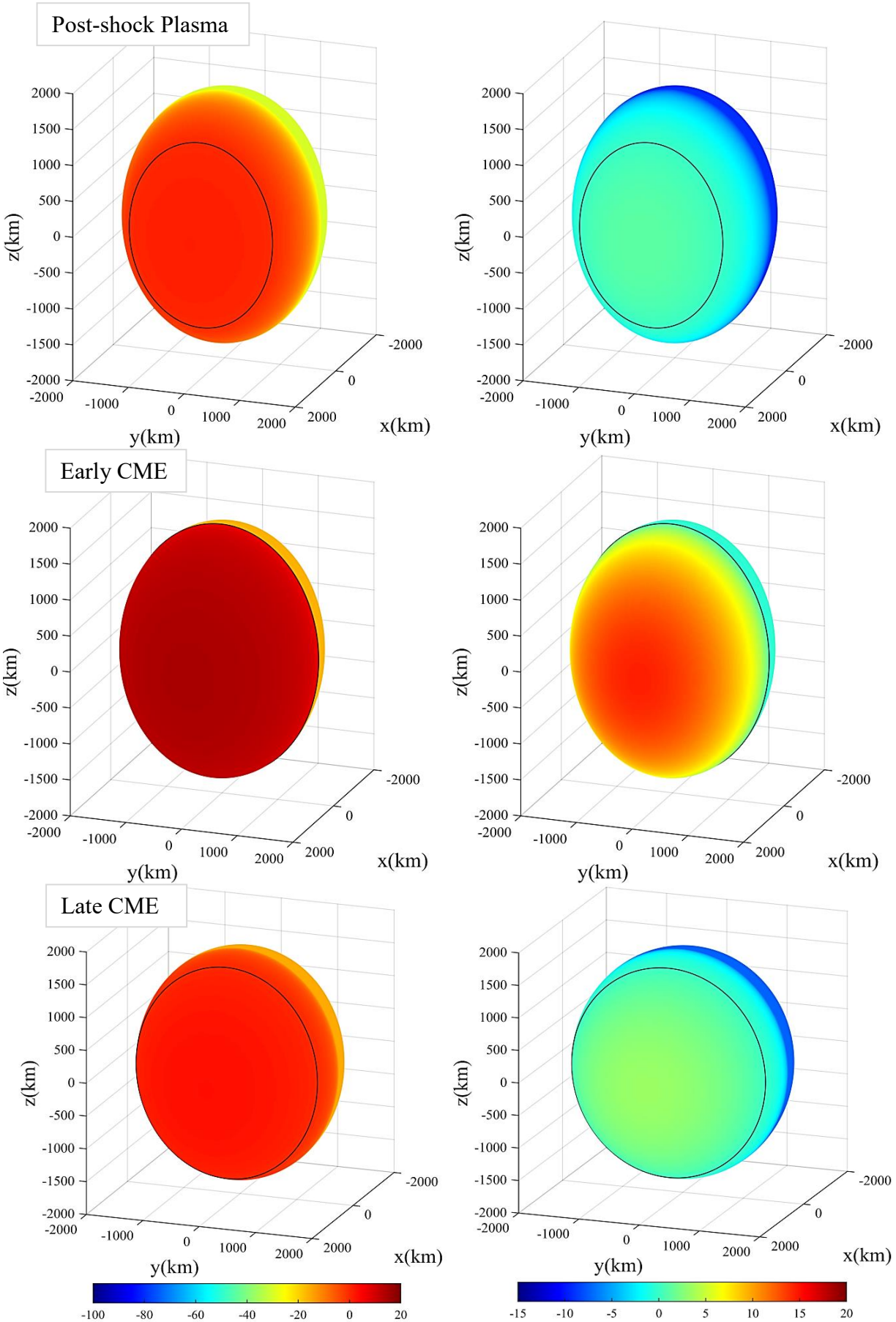

Figure 2.10 : Lunar surface potential (left column), electric field (right column) and the dead zone location (black line) during CME passage.

The electric field is determined as + 1.263 V/m on the subsolar point and -9.006 V/m above the terminator region. A weak positive potential allows a higher percentage of the emitted photoelectrons to escape the subsolar point; therefore, the photoelectron sheath density decreases, whereas its thickness increases. On the other hand, high density of the incoming SW electrons covers the lunar terminator surface with a thin and highly dense electron sheath. Therefore, the electric field becomes enhanced (Fig. 2.10). Furthermore, the negatively charged surfaces expand in the direction of the subsolar region, and the dead zone location is determined as 47.85^{o} that is significantly lower than the SW cases.

The early CME passage represents the nearly-absence of the SW due to the minimum plasma density and the coldest temperatures. Therefore, the photoemission current becomes dominant, and the positively charged surfaces expand in the direction of the lunar terminator while the dead zone location reaches at 89.87^{o}. As a result, the surface potentials are calculated as +15.00 V on the subsolar point and -16.42 V on the terminator region. In addition, only the high-energy tail of the emitted photoelectron distribution can escape the strong positive potential of the subsolar point. For this reason, the electric field evolves into +14.47 V/m. On the other hand, the late CME passage has significantly high density with cold plasma temperatures. Due to high density, the subsolar potential conditions are very similar to the post-shock plasma passage. Even though the terminator surface potential is insignificant, the high density enhances the electric field that is found as -7.260 V/m.

2.5.2.2 CME Event 2

Another geo-effective CME event had occurred from 1 to 3 May 1998 (Farrell et al., 2012, 2013). A solar flare event had occurred during the early CME period on 2 May 1998, and the photoemission current density is increased by a factor of 5 for an X1 type solar flare (Farrell et al., 2013).

Table 2.6: Average SW parameters of CME event from 1 to 3 May 1998.

Parameters	Post-shock Plasma	Early CME	Late CME
Plasma electron density (#/cm^3)	20.0	3.0	50.0
Plasma electron temperature (eV)	14.8	6.6	3.2
Plasma ion temperature (eV)	43.0	6.8	2.6
Solar wind flow velocity (km s^{-1})	600	650	500
Photoelectron current (A m^{-2})	-4.5×10^{-6}	-22.5×10^{-6}	-4.5×10^{-6}

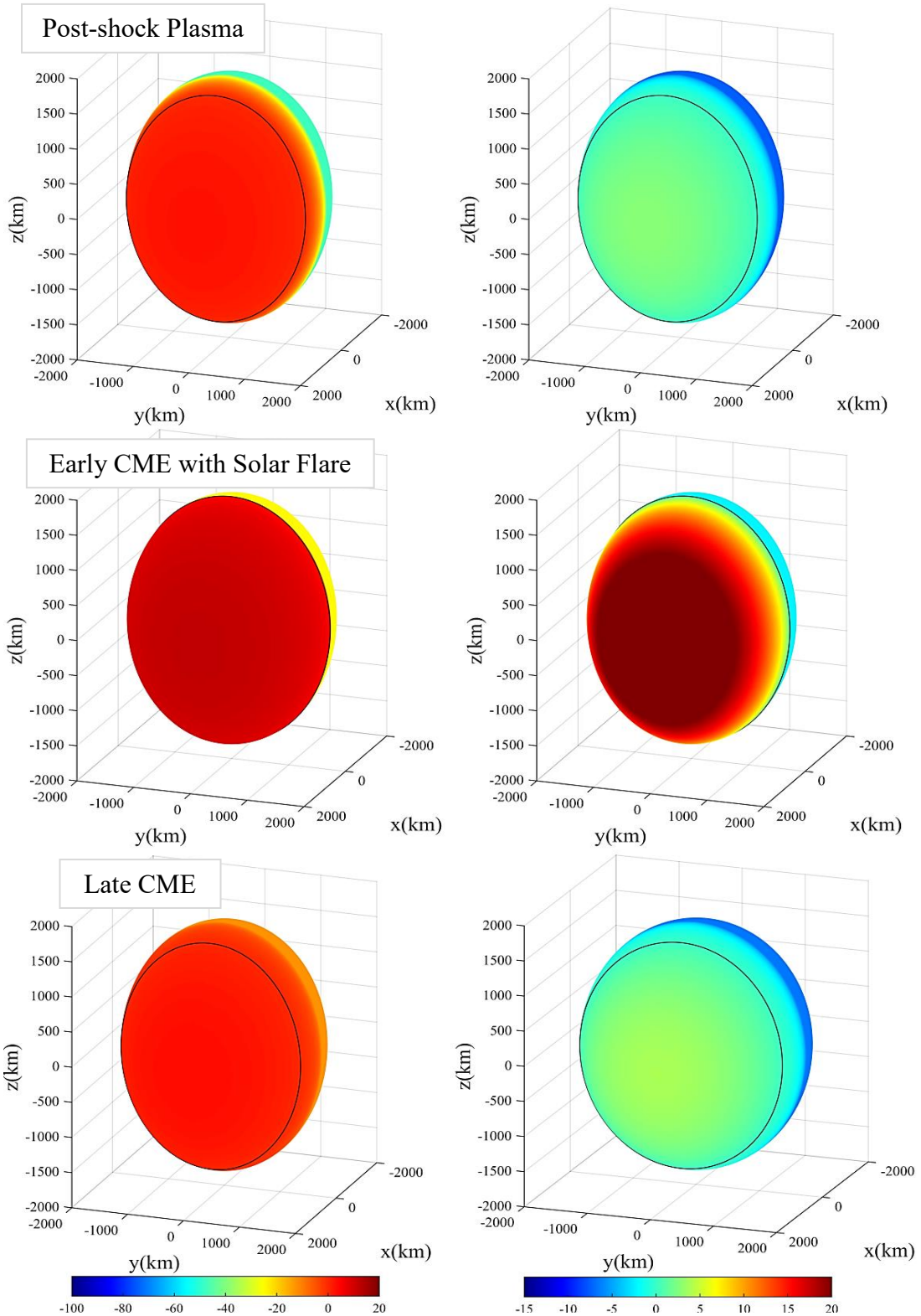

Figure 2.11 : Lunar surface potential (left column), electric field (right column) and the dead zone location (black line) during CME passage.

The electron temperature starts as the regular solar wind conditions, and it reaches approximately 43.0 eV for the ions during post-shock plasma passage while the solar wind velocity is higher than the first event. Terminator surface potential is

significantly similar to the SW case, whereas the electric field is weaker than the first event due to the lower electron density. The early-CME has slightly higher density and warmer plasma temperature than the first event; however, the photoemission current increases due to the solar flare event. A similar surface potential distribution is observed with the nearly-absence of solar wind on the lunar dayside. The surface potential becomes approximately +12 V. Second, the electric field becomes significantly strong on the subsolar point, and it reaches up to +27.81 V/m (Figure 2.11). During the passage of the late CME, the terminator surface potential becomes -12.36 V, whereas the subsolar surface potential is +3.513 V. In addition, the electric field is determined as +3.867 V/m on the subsolar point and -6.571 V/m on the terminator region. Due to the high electron density, the electron sheath thickness is considerably smaller than the SW cases for the lunar terminator, which is 1.881 m. Moreover, the location of the dead zone is found as 67.64^{o}.

2.5.2.3 CME Event 3

The final geo-effective CME event is selected from 8 to 12 March 2012 (Möstl et al., 2014) since its post-shock plasma has higher electron temperature than the previous cases and lower plasma density than the first event. In addition, there were two X1 type solar flare occurrences on 9^{th} and 10^{th} of March. Average plasma parameters of the third CME event intervals in Table 2.7.

Table 2.7: Average SW parameters of CME event from 8 to 12 March 2012.

Parameters	Post-shock Plasma	Early CME 01	Early CME 02	Late CME
Plasma density (#/cm^3)	18.6	7.6	3.2	14.9
Electron temperature (eV)	30.8	6.6	3.0	7.9
Ion temperature (eV)	49.3	16.5	0.57	9.7
SW flow velocity (km s^{-1})	752	702	489	454
Photoelectron current (A m^{-2})	-4.5 x 10^{-6}	-22.5 x 10^{-6}	-22.5 x 10^{-6}	-4.5 x 10^{-6}

During the first interval, the plasma density is lower than the previous post-shock plasma passages even though the electron temperature is approximately three times of the post-shock plasma of the first event. As a result, the terminator region surface potential is calculated as -108.5 V together with -11.34 V/m electric field. On the other hand, the subsolar surface potential decreases to +2.023 V while the electric field becomes as low as +1.962 V/m.

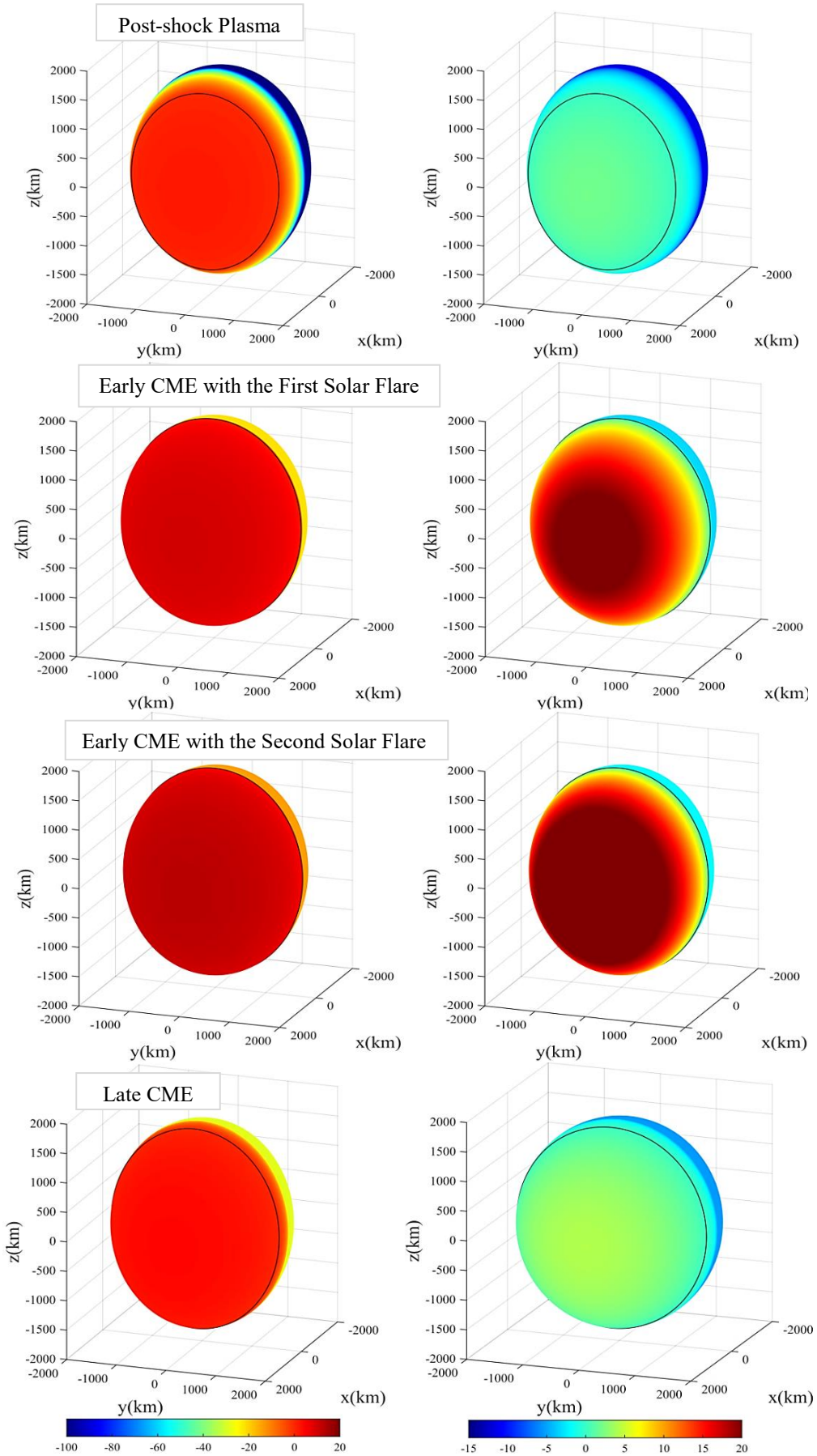

Figure 2.12 : Lunar surface potential (left column), electric field (right column) and the dead zone location (black line) during CME passage.

During the first X1 type solar flare event, the photoemission of electron increases significantly, whereas the electron current to the surface is weak due to cold electron temperature and low plasma density. Therefore, the lunar dayside has high positive surface potential as well as strong electric field. The surface potential is determined as +10.35 V on the subsolar point and – 21.78 V on the lunar terminator. In addition, the electric field has values of +22.36 V/m and -3.144 V/m on the subsolar point and lunar terminator, respectively. Furthermore, the dead zone location is calculated as 88.72^{o}. During the second X1 type solar flare occurence, the SW parameters decline further (Table 2.7). Therefore, the terminator surface potential and electric field weaken significantly, which are calculated as -13.76 V and -1.912 V/m. On the other hand, the increased photoemission due to the solar flare and the absence of a strong upstream plasma flow allow the subsolar surface potential to increase up to +13.20 V. While the subsolar point electric field develops into +28.51 V/m, the dead zone location is transferred to 89.63^{o}.

The upstream parameters are significantly similar to the regular SW condition during the late CME interval. Even though the plasma temperature is slightly colder than the SW case, it considerably resembles to the slow stream SW. As a result, the terminator region surface potential is calculated as -28.88 V together with -5.334 V/m electric field. On the other hand, the subsolar surface potential decreases to +4.208 V while the electric field is calculated as +4.130 V/m.

3. ELECTROSTATIC LUNAR DUST TRANSPORTATION

3.1 Introduction

The current balance method is used to estimate the lunar surface conditions in the previous section, and the role of the surface potential and the electric field on the dust lofting is investigated in this section by estimating the initial launching and the maximum heights of the lofted dust grains under various ambient plasma conditions. The surface electric field cannot loft the charged dust particles, which are attached to the lunar surface and each other, without considering the repulsion between the charged dust grains since the contact forces are significantly stronger than the electrostatic force due to the surface electric field.

In this section, the initial separation of the charged dust grains on the lunar surface is explained in detail. First, the charging mechanism on the patch surfaces within the microcavities between the neighboring dust grains is described. Second, the charging requirement in order to launch a dust grain is expressed as a function of the related parameters such as the microcavity size, the surface cleanliness, the emitted electron temperature, the dust density and so on. Third, the initial launching velocities are estimated by the conservation of the energy, and the charging time of the dust grains are estimated by the time dependence of the electric field within the gap between particles. Finally, the maximum reachable heights are estimated for the dust grains with 0.1, 1 and 5 μm radius, and the regular SW conditions are used as well as 5-minute intervals of the CME event data in order to observe the influence of the charging time related to the particle size and the upstream plasma parameters.

3.2 Simulation Method

3.2.1 Lunar Dust Charging and Initial Separation

Recent laboratory experiments have demonstrated that dust grains can be launched from a dusty surface due to charging within microcavities between the particles by the photoemission of electrons and/or the secondary electron emission (Fig. 3.1), and

a patched dust charging model is suggested as (Wang et al., 2016; Schwan et al., 2017):

$$Q_{microcavity} = -0.5\eta C T_{ee} \tag{3.1}$$

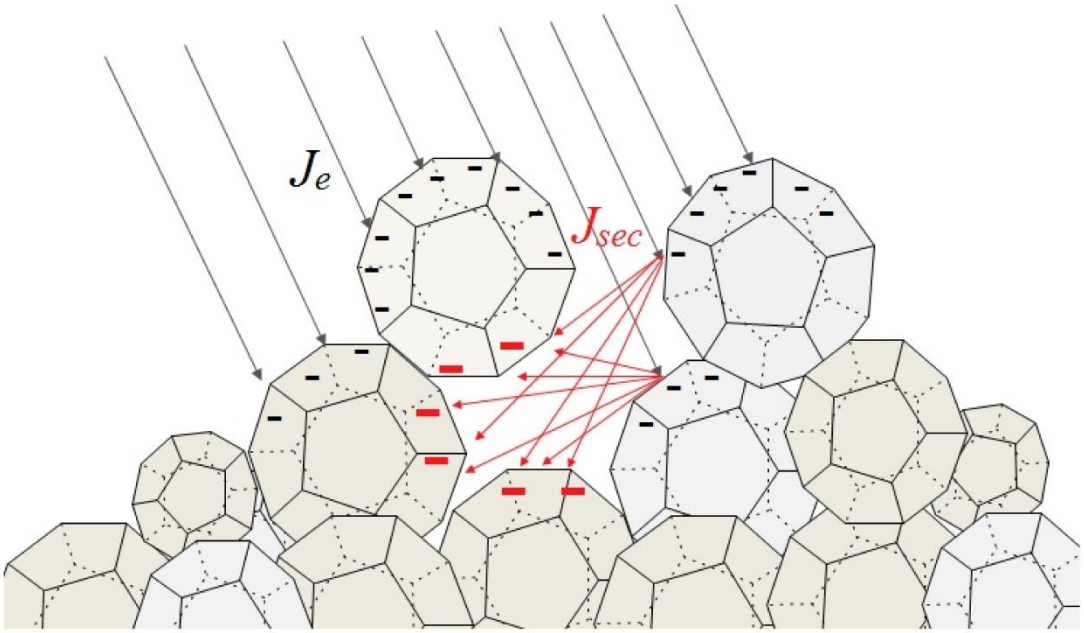

Figure 3.1 : Patched-surface charging within a single microcavity.

Equation 3.1 uses the enhanced charging number within the microcavities η to consider the absorption of the emitted electrons in the high-energy tail of the electron energy distribution, the capacitance of a dust grain C and the emitted electron temperature from the neighboring dust grains T_{ee}. The resulting repulsive force due to the patched surface charging and the charge collection rates on the patch surfaces are modified depending on the several factors such as the particle-particle distance, the emitted electron temperature, the number of microcavities, and the secondary electron emission current density. To simplify the problem, the following calculations are performed for the isolated dust particles, which are charged within a single microcavity separated by a distance s.

The force equilibrium can be given for a single dust particle resting on the lunar surface as:

$$F_{Coulomb} + F_{EF} + F_{contact} + F_{gravity} \tag{3.2}$$

$F_{contact}$ is the contact forces between the dust grain surfaces, and it is assumed as the cohesive force between two spherical particles. In addition, C is calculated with

Hamaker constant, and S is the surface cleanliness of the dust grains (Perko et al., 2001; Hartzell and Scheeres, 2011; Hartzell et al., 2017).

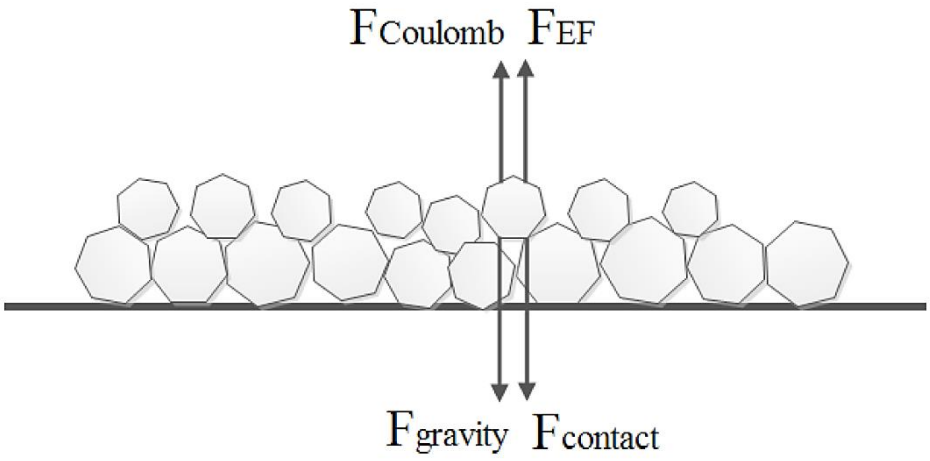

Figure 3.2 : Force equilibrium of dust grains.

$$F_{contact} = CS^2(2a) \tag{3.3}$$

$F_{Coulomb}$ is estimated as the repulsive force due to charge accumulation within the microcavity between two neighboring dust grains (Wang et al., 2016), and $F_{gravity}$ is the gravity force. F_{EF} is the electrostatic force due to the terminator electric field, which is assumed as the force influencing the half of the particle surface on the top that is exposed to the incoming electrons from the ambient plasma and the surface electric field.

$$F_{EF} = E_0 Q_{top\_surface} = E_0 \varepsilon_0 \int_0^{\frac{\pi}{2}} 2\pi a^2 \, E_0 cos\alpha \, d\alpha = 2\pi a^2 \varepsilon_0 E_0^2 \tag{3.4}$$

To release a particle from the lunar terminator, the following condition must be met as below:

$$F_{Coulomb} + F_{EF} > F_{contact} + F_{gravity} \tag{3.5}$$

$$k_e(\frac{Q_{microcavity}}{s})^2 + 2\pi a^2 \varepsilon_0 E_0^2 > CS^2(2a) + \frac{4}{3}\pi a^3 \rho_{dust} g_{lunar} \tag{3.6}$$

$$\left(\frac{-0.5\eta(4\pi\varepsilon_0 a)T_{ee}}{s}\right)^2 > \frac{1}{k_e}\left(CS^2(2a) + \frac{4}{3}\pi a^3 \rho_{dust} g_{lunar} - 2\pi a^2 \varepsilon_0 E_0^2\right) \quad (3.7)$$

k_e is Coulomb's constant, and a is the radius of a single dust grain. In addition, equation 3.8 uses the mass density of the dust grains ρ_{dust}, which is approximately $3 \times 10^3\ kg/m^3$ (Heiken et al., 1991), and the gravity acceleration of g_{lunar} that is approximately 1/6 that of the gravity acceleration in the laboratory experiments.

The requirement of the enhanced charging number η to detach a single dust grain from the lunar surface with the microcavity size s can be estimated as:

$$\eta > \frac{s}{T_{ee}}\sqrt{\frac{2CS^2}{\pi\varepsilon_0 a} + \frac{4a\rho_{dust} g_{lunar}}{3\varepsilon_0} - 2E_0^2} \quad (3.8)$$

$$Q_{microcavity} = -\left(\left\lfloor \frac{0.5CT_{ee}}{e}\left(\frac{s}{T_{ee}}\sqrt{\frac{2CS^2}{\pi\varepsilon_0 a} + \frac{4a\rho_{dust} g_{lunar}}{3\varepsilon_0} - 2E_0^2}\right)\right\rfloor + 1\right)e \quad (3.9)$$

Equation 3.9 shows the charge accumulated within the microcavity that can mobilize a dust grain by exceeding the forces of gravity and contact. First, the maximum charge that can be collected while remaining attached to the surface is calculated as the number of collected electrons. Since the number of the absorbed electrons can only be integer, the floor function is used to find the integer part of the charge requirement, and it is increased by one electron to match the condition given in equation 3.5. As a result, the initial charge of the launched dust grains can be given as:

$$Q_{dust\_initial} = Q_{microcavity} + Q_{top\_surface} \quad (3.10)$$

$$Q_{dust\_initial} = -\left(\left\lfloor \frac{0.5CT_{ee}}{e}\left(\frac{s}{T_{ee}}\sqrt{\frac{2CS^2}{\pi\varepsilon_0 a} + \frac{4a\rho_{dust} g_{lunar}}{3\varepsilon_0} - 2E_0^2}\right)\right\rfloor + 1\right)e + 2\pi a^2 \varepsilon_0 E_0 \quad (3.11)$$

Surface cleanliness S is assumed as 0.13 in the vacuum chamber experiments (Wang et al., 2016), and this parameter is estimated as 0.88 for the lunar dayside and 0.75 for the lunar night side (Perko et al., 2001). Since this parameter is considerably

higher on the lunar surface due to the high vacuum condition, stronger charging is required in order to detach a dust particle on the Moon even though the lunar gravity acceleration is approximately 1/6 that of the acceleration due to gravity in the laboratory experiments. The results are given in Fig. 3.3 by the estimation of enhanced charging number under the slow stream SW on the lunar terminator region and the vacuum chamber conditions with 450 eV electrons and approximately 8400 V/m surface electric field strength that is similar to the experimental conditions.

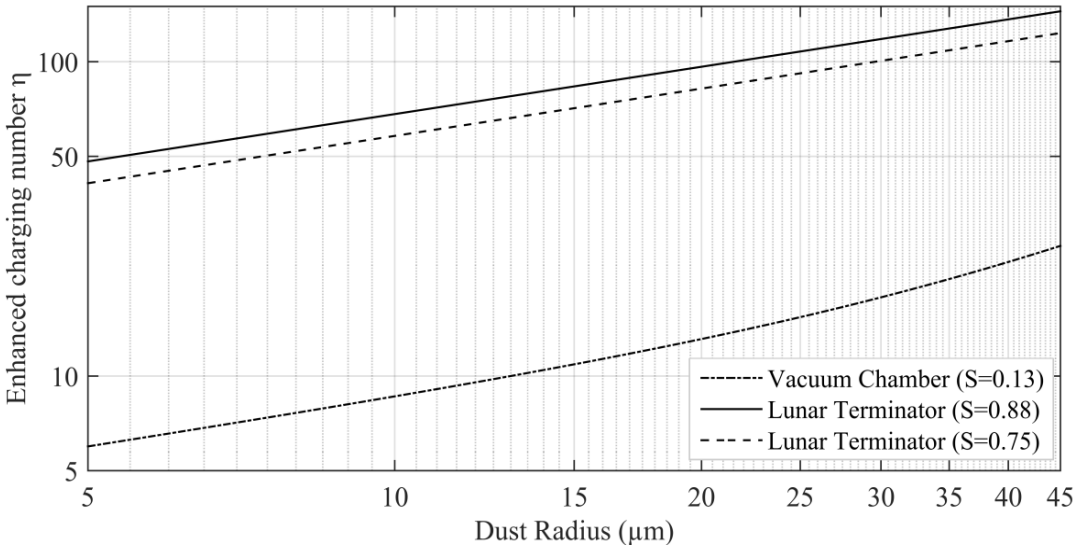

Figure 3.3 : Estimation of enhanced charging number η for the vacuum chamber condition, the lunar dayside and night side.

Initial velocity v_0 of a launched particle can be estimated by assuming that all the electrostatic energy transforms into kinetic energy as:

$$0.5m_{dust}v_0^2 = \sum E_{Es} - \sum W \tag{3.12}$$

It is estimated as the sum of the potential energy of the electrostatic repulsion within the microcavity and the additional input from the surface electric field E_{Es} and the work done against the gravity and the contact forces W.

$$v_{0x}^2 + v_{0y}^2 + v_{0z}^2 = \frac{2}{m_{dust}}(\sum E_{Es} - \sum W) \tag{3.13}$$

$$v_{0z} = [\frac{2}{m_{dust}}(\frac{Q_{microcavity}^2}{4\pi\varepsilon_0 s} + (2\pi\varepsilon_0 a^2 E_0^2 - m_{dust}g_{lunar})d_1 - 2CS^2 a d_2)]^{0.5} \tag{3.14}$$

For the maximum height calculation, v_{0x} and v_{0y} are assumed as 0 in equation 3.13 since a particle reaches its maximum height h_{max} after being launched vertically from the surface. d_1 is the approximate distance for the electrostatic potential energy to transform into kinetic energy, which is estimated as $100s$. For micron and submicron-sized grains, it is seen that $h_{max} >> d_1$ and $\lambda_D >> d_1$. In addition, d_2 is the separation distance from the contact forces, and it is suggested as several dozens of nanometers to cancel the contact forces for a dust particle (Popel et al., 2016).

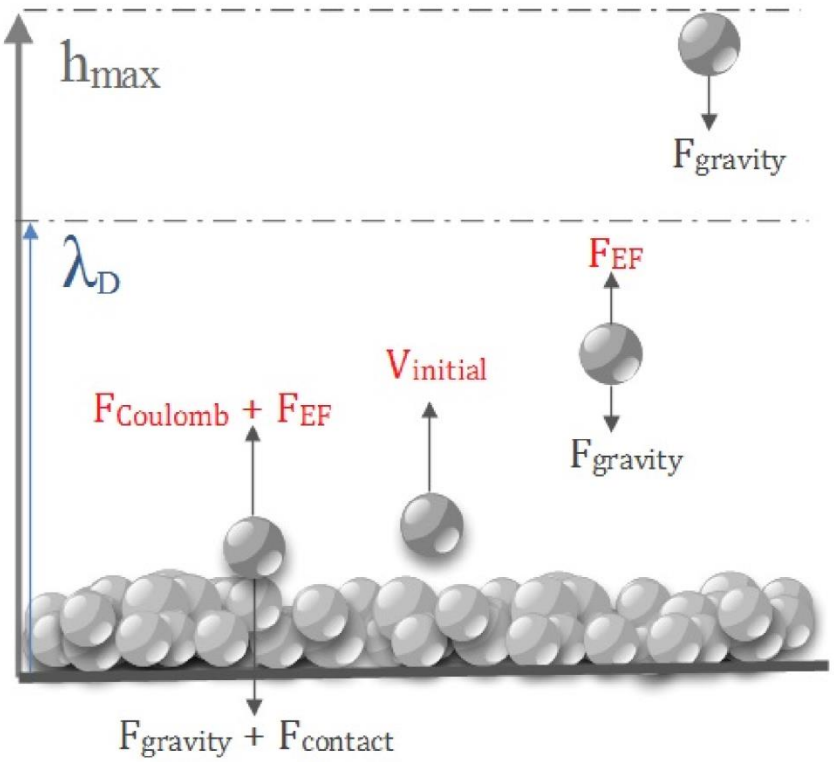

Figure 3.4 : Lofting of lunar dust grains from the surface.

Depending on the electrostatic acceleration and the lunar gravity, the dust particles can have different behaviors within the electron sheath above the lunar terminator after they are launched (Fig. 3.4). These conditions can be explained as below:

• Condition 1: Dust particles can leave the electron sheath while accelerating or maintaining similar velocities to the initial vertical launching velocities ($a_{dust} = \frac{Q_{dust}E_0}{m_{dust}} - g_{lunar} \geq 0$).

• Condition 2: Some of the dust particles reach lower heights than Debye length, or they depart from the electron sheath with lower velocities than the initial vertical velocity ($a_{dust} = \frac{Q_{dust}E_0}{m_{dust}} - g_{lunar} < 0$). Therefore, they can be expressed as:

1. Dust particles leaving the electron sheath after decelerating ($h_{max} > \lambda_D$).

2. Dust particles reaching zero velocity within the sheath ($h_{max} < \lambda_D$).

The particles with 0.1 μm radius are accelerated within the electron sheath in the following calculations (Condition 1), whereas the dust grains with 1 μm radius are decelerated in the simulations most of the time (Condition 2.1) except the post-shock plasma passages (Condition 1). On the other hand, the dust grains 5 μm in radius always reach the zero velocity within the electron sheath (Condition 2.2).

Since the charge magnitudes of the dust grains evolve over time, the vertical motion of the dust grains within the electron sheath is calculated by the charging current sources, the initial charge magnitude of the detached dust grains, the surface electric field and the initial vertical launching velocity with a time step of 10^{-4} s. The electron current I_e, the ion current I_i, the photoemission current I_{ph} and the second electron emission current I_{sec} are used from the well-known equations to calculate the variation of the dust charge (Manka, 1973; Goertz, 1989; Vaverka et al., 2016; Miyake et al., 2018).

$$\frac{dQ_{dust}(t)}{dt} = I_e(\mathrm{t}) + I_i(\mathrm{t}) + I_{ph}(\mathrm{t}) + I_{sec}(\mathrm{t}) \tag{3.15}$$

$$a_{dust}(t) = \frac{(Q_{dust}(t-1) + dQ_{dust}(t))E_0 - F_{gravity}}{m_{dust}} \tag{3.16}$$

$$V(t) = V(t-1) + a_{dust}(t) * \delta t \tag{3.17}$$

3.2.2 Microcavity Size Selection

The particle-particle distance can be modified due to the packing density of the dust grains, whereas the contact forces can vary orders of magnitude by the contact areas between the dust grains on the lunar surface (Cooper et al., 2001; Wang et al., 2016). If we assume that the particles are charged within a single microcavity, various sizes of the microcavities can be used to calculate the resulting charging requirements for the initial launching and the motion of the dust grains within the electron sheath. Slow stream SW conditions are used to estimate the enhanced charging number η, the initial charge values of detached dust grains, the initial vertical launching

velocities and the maximum heights by modifying the size of the microcavity in Table 3.1-3.4 for the lunar terminator region.

Table 3.1 : Estimated initial charges (C) with varius microcavity sizes *s*.

Dust radius a	$s = a$	$s = 2a$	$s = 3a$
0.1 μm	4.054×10^{-17}	8.091×10^{-17}	1.213×10^{-16}
1 μm	1.277×10^{-15}	2.554×10^{-15}	3.831×10^{-15}
5 μm	1.428×10^{-14}	2.856×10^{-14}	4.284×10^{-14}

Table 3.2 : Estimated enhanced charging number η with varius microcavity sizes *s*.

Dust radius a	$s = a$	$s = 2a$	$s = 3a$
0.1 μm	4.601	6.667	8.234
1 μm	1.520	2.155	2.641
5 μm	0.681	0.964	1.181

Table 3.3 : Estimated initial vertical launching velocities (m/s) with varius microcavity sizes *s*.

Dust radius a	$s = a$	$s = 2a$	$s = 3a$
0.1 μm	95.37	191.2	287.1
1 μm	1.098	4.626	10.56
5 μm	0.150	0.310	0.480

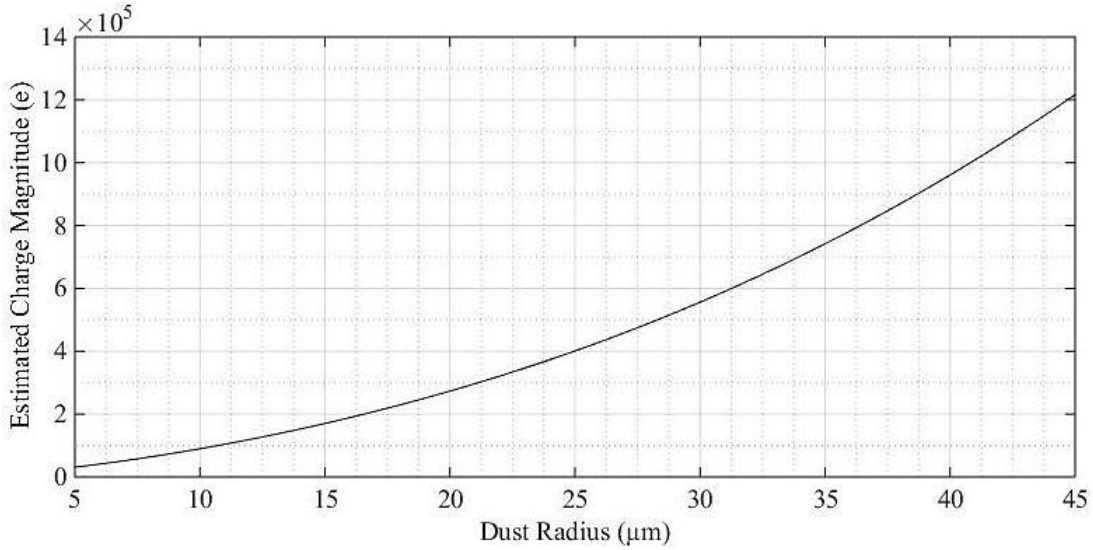

Figure 3.5 : Estimated charges (e) of the lofted dust grains in the vacuum chamber experiments.

The similar heights to the LHG observations of the Surveyor missions are estimated for the microcavity sizes as the particle diameter (Table 3.3). In addition, Schawn et al. (2017) measured the charges of the silica microspheres with approximately 21.2 μm radius as well as irregular-shaped particles in the vacuum chamber, and the

results show that all particles have charges larger than 10^5 e. Moreover, the mean value of the measured silica dust charge magnitude is slightly lower than 3.0×10^5 e in Fig. 3.6 (Schwan et al., 2017), whereas the estimated value is approximately $4.682 \times 10^{-14} C$ (2.922×10^5 e) charge by Eq. (8) in Fig 3.5 for the vacuum chamber conditions with the surface cleanliness parameter as $S = 0.13$.

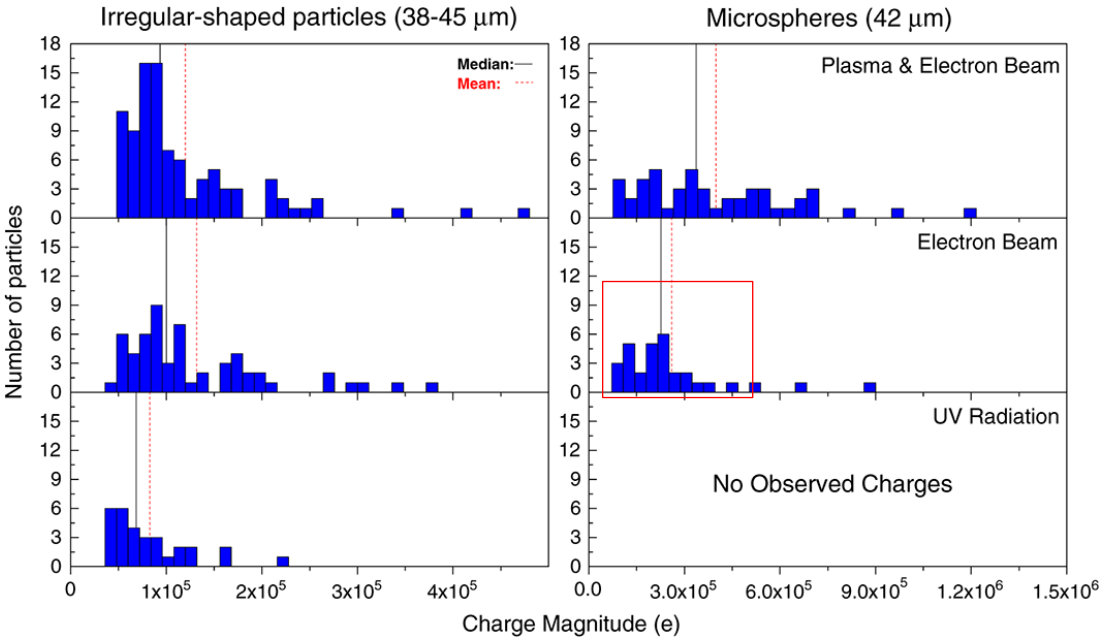

Figure 3.6 : Direct measurements of charge states of microspheres (Schawn et al., 2017).

For these reasons, the following calculations are performed for the microcavity size as the particle diameter. In addition, Wang et al. (2016) concluded that lunar dust grains 2.5 μm in radius can reach approximately 0.11 m height with the particle charge of $4.4 \times 10^{-15} C$, and the dust particles with 5 μm radius would reach these altitudes with approximately $1.75 \times 10^{-14} C$ charge ($\eta \approx 21$ for $T_{ee} = 3$ eV). Since the charging constraint from equation 3.8 is used to estimate the patch surface charging to launch the dust grains by exceeding the forces of contact and gravity, the resulting charge estimations are in the same range but higher than these values for the same particle sizes.

The variation of contact forces can alter these values further. For instance, the charge magnitude to loft a dust particle with 5 μm radius becomes $9.032 \times 10^{-15} C$ ($\eta \approx 12.99$) if the contact forces are decreased by one order of magnitude. For this reason, the initial vertical launching velocity and the maximum height can be determined as approximately 0.30 m/s and 0.03 m. Furthermore, if the contact force

is multiplied by two, the required charge magnitude to separate the dust grain becomes $4.039 \times 10^{-14} C$ ($\eta \approx 58.08$). As a result, it becomes difficult to launch the dust grains, and the separated particles would have 1.363 m/s initial launching velocities and reach 0.640 m height.

Table 3.4 : Estimated initial forces (N) for the dust grains on the lunar terminator surface.

	$F_{contact}$	$F_{gravity}$	F_{EF}	$F_{Coulomb}$
0.1 μm	1.4659×10^{-9}	2.0138×10^{-17}	1.6289×10^{-23}	1.4709×10^{-9}
1 μm	1.4659×10^{-8}	2.0138×10^{-14}	1.6289×10^{-21}	1.4660×10^{-8}
5 μm	7.3295×10^{-8}	2.5172×10^{-12}	4.0723×10^{-20}	7.3297×10^{-8}

For the particle sizes considered in Table 3.4, the surface electric field has significantly low influence on the initial separation of the dust particles; however, it can be an important factor during the laboratory experiments. In the following calculations, the patched surface charging within a single microcavity and the dust grains separated by a distance as the particle diameter are used. The estimated initial forces are presented for the particles with 0.1, 1 and 5 μm radius in Table 3.4.

3.2.3 Charging Time of the Dust Grains

Charging time of the dust grains must be considered in order to start the calculation of the dust velocity and height. According to the previous studies, the time required to reach equilibrium potential for smaller-sized dust grains is considerably longer than the charging time of the larger particles (Goertz, 1989; Vaverka et al., 2016; Zimmerman et al., 2016). In the simulations, the simple one-dimensional wall-charging model is used to calculate the formation of the electric field between the dust grains separated by a microcavity, and the secondary electron emission is used as the charging current source. The time dependence of the electric field within the gap between particles is expressed as (Zimmerman et al., 2016):

$$E(t) = -\frac{U_{th}}{eL} ln(1 + \frac{j_{th} eL}{\varepsilon_0 U_{th}}) \tag{3.18}$$

It should be noted that the electrical conductivity of the charged dust grains is not taken into account during the simulations. L is the characteristic distance of the

microcavity, which is taken as the particle diameter, e is the electron charge with $U_{th} = \frac{m_e V_{th}^2}{2}$.

$$t_{5\mu m} < t_{1\mu m} < t_{0.1\mu m} \tag{3.19}$$

$$J_{sec} = 3.7\ \delta_m J_e \exp\left\{-\frac{|e\emptyset_s|}{k_B T_e}\right\}\left(\frac{E_m}{4k_B T_e}\right)^2 \int_0^\infty u^5 \exp\left\{-\left(\frac{E_m}{4k_B T_e}u^2 + u\right)\right\} du \tag{3.20}$$

For this reason, the dust grains 0.1 μm in radius are launched from the surface less frequently than the micron-sized particles since submicron-sized dust grains collect the required charges on the patch surfaces from minutes to hours depending on the secondary electron emission current (equation 3.20). On the other hand, charging times of micron-sized dust grains are calculated as varying from seconds to minutes. Therefore, if the dust grain is not able to collect sufficient charge in the current simulation step, it is transferred to the next iteration with a condition of taking less total time of terminator region passage over a region 4^o wide, which is approximately 130 km (Vaverka et al., 2016). In addition, the lunar terminator moves around 4.1 m/s at the equator (Berg, 1978); therefore, it takes approximately 8.216 hours.

3.3 Maximum Height Estimations

3.3.1 Solar Wind

Apollo observations suggested that dust grains between 0.1-1 μm in radius were responsible for the high-altitude lunar horizon glow, whereas the dust grains with approximately 5 μm radius scattered the sunlight during Surveyor observations near the surface on the western horizon. Therefore, the calculations are performed for the dust grains with 0.1, 1 and 5 μm radius.

The enhanced charging number η is calculated as approximately 5.817, 18.37 and 41.07 for 0.1, 1 and 5 μm radius dust grains respectively. In addition, the maximum value of the initial vertical velocity is found as 6.670 m/s, 2.155 m/s and 0.964 m/s for 0.1, 1 and 5 μm radius dust grains.

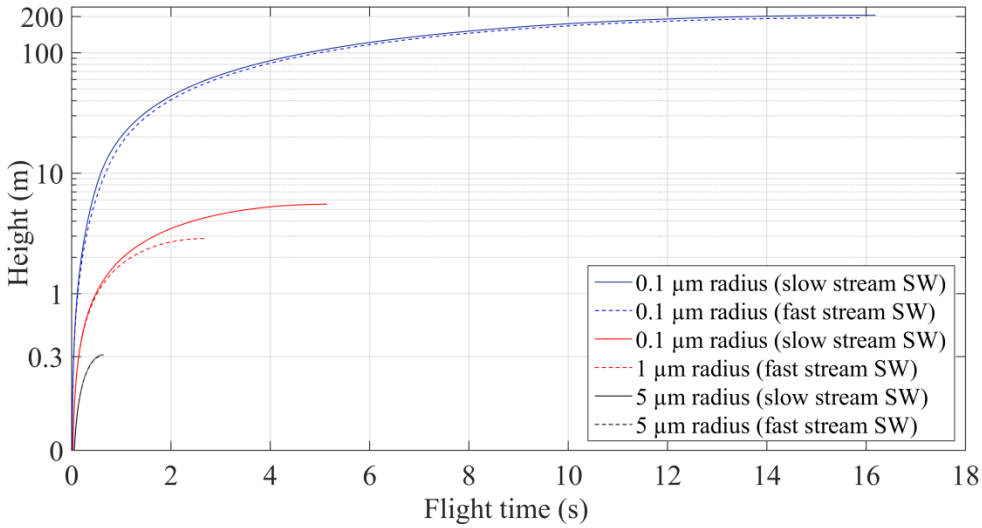

Figure 3.7 : Lofting of the dust grains with 0.1, 1 and 5 μm radius under slow and fast steam SW.

The maximum heights are determined as 204.6 m and 194.7 m for the dust grains with 0.1 μm radius, 5.503 m and 2.860 m for the dust grains with 1 μm radius, and 0.311 m and 0.304 m for the dust grains with 5 μm radius under the slow and fast stream SW conditions respectively (Fig. 3.7). In addition, the dust grains 0.1 μm in radius accelerates within the electron sheath above the terminator region, and they slow down under the gravity influence after leaving the electron sheath (Fig. 3.8). On the other hand, the dust grains with 1 and 5 μm radius decelerate within the electron sheath due to the stronger gravity force than the electrostatic force. Therefore, a thicker electron sheath can accelerate the submicron-sized dust grains for a longer distance.

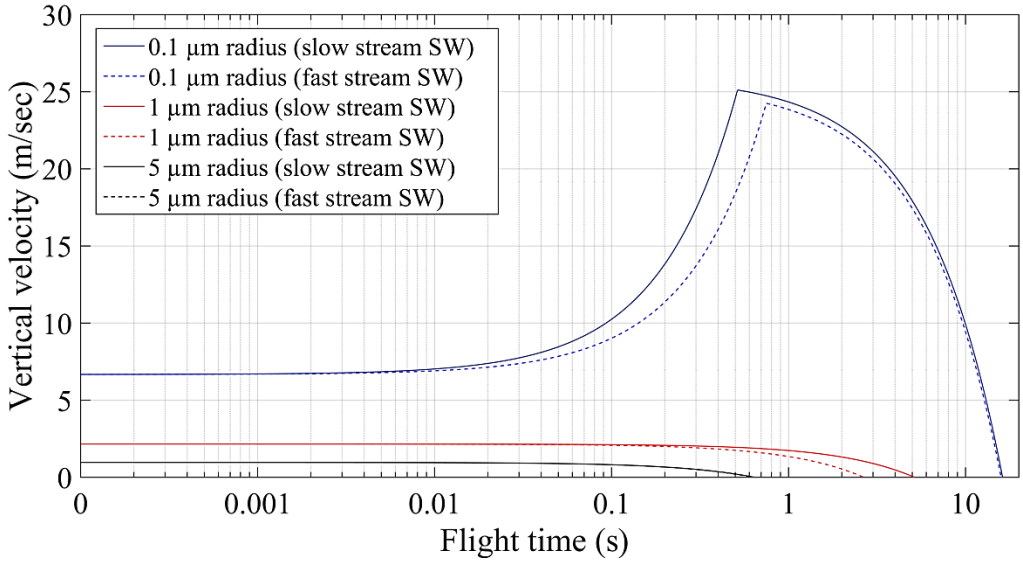

Figure 3.8 : Velocity change of the dust grains with 0.1, 1 and 5 μm radius.

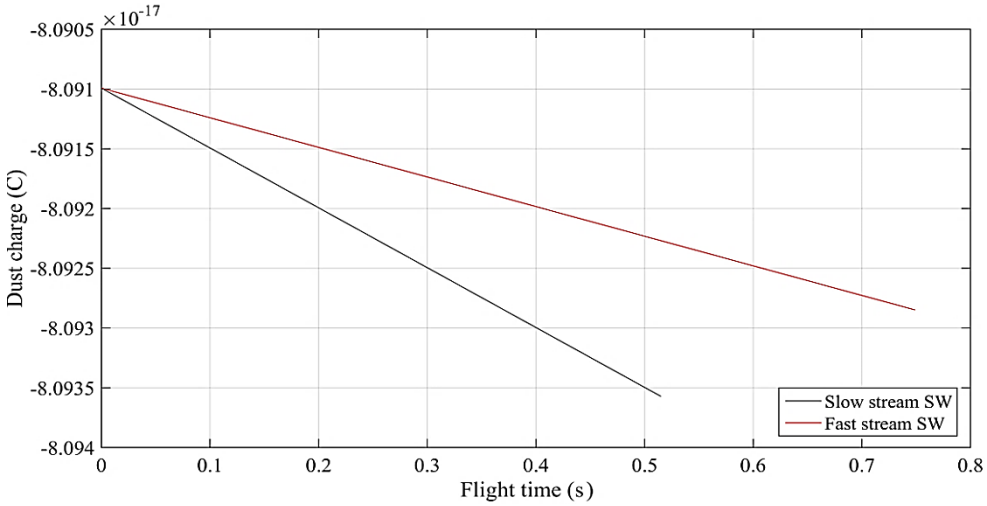

Figure 3.9 : Charge variation of the dust grains with 0.1 µm radius during the lofting motion.

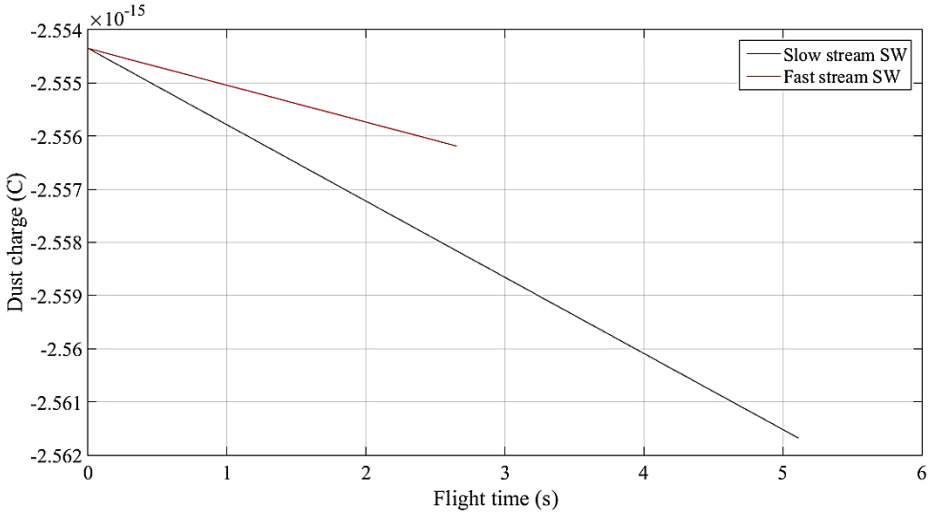

Figure 3.10 : Charge variation of the dust grains with 1 µm radius during the lofting motion.

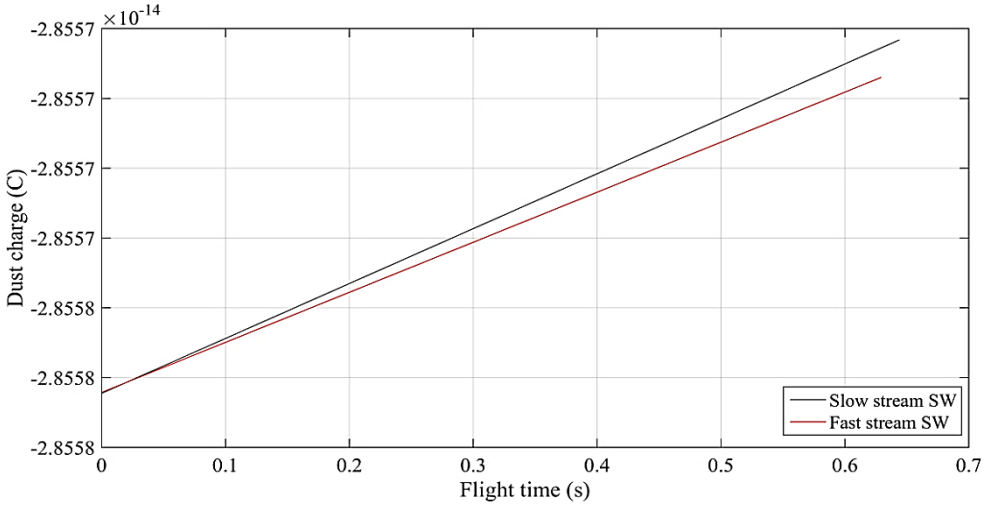

Figure 3.11 : Charge variation of the dust grains with 5 µm radius during the lofting motion.

Fig. 3.9 – 3.11 show the charge variation of the dust grains after the initial launching. Even though the dust grains with 0.1 and 1 μm radius collects electrons within the electron sheath, the dust grains with 5 μm radius loses electrons due to the photoemission. This can be explained by the surface area of the dust grains with 5 μm radius since a larger cross-section facing the solar irradiation allows the dust particle to emit a higher number of photoelectrons.

According to these results, the charging within the microcavities and the surface electric field can produce the lunar horizon glow observations of Surveyor missions under the regular solar wind conditions. In addition, submicron-sized dust grains can reach the altitudes similar to the light scattering observations of Lunokhod-2 astrophotometer. On the other hand, there is a considerable difference between the estimated heights and the high-altitude lunar horizon glow observation during Apollo 15 image sequences.

3.3.2 CME Events

The following results are simulated with the SW parameters during the three CME events that are investigated in section 2. Proton temperature T_i, plasma density n_0 and solar wind velocity V_{sw} are retrieved from NASA/GSFC's OMNI data set through OMNIWeb OMNI (Combined 1AU IP Data; Magnetic and Solar Indices). In addition, the electron temperature T_e is taken from Wind 3-D Plasma Analyzer - R. Lin/S. Bale (UC Berkeley) for all events.

Since the time resolutions of the data sets are different for OMNIWeb and Wind 3-D plasma analyzer, both are re-sampled to 5-minute intervals before the simulations. The time step is chosen greater than the time required to reach the equilibrium potential of the lunar surface and the flight time of the dust grains. First, we have calculated the terminator region surface potential, Debye length, and electric field. Second, the location of the dead zone is estimated since it is controlled by the electron current, and the negatively charged surfaces repulse the charged dust grains while increasing the dust heights. In addition, the secondary electron emission current of each step is compared to the slow stream SW condition since there is no direct measurement near the surface to consider for the dust launching rates related to the ambient plasma parameters.

3.3.2.1 CME Event 01

A geo-effective CME passage is selected from 8 to 13 February 1997 (Bruecker et al., 1998) since its post-shock plasma has higher density than the following CMEs, and it reaches the minimum level compared to the other events during the early CME passage with significantly cold temperatures. There was no solar flare occurrence as mentioned before.

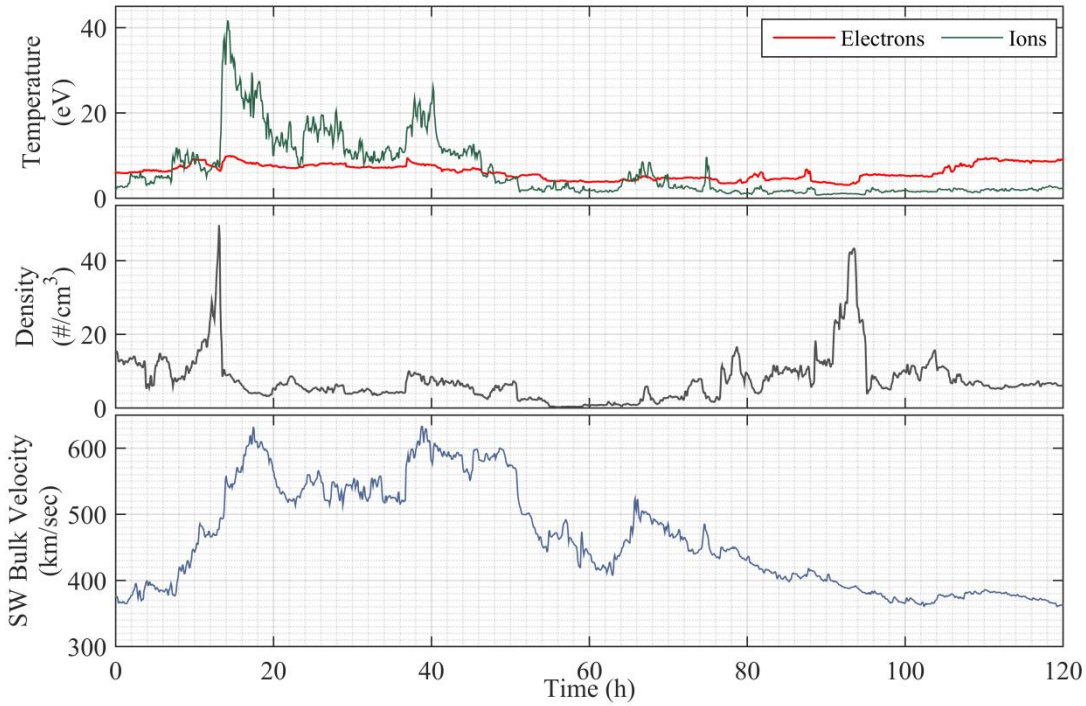

Figure 3.12 : CME event 01 input data.

The electron temperature variation is less than the following events. During the post-shock plasma passage near 13^{th} hour, the ion temperature reaches up to 40 eV, and the density is approximately 45 cm^{-3}. During the early CME passage the minimum plasma density is observed for almost 4 hours, and its effect can be seen in the following results around 56^{th} hour. In addition, the density increased up to 45 cm^{-3} once more while the plasma temperatures are still cold during the CME-driver gas passage. The plasma parameters are given in (Fig. 3.12) as extracted from NASA/GSFC's OMNI data set through OMNIWeb.

During the post-shock plasma passage near 13^{th} hour the terminator region surface potential is approximately -24.52 V, and the electric field becomes -9.036 V/m (Fig. 3.13). In addition, the maximum dust heights above the terminator region become smaller even though the electrostatic forces are stronger due to the electric field. It is

the result of the short time for acceleration within the thinner electron sheath, which is estimated as 2.890 m. The minimum plasma density is observed during the early CME passage near 56^{th} hour, and the surface potential is found as -16.31 V while the electric field is -0.556 V/m. Since the electrostatic forces become significantly weak on the terminator region, the dust heights become lower.

During the late CME passage between 76^{th} and 110^{th} hours the terminator region has ranging values from -34.80 V to -13.27 V. In addition, the electric field ranges from -7.463 V/m to -1.540 V/m. Dust heights show that dust grains with 0.1 μm radius can reach up to approximately between 67.39 m and 148.9 m above the terminator region.

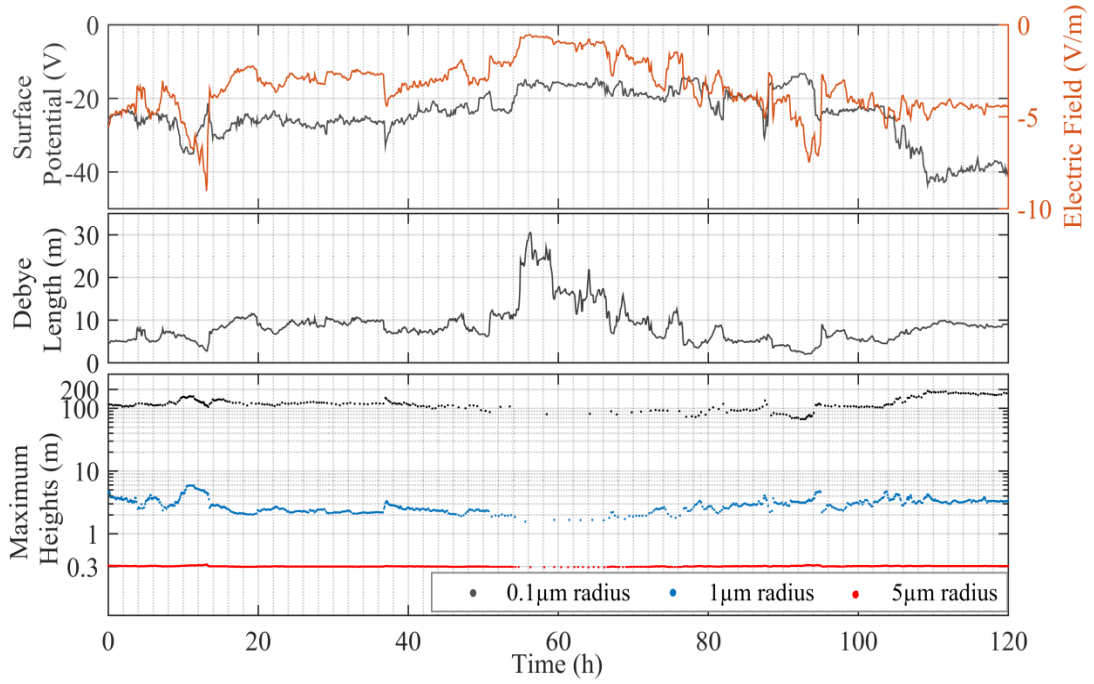

Figure 3.13 : The results for surface potential and electric field (top), debye length (middle) and maximum heights (bottom) for terminator region.

The dead zone location varies between 56^{o} and 90^{o} during the CME passage (Fig. 3.14). First, the high-density post-shock plasma moves the dead zone location closer to the subsolar point; therefore, it is found as 56.52^{o} near 13^{th} hour. Second, the minimum density during the early CME passage allows the dead zone location to move closer to the terminator region due to the dominance of the photoelectron emission, and it carries its location up to 89.84^{o}. Furthermore, its location varies between 67.24^{o} and 86.97^{o} due to the density variation during the late CME passage. After 110^{th} hour the plasma density and the electron temperature return to

the levels seen in the regular SW. Higher electron temperature leads to stronger negative surface potentials on the terminator region, and the average plasma density allows the dust particles to reach higher altitudes even though the terminator region electric field has average values.

According to the secondary electron emission ratios, the number of the particles launched from the surface can increase around 13^{th} and 90^{th} hours compared to the slow stream SW conditions since the secondary electron emission controls the separation of charged dust grains. In addition, the dust grains are launched more frequently during the post-shock plasma passage and the density enhancement of the CME-driver gas. On the other hand, dust lofting is not observed to the high altitudes during the early-CME passages near 60^{th} hour.

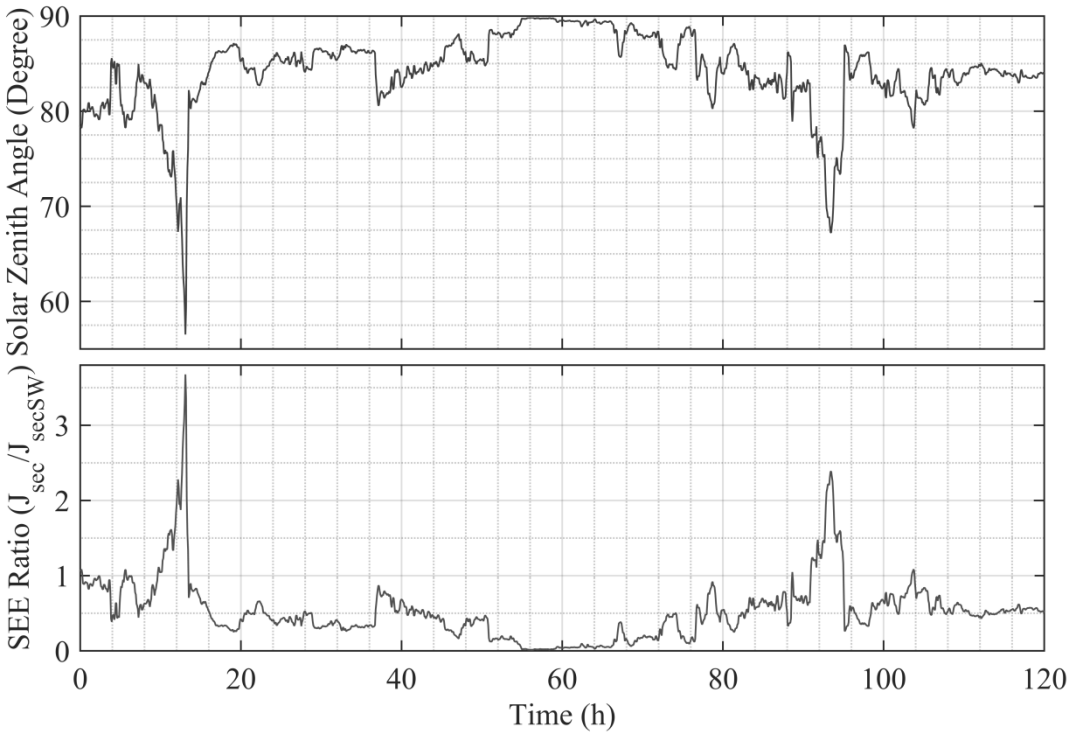

Figure 3.14 : Dead zone location (top) and secondary electron emission ratio between each iteration and slow stream solar wind (bottom).

3.3.2.2 CME Event 02

Another geo-effective CME event had occurred from 1 to 3 May 1998 (Farrell et al., 2012, 2013). The plasma temperature starts as the regular solar wind conditions, and it reaches approximately 46.07 eV for the ions during post-shock plasma passage while the solar wind velocity increases up to 620.8 km/s. Electron temperatures are generally colder than the ions'. In addition, the plasma density, the temperature and

the SW bulk velocity become significantly high around 25^{th} hour; therefore, we can observe the charging of the lunar surface under highly dense and fast flowing plasma.

Following the post-shock plasma, the density and temperature become similar to the regular SW conditions during the early CME passage. On the other hand, the CME-driver gas reaches the Moon with a density of approximately 10 times that of the previous plasma population after 55^{th} hour. Therefore, very cold and highly dense plasma is observed during the late CME period before the plasma properties return to the regular solar wind conditions. In addition, a solar flare event had occurred during the early CME period on 2 May 1998, and the photoemission current density is increased by a factor of 5 for an X1-type solar flare (Farrell et al., 2013). The plasma parameters are given in Fig. 3.15 as extracted from NASA/GSFC's OMNI data set through OMNIWeb.

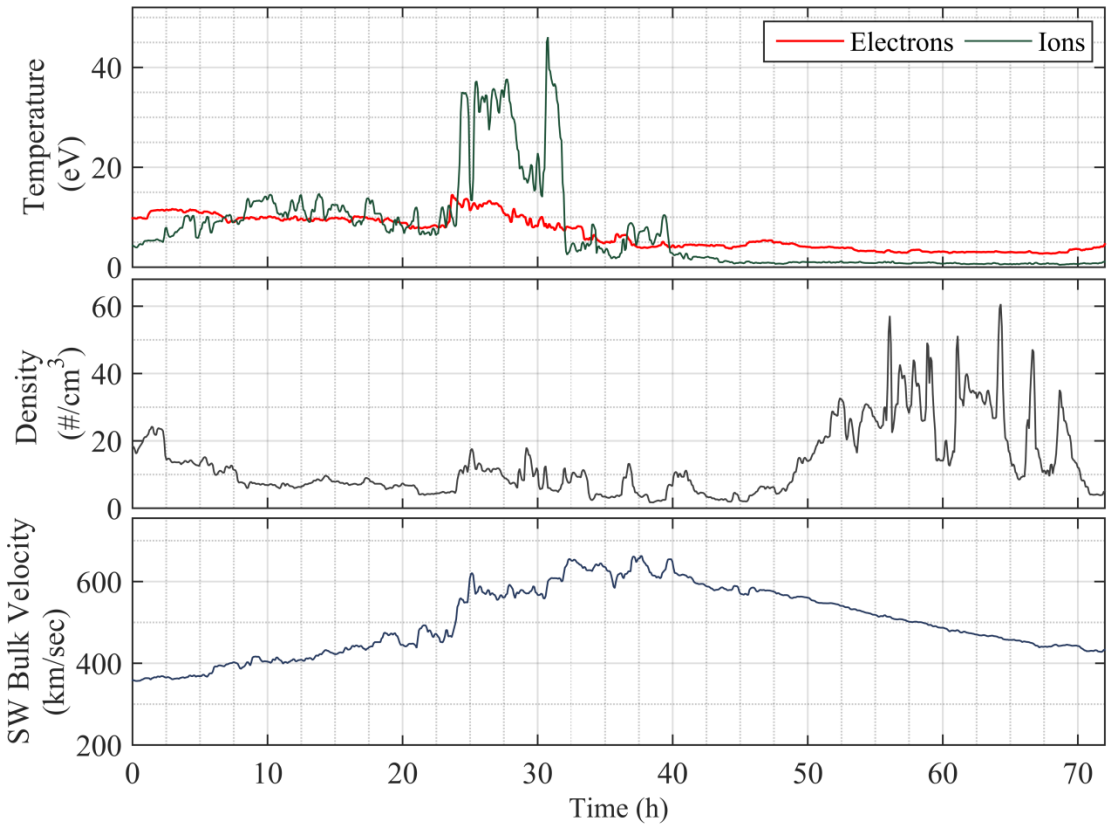

Figure 3.15 : CME event 02 input data.

During the post-shock plasma passage near 24^{th} hour, the terminator region is charged to higher negative potentials up to -57.04 V, and the electric field becomes stronger as -4.505 V/m even though the electron temperature increases less than the

ions'. The maximum dust heights above the terminator region become higher due to the increase of the electron sheath thickness and electron temperature. Therefore, the dust grains with 0.1 μm radius can reach up to 242.5 m, whereas the heights of the particles with 5 μm radius are found as 30.65 cm. During the late CME passage after 55^{th} hour, the average surface potential is approximately -14 V while the electric field ranges from -8.379 V/m to -3.069 V/m. Dust heights show that 0.1 μm size dust grains can reach up to approximately 68.74 m above the terminator region, whereas the heights are found as approximately 3.421 m for 1 μm grains and 32.13 cm for 5 μm grains (Fig. 3.16).

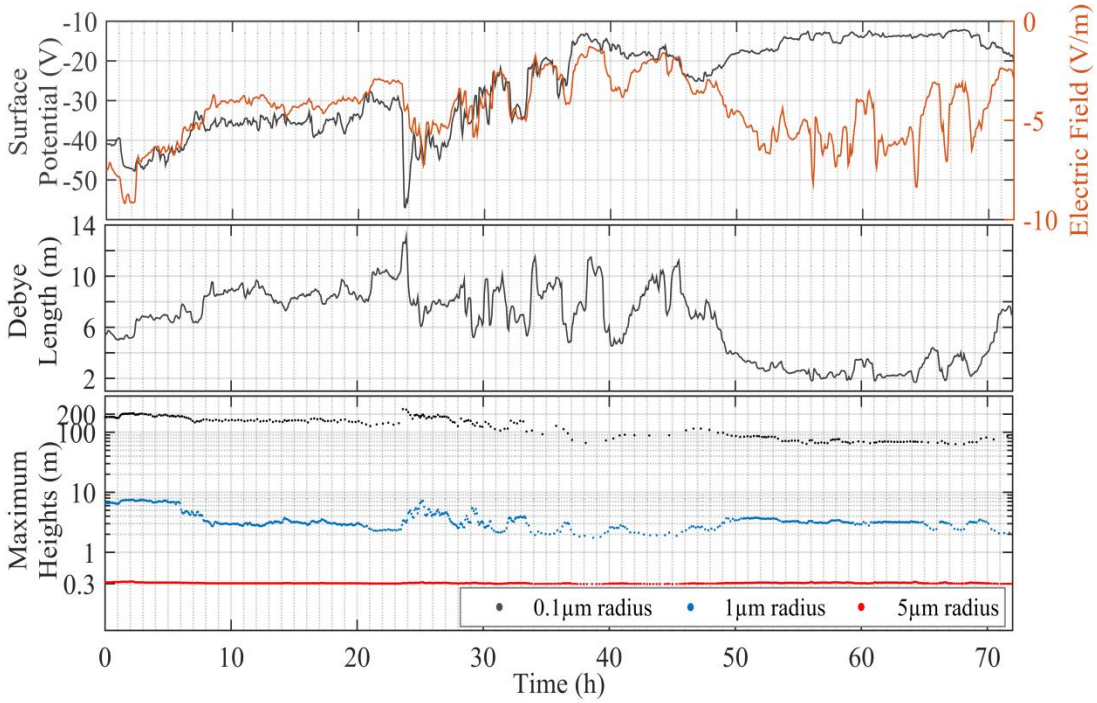

Figure 3.16 : The results for surface potential and electric field (top), debye length (middle) and maximum heights (bottom) for terminator region.

The dead zone location varies between 65^{o} and 90^{o} during the CME passage (Fig. 3.17). First, the post-shock plasma conditions increase the electron current to the surface, which tends to move the dead zone location closer to the subsolar point. Second, the solar flare event produces higher photoelectron emission, and it moves the dead zone location up to 89.49^{o}. Finally, its location varies between 64.51^{o} and 85.31^{o} due to the density variation during the late CME passage.

The secondary electron emission ratio is not considerably high during the post-shock plasma passage around 24^{th} hour (Fig. 3.17). Even though it suggests increasing of the maximum heights, the number of the particles launched from the surface can be

lower than the first event. Finally, the charging times of the dust particles increase after 30^{th} hour due to the colder electron temperatures and lower density until the late CME passage.

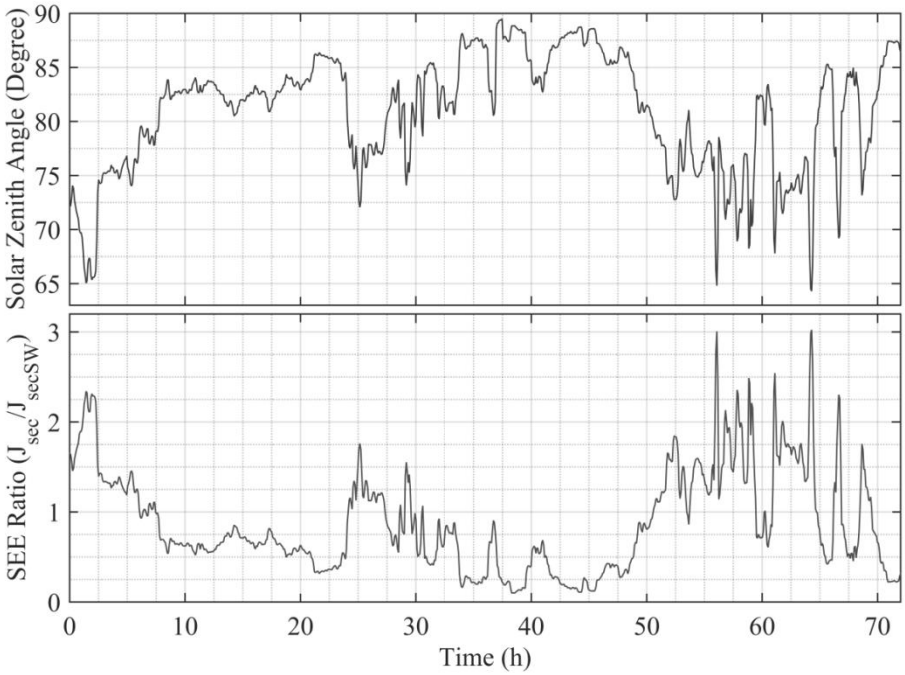

Figure 3.17 : Dead zone location (top) and secondary electron emission ratio between each iteration and slow stream solar wind (bottom).

3.3.2.3 CME Event 03

The final geo-effective CME event is selected from 8 to 12 March 2012 (Möstl et al., 2014) since its post-shock plasma has higher electron temperature than the previous cases and lower plasma density than the first event. Therefore, it is expected to observe the influence of the high electron temperature without the negative impact of thin electron sheath on the dust heights. In addition, there were two X1 type solar flare occurrences on 9^{th} and 10^{th} of March. The following plasma parameters are given in Fig. 3.18 as extracted from NASA/GSFC's OMNI data set through OMNIWeb.

During the post-shock plasma passage after 10^{th} hour, the electron temperature reached up to 32.15 eV, whereas the ion temperature is approximately 82.65 eV while the density is 25 cm^{-3}. In addition, the upstream ions remain with high thermal energies longer than electrons while the electrons start to get colder around 12^{th} hour while the density decreases. The surface potential is approximately -131.3 V, and the electric field becomes -12.75 V/m. In addition, the maximum heights for

the dust grains with 0.1 μm radius above the terminator region reach up to 541.6 m, which is the maximum value in all three events, and it remains in those altitudes less than an hour (Fig. 3.19).

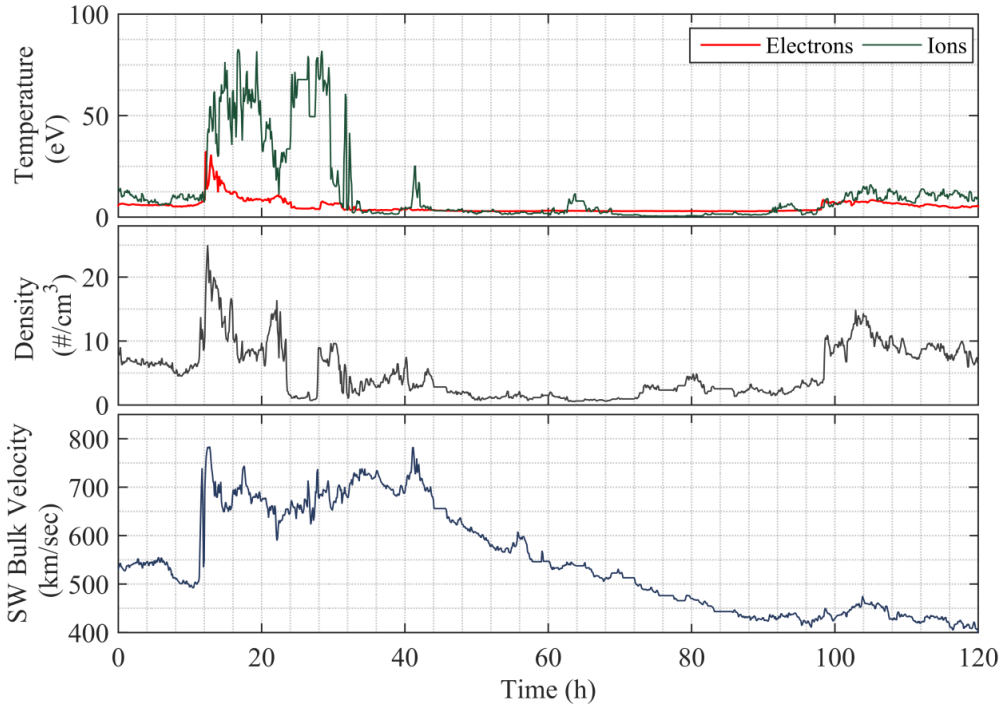

Figure 3.18 : CME event 03 input data.

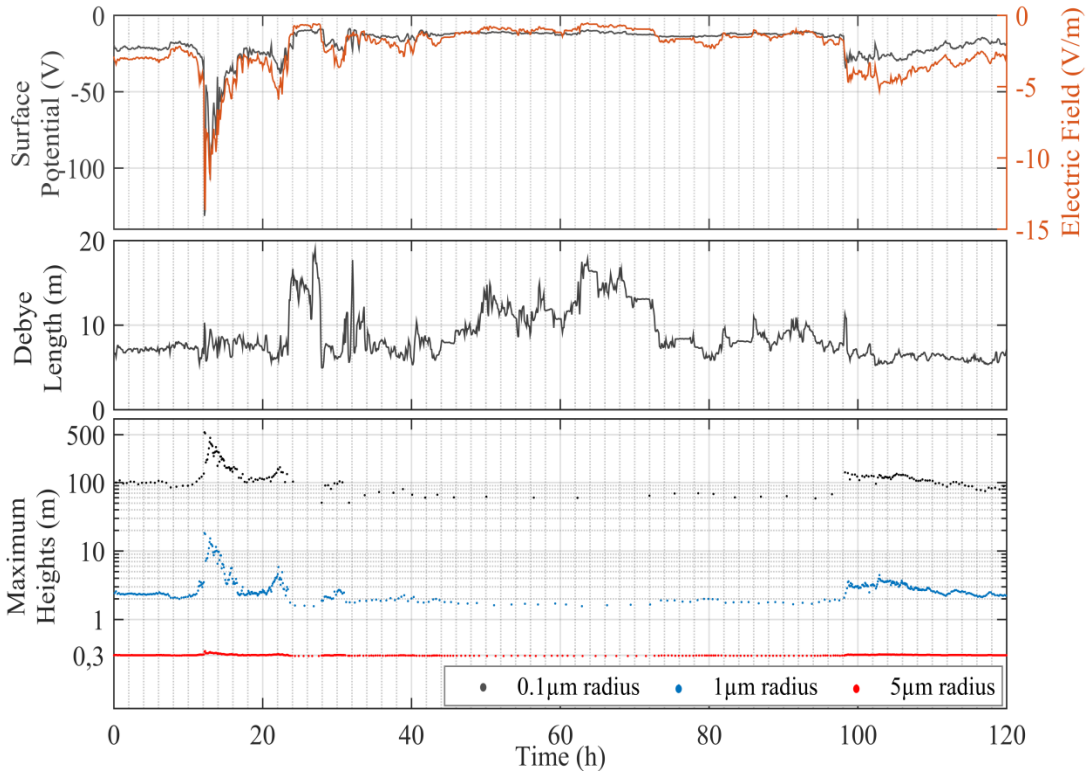

Figure 3.19 : The results for surface potential and electric field (top), debye length (middle) and maximum heights (bottom) for terminator region.

The plasma density becomes as low as 0.535 cm^{-3} during the early CME passage. In addition, the electron temperature becomes near 2.894 eV, and the ion temperature decreases down to 0.441 eV. The surface potential varies between -17.45 V and -9.777 V and the electric field remains around -1 V/m. Since the electrostatic forces become extremely weak, the dust grains cannot reach high altitudes. In addition, the secondary electron emission decreases significantly, and the charging time of the all particle sizes are increased considerably for approximately 3 days around the terminator region, and it takes hours for the submicron-sized grains to collect the required charges.

The terminator region has ranging values from -34.71 V to -14.74 V during the late CME passage after 98^{th} hour. In addition, the surface electric field ranges from -5.306 V/m to -2.516 V/m. Dust heights show that 0.1 μm size dust grains can reach up to approximately 153.3 m above the terminator region whereas 1 μm size dust grains can reach up to approximately 4.432 m, and 5 μm size dust grains have 30.95 cm heights.

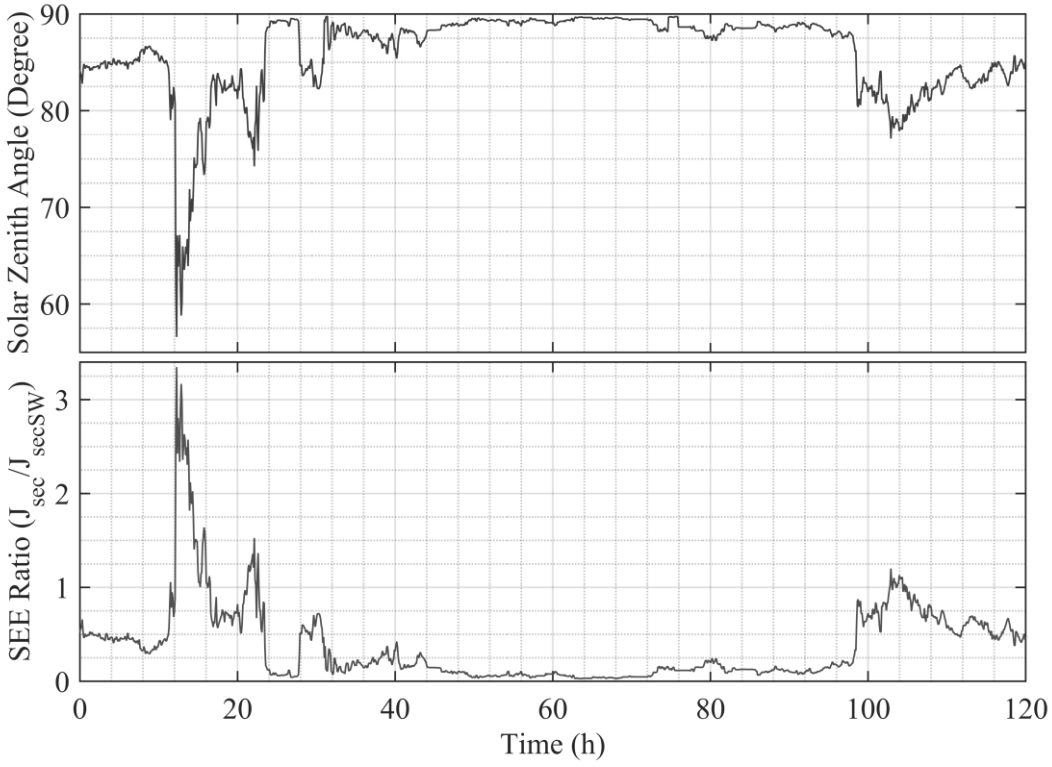

Figure 3.20 : Dead zone location (top) and secondary electron emission ratio between each iteration and slow stream solar wind (bottom).

The dead zone location varies between 56^{o} and 90^{o} during this event (Fig. 3.20). First, the high-density post-shock plasma near 12^{th} hour moves the dead zone

location closer to 56.52^{o}. Second, the minimum density during the early CME passage and the solar flares carry the dead zone location up to 89.76^{o}. Furthermore, its location varies between 77.12^{o} and 86.25^{o} due to the density variation during the late CME passage after 98^{th} hour.

The secondary electron emission ratio suggests the number of the launched dust particles may increase during the post-shock plasma passages before becoming substantially low due to cold electrons with low density.

3.3.3 Error Sources

3.3.3.1 Uncertainty of Maximum Height Estimations

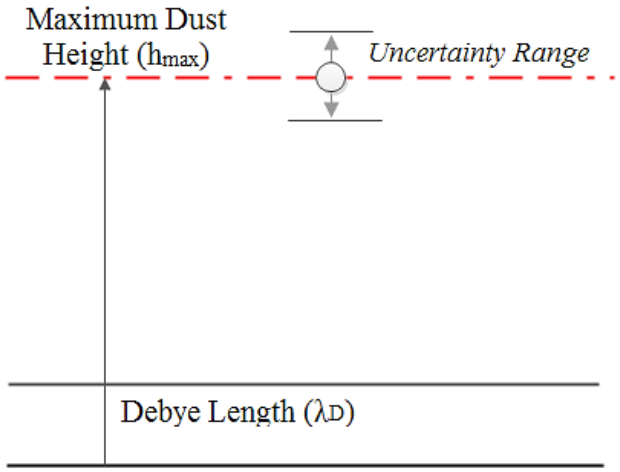

Figure 3.21 : Uncertainty range during the maximum height calculations.

An error source is present in the simulations due to the selection of the time step since the height of the dust particles are tracked together with their velocity (Fig. 3.21). Since the particles are slowing down under the gravity of the Moon, the velocity can change direction during the final iteration of the simulation.

By using the energy formulas, the following uncertainty range can be calculated for the dust grains slowing down under the influence of the lunar gravity as (Fig. 3.22 and 3.23):

$$dh = \frac{V(t)^2 - V(t-1)^2}{2g_{lunar}} \tag{3.21}$$

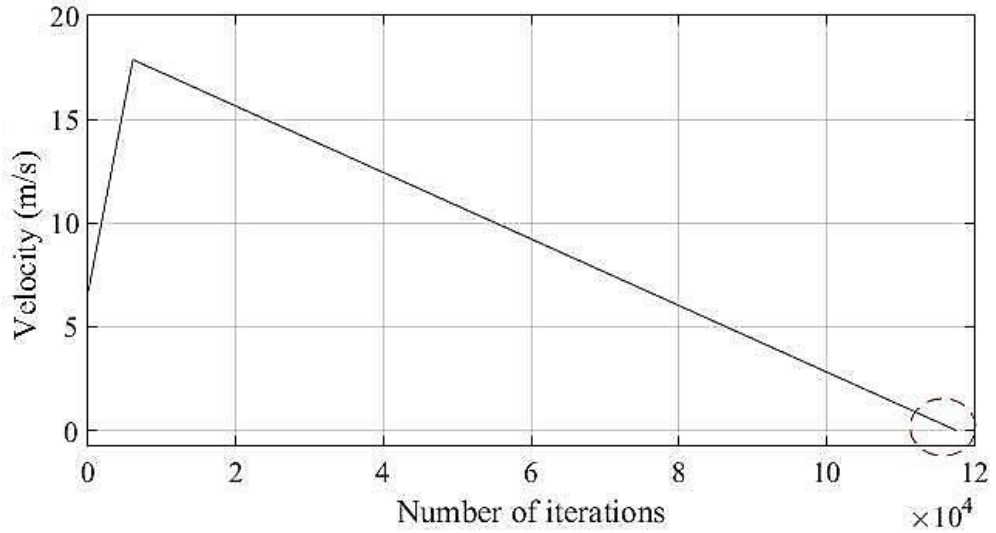

Figure 3.22 : Initial electrostatic acceleration of the dust grains with 0.1 μm radius and its deceleration under the lunar gravity after passing through the Debye length. (electrostatic acceleration > lunar gravity).

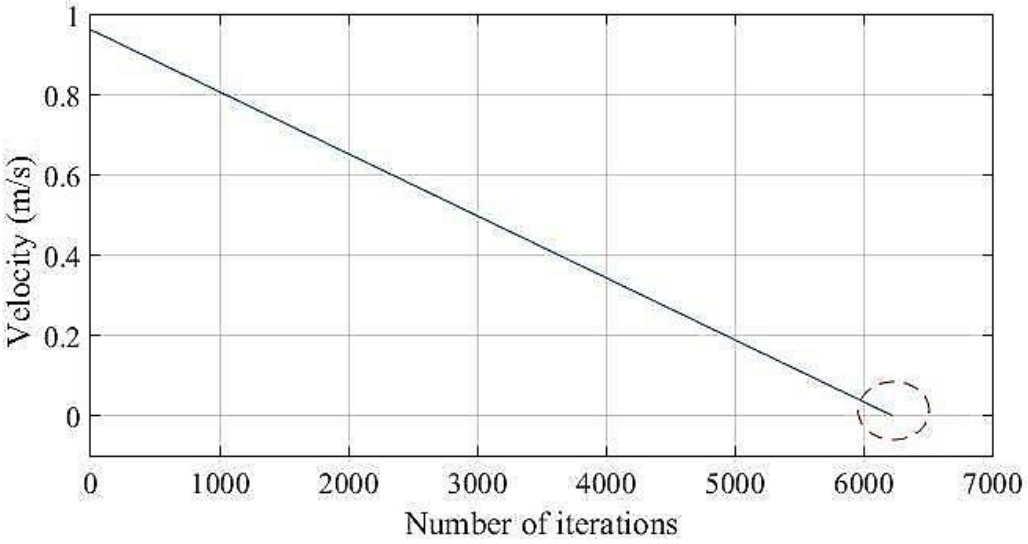

Figure 3.23 : Velocity of the dust grains with 5 μm radius and its deceleration under the lunar gravity within the Debye length. (electrostatic acceleration < lunar gravity).

Since the velocity and height of the dust grains are updated with $\delta t = 10^{-4}\ s$, the potential error is calculated in the range of $10^{-11} - 10^{-9} m$ for the reported heights (Fig. 3.24 and 3.25). This error increases when the time step is selected longer than $\delta t = 10^{-4}\ s$. For instance, the potential error range is found around $10^{-5} m$ when the time step is selected as $\delta t = 10^{-2}\ s$. For this reason, all calculations for the dust motion are performed with $\delta t = 10^{-4}\ s$.

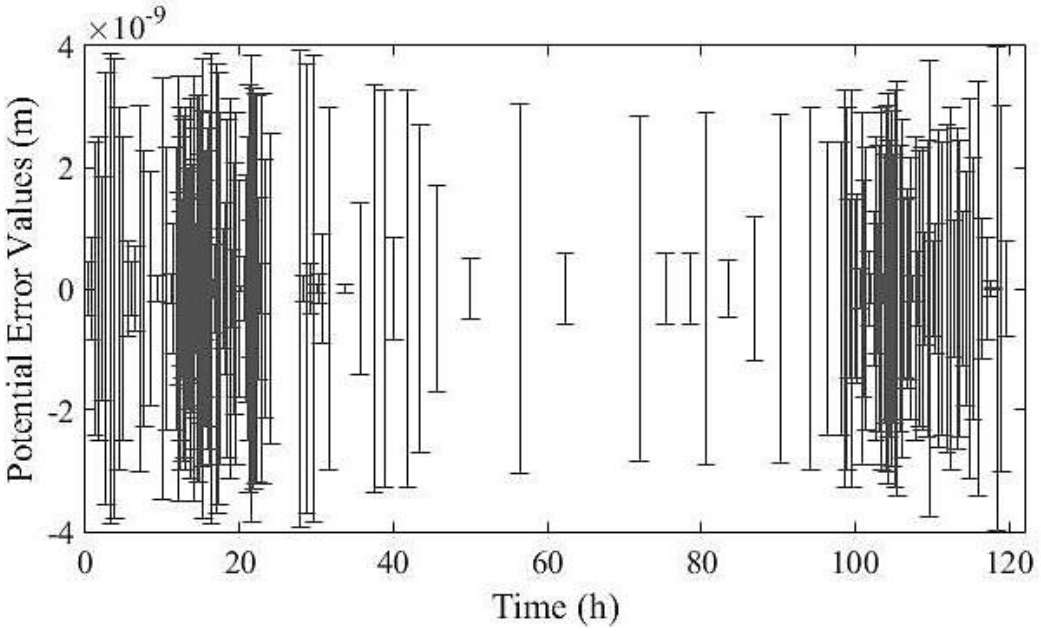

Figure 3.24 : Potential error values for the maximum height calculations of the dust grains with 0.1 μm radius during the CME event 03.

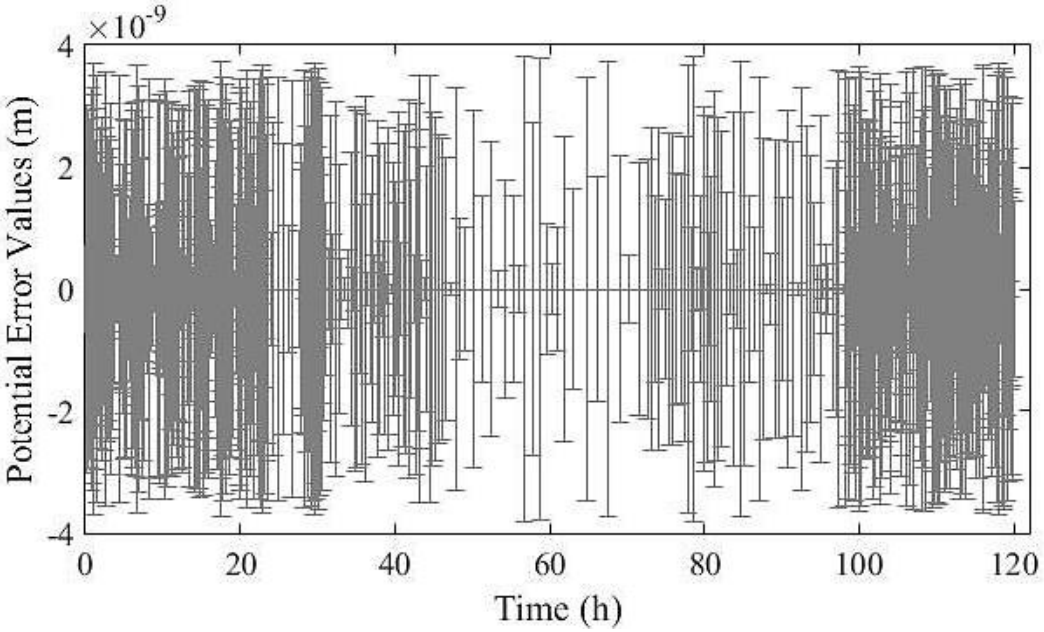

Figure 3.25 : Potential error values for the maximum height calculations of the dust grains with 5 μm radius during the CME event 03.

3.3.3.2 Velocity Error during Electron Sheath Boundary Passage

The dust particles are repelled from the lunar surface due to the electrostatic forces within the surface electron sheath. If they can leave this sheath thickness, they slow down under the lunar gravity and eventually return to the surface. However, the potential error within the passage of the electron sheath boundary can cause the error accumulation for the following time steps.

$$V(t) = V(t-1) + a_{dust}(t-1)\delta t \tag{3.22}$$

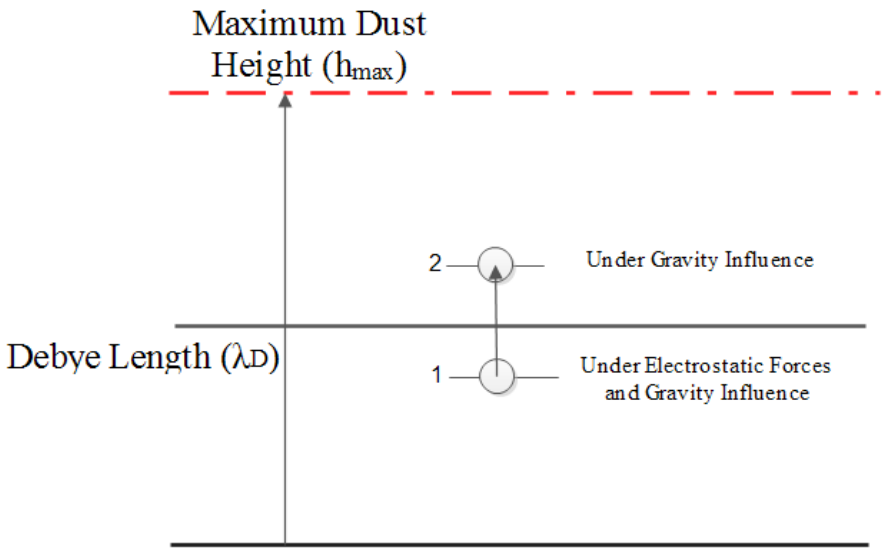

Figure 3.26 : Potential error source due the acceleration update during the passage of surface electron sheath.

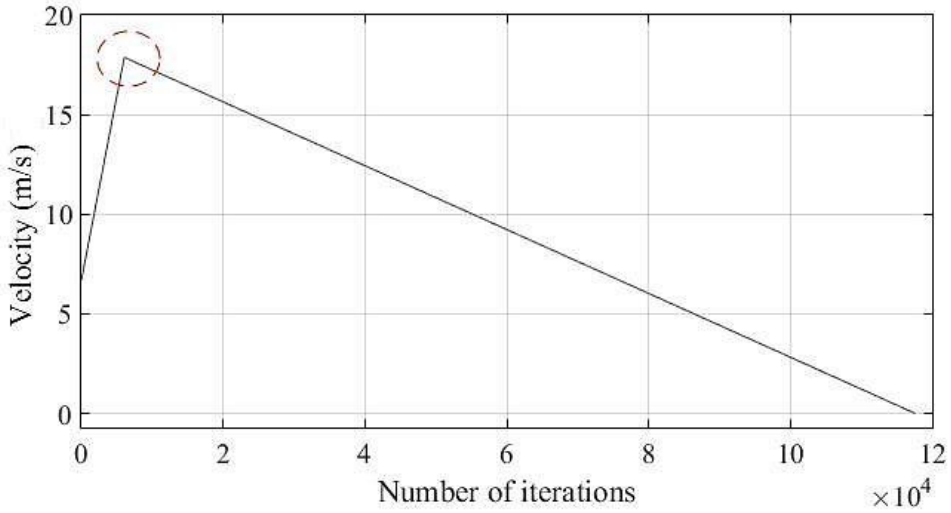

Figure 3.27 : Potential error source due the acceleration update during the passage of surface electron sheath.

The time step ($\delta t = 10^{-4}$ s) can be divided into two parts such as the required time to reach from the current position to the boundary of the electron sheath δt_1 and the remaining time to reach the next position after passing the electron sheath δt_2. Therefore, $\delta t = \delta t_1 + \delta t_2$. As a result, when the simulation updates the velocity and height profile with the electrostatic acceleration from position 1 to 2 in Fig. 3.26, it represents a potential error related to the selected time step and the velocity of the particle. The velocity can be estimated as:

$$V' = V(t-1) + \left(a_q(t-1) - g_{lunar}\right)\delta t_1 - g_{lunar}\delta t_2 \quad (3.23)$$

a_q is the electrostatic acceleration, and g_{lunar} is the lunar gravity. The potential error between the estimated $V(t)$ and V' can be calculated as:

$$\varepsilon_{velocity} = V(t) - V' = -a_{dust}(t-1)\delta t_2 \quad (3.24)$$

Since we track the height of the dust grains, the difference between the position 1 and the electron sheath boundary can be calculated (δh).

$$\delta h = V(t-1)\delta t_1 + 0.5\left(a_q(t-1) - g_{lunar}\right)\delta t_1 \quad (3.25)$$

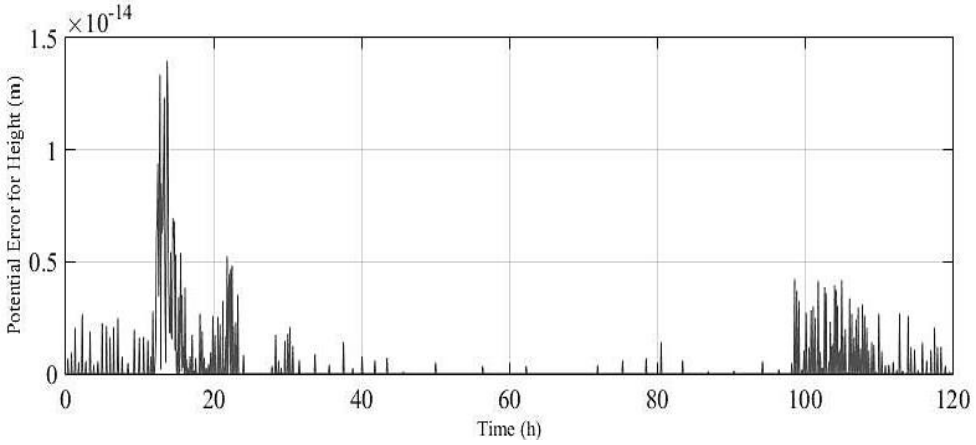

Figure 3.28 : Uncertainty value due the acceleration update during the passage of surface electron sheath of CME event 03 for dust grains with 0.1 μm radius.

δt_1 can be calculated from the equation above since all other elements are known within the simulation. As a result, the remaining time can be calculated as $\delta t_2 = \delta t - \delta t_1$. The error in the maximum height calculations due to the velocity error could be estimated as:

$$\varepsilon_{height\_max} = \varepsilon_{velocity} \sum dt \quad (3.26)$$

The uncertainty ranges are calculated as approximately 10^{-21} – 10^{-20} m/s for the velocities and 10^{-16} - 10^{-14} m for the heights ε_{height_max} for δt= 10^{-4} s.

3.3.3.3 Total Estimated Errors for the Predicted Heights

According to the error analysis, it is observed that the accuracy of the results is sufficient for the simulations. All initial constants are included into the simulation

code with 9 significant figures. In addition, Matlab uses 16 digits for precision. The potential error estimations increase with the simulation time steps while updating the velocity and height of the dust grains.

The following results are given for the investigated dust particles during the third CME event from 2012.

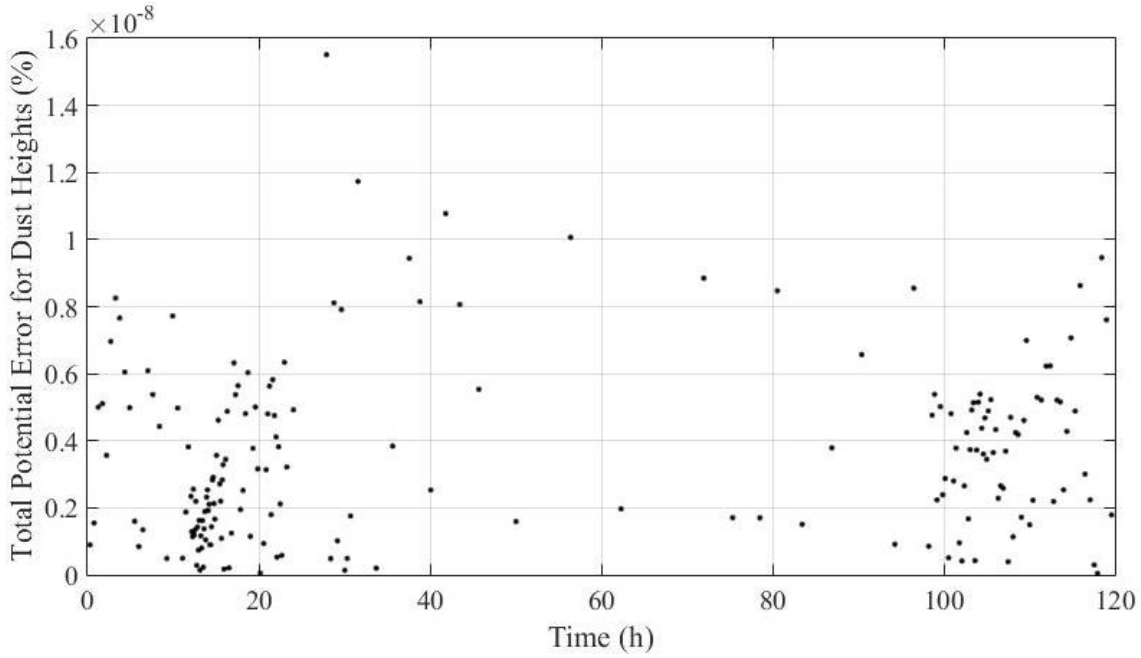

Figure 3.29 : Total potential error percentage estimation of the heights for the dust grains with 0.1 μm radius during the third CME event for $\delta t = 10^{-4}$ s.

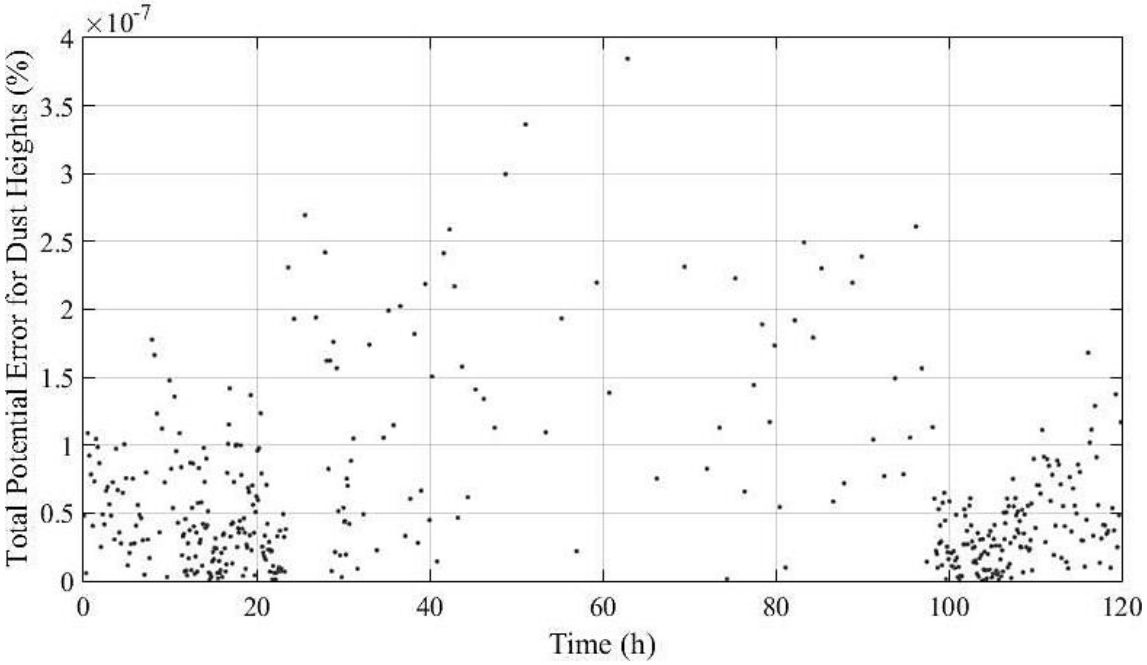

Figure 3.30 : Total potential error percentage estimation of the heights for the dust grains with 1 μm radius during the third CME event for $\delta t = 10^{-4}$ s.

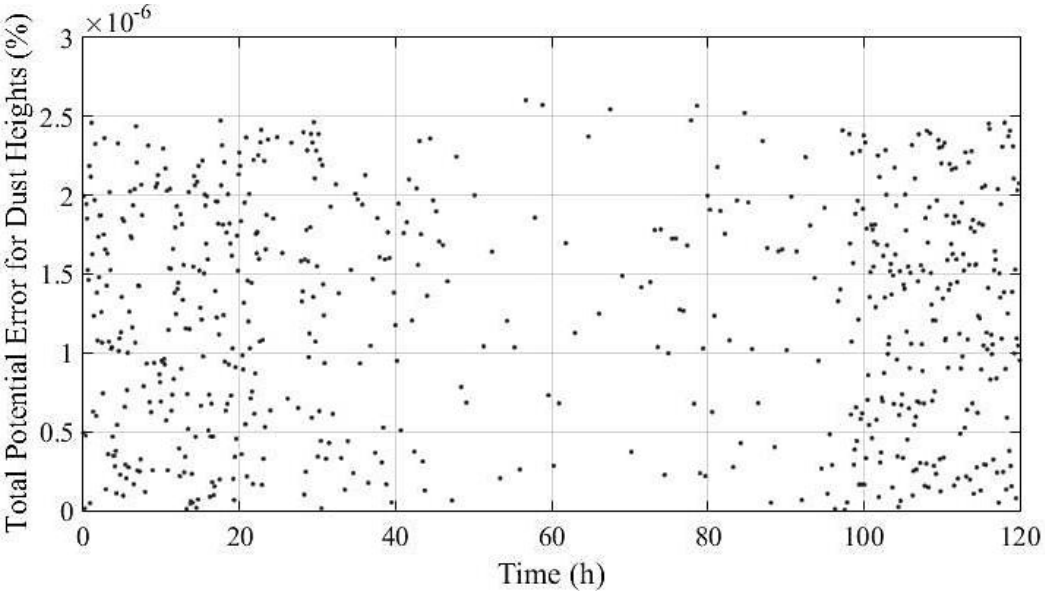

Figure 3.31 : Total potential error percentage estimation of the heights for the dust grains with 5 μm radius during the third CME event for $\delta t = 10^{-4}$ s.

4. EXPERIMENTAL INVESTIGATION ON SILICA DUST LOFTING

4.1 Introduction

Recent laboratory experiments demonstrated that dust particles can be lofted in the vacuum chamber under the electron beam and/or UV lamp (Wang et. al, 2016; Champlain et al., 2016; Schawn et al., 2017) since the emitted electrons are absorbed by the neighboring dust grains while producing strong repulsive forces between the charged particles. Since the size of the microcavities is significantly small, the repulsive force between the dust grains can overcome the forces of gravity and contact.

Hartzell et al. (2011, 2013) indicated the importance of the contact forces for the dust grains with smaller sizes; consequently, they concluded that the required surface electric field strength to detach a dust grain is minimum for intermediate-sized particles since the contact force is dominant for smaller sized grains, whereas the gravity force is effective for larger sizes. On the other hand, this study does not include the emitted electron absorption between the neighboring dust grains. Therefore, it represents a challenge to detach small-sized particles from a surface without the electrostatic forces since these grains are under the influence of the cohesion more than the gravity (Hartzell et al., 2017). In addition, it is seen that the particles can be launched by mechanical vibrations while the electric field near the boundaries between sunlit and dark surfaces can also contribute to the dust transportation (Criswell, 1973; Champlain et al., 2016; Poppe et al., 2012; Hess et al., 2015).

The initial charging of the regolith grains is critical in order to predict the dust transportation since the particle velocities and the forces resulting from the surface electric field are determined accordingly.

The purpose of the experiments is to investigate our capability to predict electrostatic dust transportation in the vacuum chamber experiments in order to estimate the lunar dust heights for a future CubeSat mission to observe the LHG. In this chapter, the

initial vertical launching velocity and the maximum heights of the spherical silica dust grains are calculated while including the estimated repulsive Coulomb forces between the charged particles in order to compare with the experimental results. The experiment setup is explained in Section 4.2, and the estimation of velocities and heights are described in Section 4.3. In addition, the experimental results are given in Section 4.4.

4.2 Experiment Setup and Method

The experiments are performed under 4×10^{-3} Pa pressure in a general-purpose vacuum chamber that is 45 cm in diameter and 50 cm in height. In addition, an electron beam is produced from a cathode ray tube, and the electron current density is measured as approximately 2.87 x 10^{-4} Am^{-2} by a Faraday cup and a digital multi-meter (Fig. 4.1).

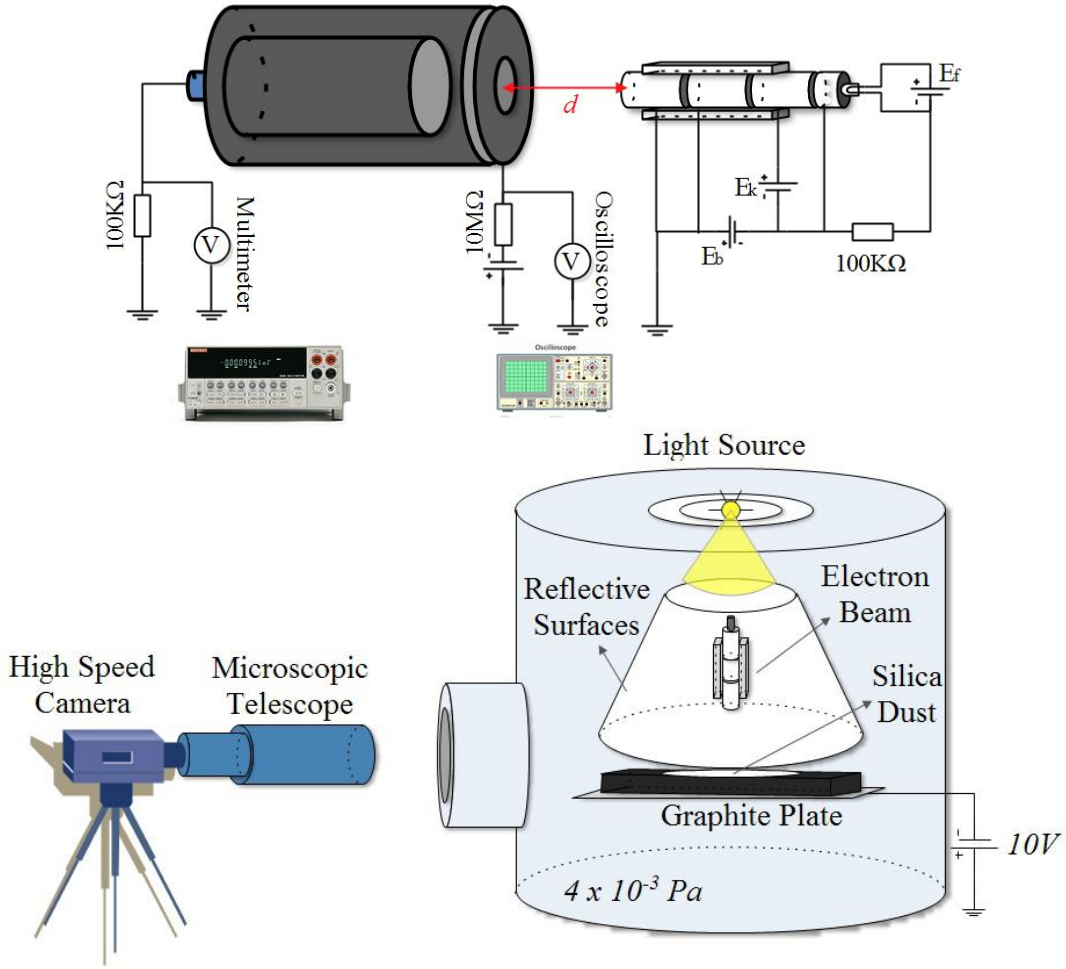

Figure 4.1 : The electron beam and the Faraday cup (top), and the general experimental setup (bottom).

Different from the previous dust lofting experiments (Wang et al., 2009; Hartzell et al., 2013; Wang et. al, 2016; Champlain et al., 2016; Schawn et al., 2017), the initial launching velocities of the grains are detected by the microscopic telescope (Questar QM-1) and the high-speed camera (Photron SA3) by focusing on the near-surface area above the dust sample (Fig. 4.2), and these measurements are compared with the estimated values. Therefore, the maximum height measurements are limited by the field of view. In addition, the influence of the packing density on the dust lofting is investigated since it is expected to increase the contact surface areas between the dust grains while decreasing the number of the microcavities.

Figure 4.2 : The microscopic telescope and the high-speed camera.

The graphite plate is placed on an aluminum that is connected to a power source in order to be biased to -10 V to control the electric field between the electron beam and the plate (Fig. 4.3), and the graphite plate is grounded at the end of each experiment.

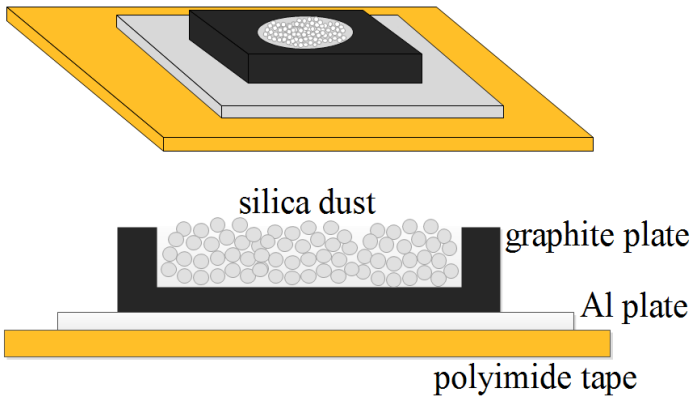

Figure 4.3 : Silica dust sample placed on the graphite plate, the biased Al plate and the polyimide tape.

Moreover, the reflective surfaces are positioned near the chamber walls after increasing the camera speed up to 500 fps to enhance the brightness of the dust grains (Fig. 4.4), and high-intensity light sources within our laboratory are not preferred since they generate photoelectrons from the dust grains and generate additional charging.

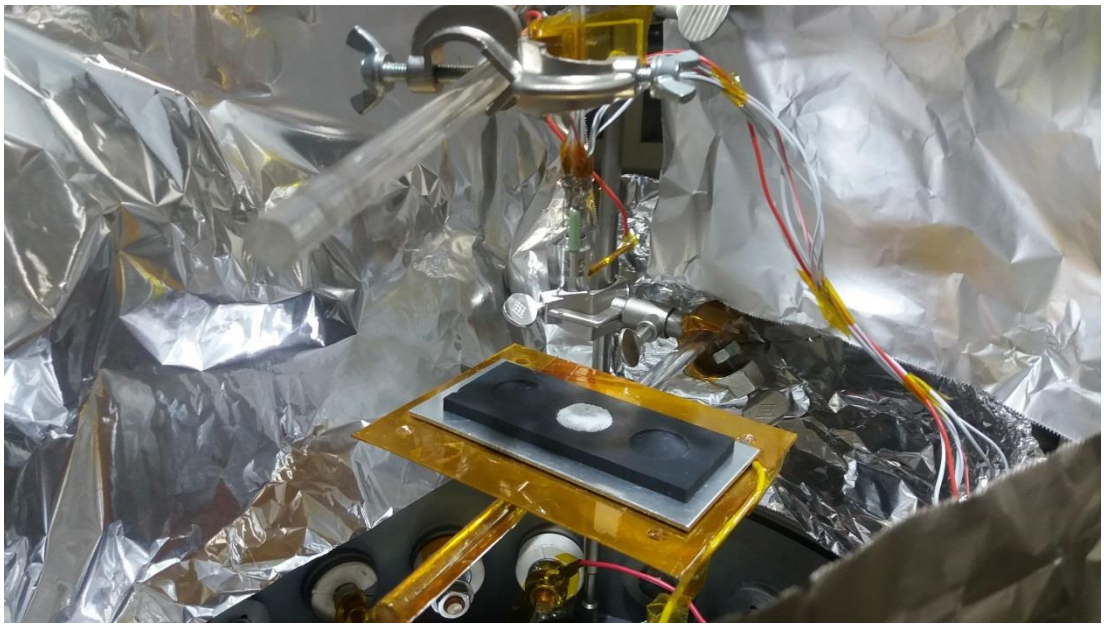

Figure 4.4 : Silica dust grains on the graphite plate inside the vacuum chamber.

Depending on the distance between the microscopic telescope and the dust sample, the resolution can be determined between 2.4 - 19.0 μm/pixel, and the maximum possible errors are +/-23 μm for the heights and +/-5.75×10^{-3} m/s for the velocity measurements with 250 fps speed due to the accuracy of the microscope scale and the pixel resolution. In addition, a video processing code is developed in order to remove the noise from the pixel values and detect the mobilized particle trajectories in Matlab (Fig. 4.5).

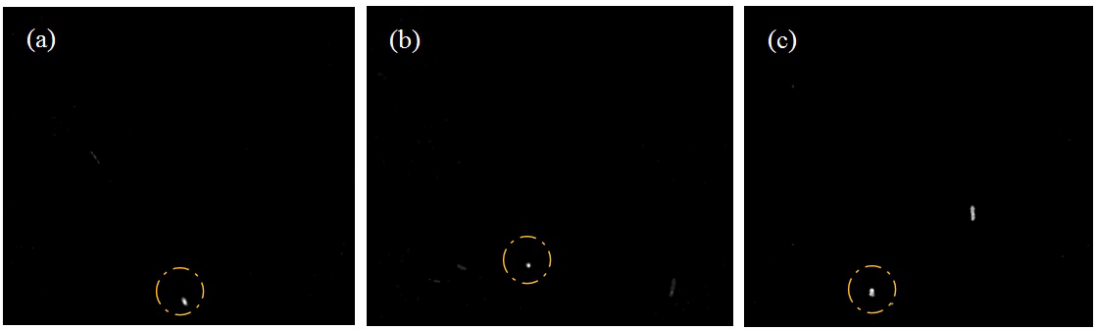

Figure 4.5 : Silica dust lofting trajectory under the electron beam: (a) initial launching (b) reaching.

Silica dust samples are prepared in the same manner for all experiments and investigated under another microscope to acquire particles with 45 μm and smaller sizes in radius since it is possible to observe aggregates up to approximately 170 μm in the glass containers due to the contact forces (Fig. 4.6). Therefore, the upper limit is approximately 45 μm by the crushing process, and we are able to identify single spherical particles smaller than 6 μm in radius under the microscope.

Figure 4.6 : Silica dust grains.

There are three different experiments that are performed. First, the dust grains are loaded on the graphite plate without applying additional pressure or external horizontal electric field. Therefore, it is called the simple case, and the estimation of the maximum heights are made for the dust particles charged within a single microcavity with a microcavity size as the particle diameter. Second, two different dust samples are compressed after loading on to the graphite plate with approximately 780.7 and 3780 Pa in order to increase the contact surface areas among the dust grains while decreasing the number of the microcavities. Therefore, it is expected to observe a smaller number of lofting events in these experiments. In addition, the initial vertical launching velocities increase due to higher potential energy built-up until the electrostatic repulsion can overcome the stronger attachment between the dust grains. Finally, the graphite plate is placed between two parallel aluminum plates that biased to 240 V. In the first experiment, the parallel aluminum plates are separated by 12 cm distance, and they were moved to 5 cm distance in the second experiment. Therefore, it is expected to increase the number of the rolling particles over the surface while increasing the number of the inter-particle collisions in order to decrease the microcavity charging requirement to overcome the contact forces. As a result, it is expected to increase the dust launching rates. In addition,

lower potential energy is required to build up within a microcavity in order to launch a dust grain when inter-particle collisions separate the attached dust grains.

4.3 Maximum Height and Initial Vertical Velocity Estimations

In the previous chapter, the estimation of the initial vertical launching velocities and the maximum heights are explained in detail. In the vacuum chamber experiments, there are critical parameters that are significantly different than the lunar surface. First, the surface cleanliness S is assumed as 0.13 in the vacuum chamber experiments (Wang et al., 2016), and this parameter is estimated as 0.88 for the lunar dayside and 0.75 for the lunar night side (Perko et al., 2001). Since this parameter is considerably higher on the lunar surface due to the high vacuum condition, weaker charging is required in order to detach a dust particle in the vacuum chamber even though the Earth's gravity acceleration is approximately 6 times of the lunar gravity acceleration. The following results are given in Fig. 4.7 by the estimation of enhanced charging number under the slow stream SW on the lunar terminator region and the vacuum chamber conditions with 450 eV electrons and approximately 8400 V/m surface electric field strength.

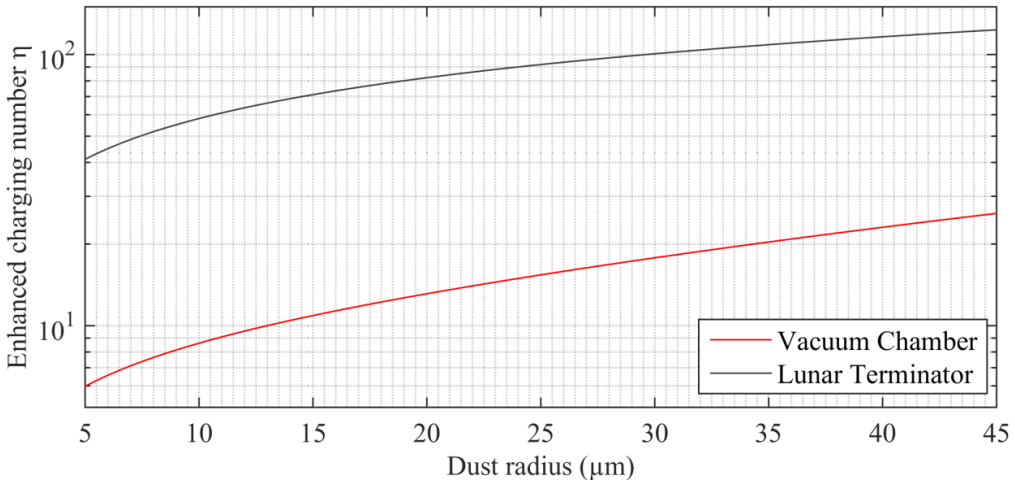

Figure 4.7 : Estimation of enhanced charging number η for the vacuum chamber conditions (S=0.13), the lunar terminator (S=0.75).

As it is mentioned in the previous section, Schawn et al. (2017) measured the charges of the silica microspheres with 21.2 μm radius as well as irregular-shaped particles, and the results show that all particles have charges larger than 10^5 e. Moreover, the mean value of the measured silica dust charge magnitude is lower than $3.0x10^5$ e

(Schawn et al., 2017), whereas the estimated value is approximately 4.682 x 10^{-14} C (2.922 x 10^5 e) charge (Fig. 4.8).

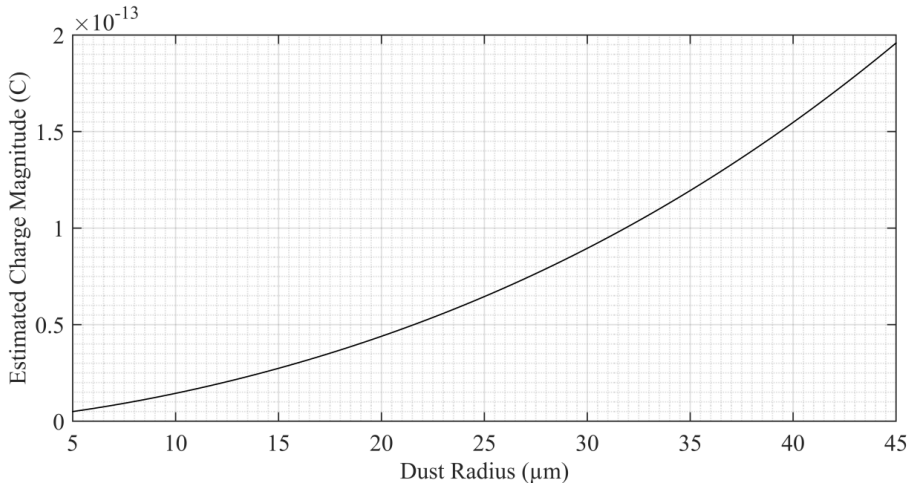

Figure 4.8 : Estimated charges of the lofted dust grains with 5-45 µm radius in the vacuum chamber experiments.

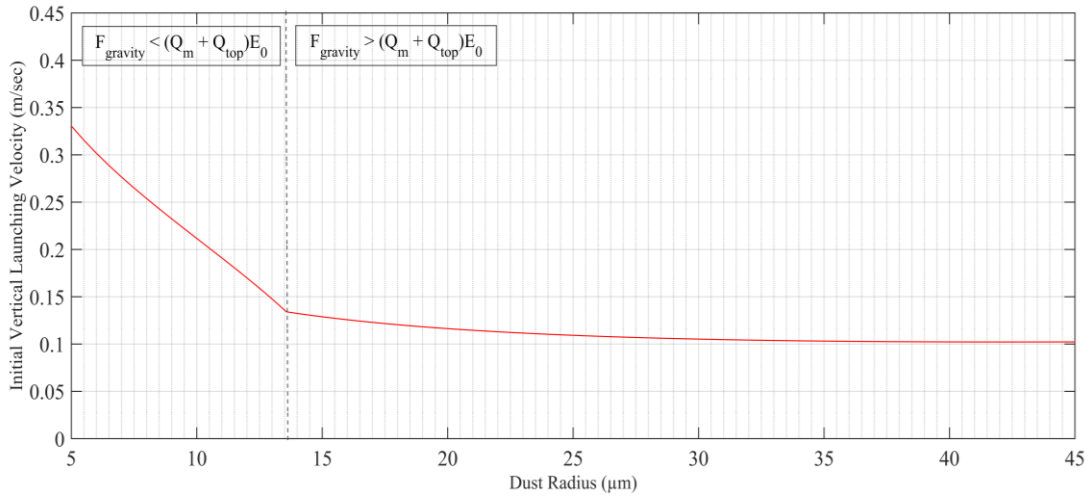

Figure 4.9 : Predicted the initial vertical launching velocities for the dust grains with 5-45 µm radius in the vacuum chamber.

According to the predicted values, it is expected to measure initial vertical launching velocities approximately between 0.1 and 0.35 $msec^{-1}$ in the ideal case (Fig. 4.9); however, these velocities can be higher if the actual contact forces are stronger than the estimation since it will require to collect higher repulsive potential energy within the microcavities to separate the dust grains. In addition, smaller-sized grains can be detected due to the enhanced light reflection near the surface even though their heights cannot be measured since they depart from the image frame due to higher velocities. For this reason, the measured maximum heights are particularly for the larger grains and potentially aggregates due to their surface area, which can reach

several millimeters above the dusty surface. According to the size limit of the camera image frame, the height measurements are up to approximately 2 cm above the surface. Therefore, the observed dust sizes are predicted as approximately 14-45 μm in radius (Fig. 4.10).

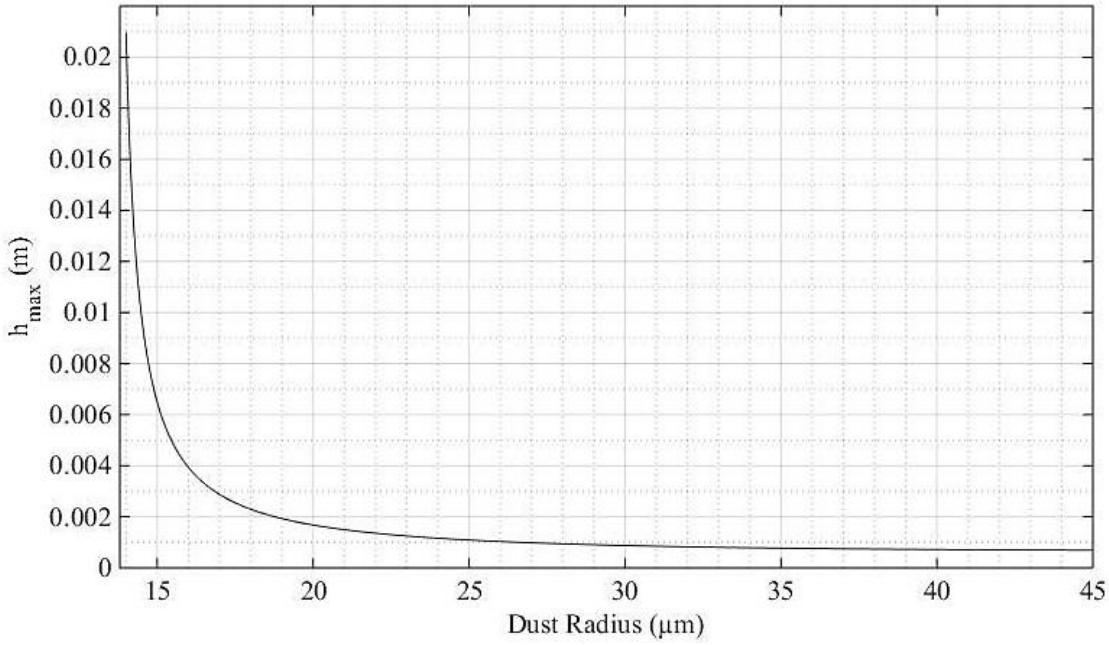

Figure 4.10 : Predicted observable heights within the image frame in the vacuum chamber,

4.4 Experimental Results

The measurement results are presented for the maximum heights and the initial vertical launching velocities detected by the high-speed camera. There are several observations that cannot be included in these results such as:

• Due to imperfect spherical shape and the rotational motion, some of the dust grains cannot be tracked since they cannot reflect sufficient light consistently.

• Some of the dust grains can travel away from the focus range of the microscopic telescope.

• A small number of particles depart from the sides of the image frame due to their velocity components parallel to the graphite surface.

• The dust grains with smaller sizes reach heights higher than the frame width (>20 mm).

Consequently, only the dust transportation observations detected with lifting and descending motion are included in the height measurements, and the vertical launching velocities are included only for the particles that can be detected during initial mobilization and in the following frames as well. In addition, there are different dust transportation observations such as the particle rolling (Fig. 4.11) or lofting of the aggregates and/or residues on the larger grains that can be detached during the motion.

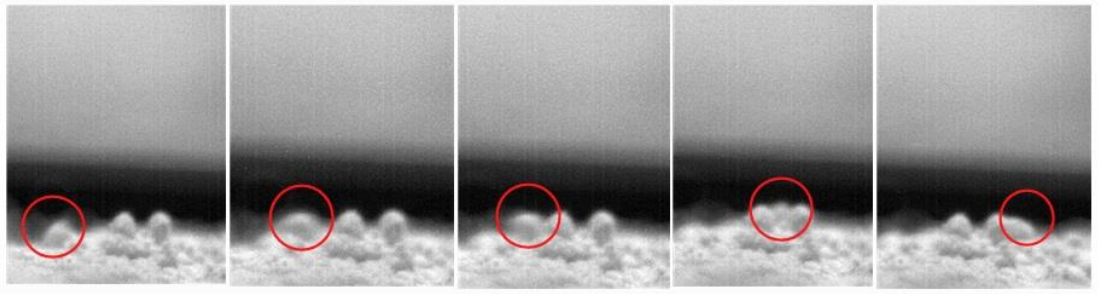

Figure 4.11 : Particle rolling in the vacuum chamber experiments.

4.4.1 Simple Case

The following experiments are performed with the dust samples prepared without any external pressure or horizontal electric field (Fig. 4.12), and they are repeated with the different dust samples to confirm the consistency of the results. The first experiment is performed under the electron beam with 450 eV energy and approximately 2.87 x 10^{-4}Am^{-2} current density, and the transportation of the silica dust grains is recorded with approximately 19.60 μm/pixel resolution, 250 fps camera speed and 1024 x 1024 image resolution.

Figure 4.12 : Scattered silica dust grains on the graphite plate after the exposure to the electron beam current.

Most of the dust particles are lofted up to approximately 3-4 mm (Fig. 4.13), and the initial vertical launching velocities are measured higher than the expected values for

a small number of the lofted grains. Even though the median and mean values of the results are considerably similar to the estimated heights and velocities for the ideal case, the higher velocities can be explained by the variation of the contact forces, or smaller particles with the sufficient brightness due to the reflected light in close proximity to the dust sample. Therefore, the results show higher velocities up to approximately 0.65 m/s for some observations. Finally, the median values of the height and velocity are determined as 0.0021 m and 0.1372 m/s, and the mean values are 0.0037 m and 0.1875 m/s.

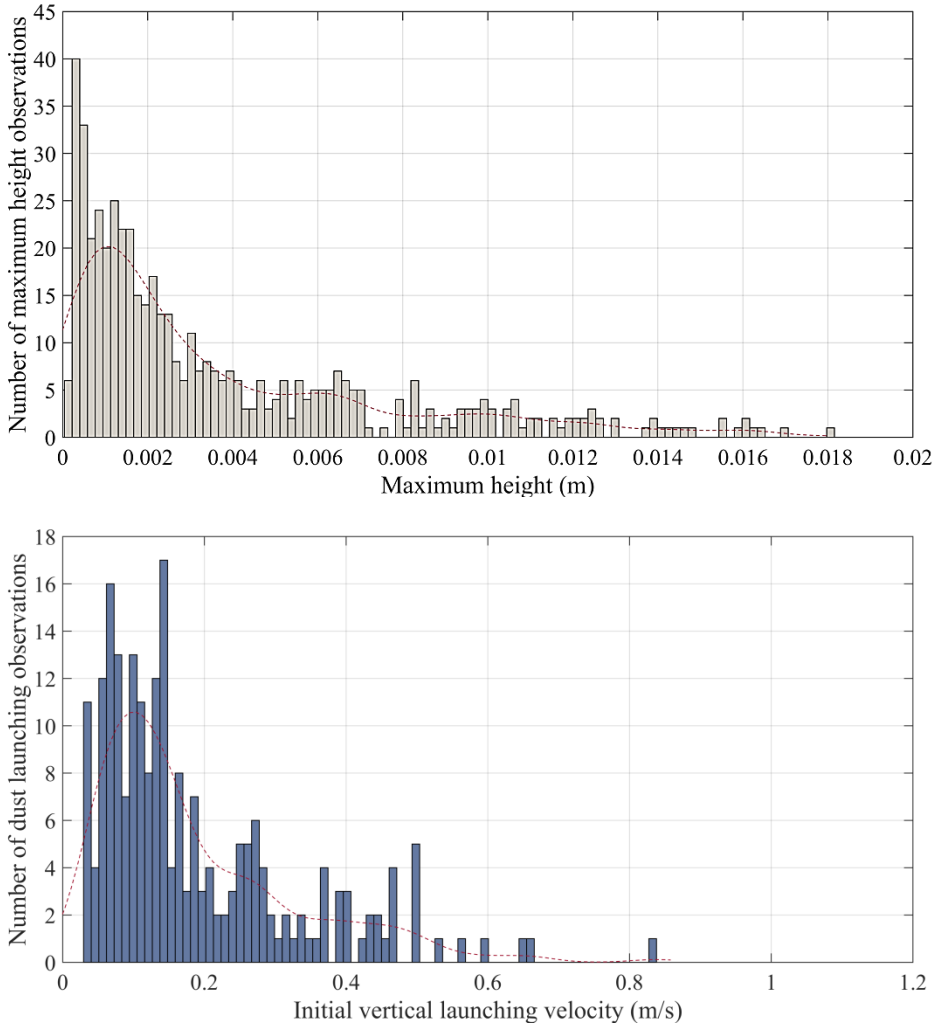

Figure 4.13 : Maximum heights (top) and initial vertical launching velocities (bottom) versus number of lofting dust observations.

The experiments are performed four times with separately prepared silica dust samples under the electron beam with 450 eV energy. In addition, a microscope scale is used to evaluate the pixel resolution of each experiment respectively, which is

determined by the image resolution and the distance between the dust sample and the microscopic telescope.

Similar to the first experiment, the camera resolution was 1024 x 1024 pixels, and the camera speed was chosen between 125, 250 and 500 fps options. These experiments were performed shorter than the first experiments since it aimed to observe the range of the measured values from the initial dust launching when the electron beam is started until the equilibrium condition when the dust transportation ends.

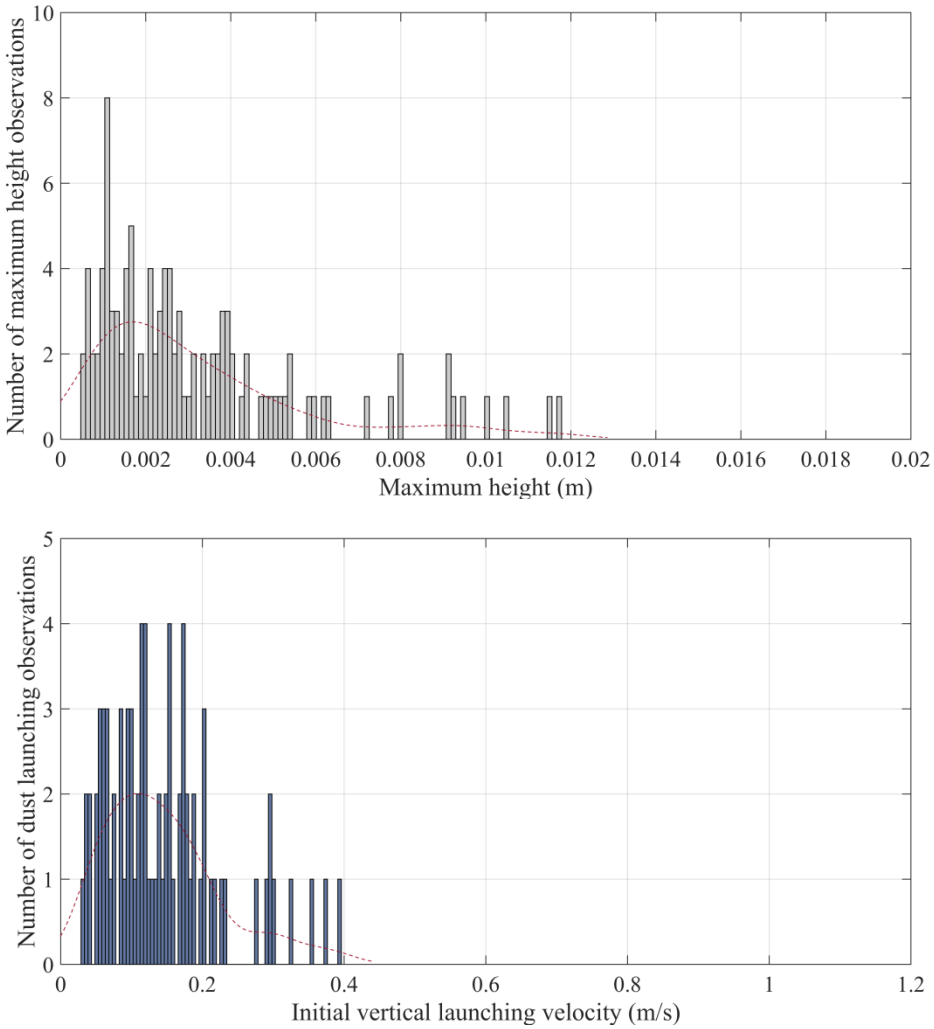

Figure 4.14 : Maximum heights (top) and initial vertical launching velocities (bottom) versus number of lofting dust observations captured with 125 fps speed.

Similar values are measured with the second dust sample when the camera speed is chosen as 125 fps. Even though the longer exposure time of the camera allowed many particles to be detected, it is determined as counterproductive since many particles changed direction between the frames. For instance, a lofting particle can be

observed ascending in a captured image frame and descending in the next image frame. The median values of the height and velocity are measured as 0.0025 m and 0.1247 m/sec, and the mean values are 0.0033 m and 0.1438 m/sec (Fig. 4.14).

The camera speed was selected as 250 fps, and the experiment was performed one more time by starting the electron beam with 450 eV. Around 70 particles were detected during the period less than 2 seconds. It is observed that more particles can be tracked definitely while determining their velocity and heights. The median values of the height and velocity are measured as 0.0016 m and 0.1331 m/sec, and the mean values are 0.0031 m and 0.1389 m/sec (Fig. 4.15).

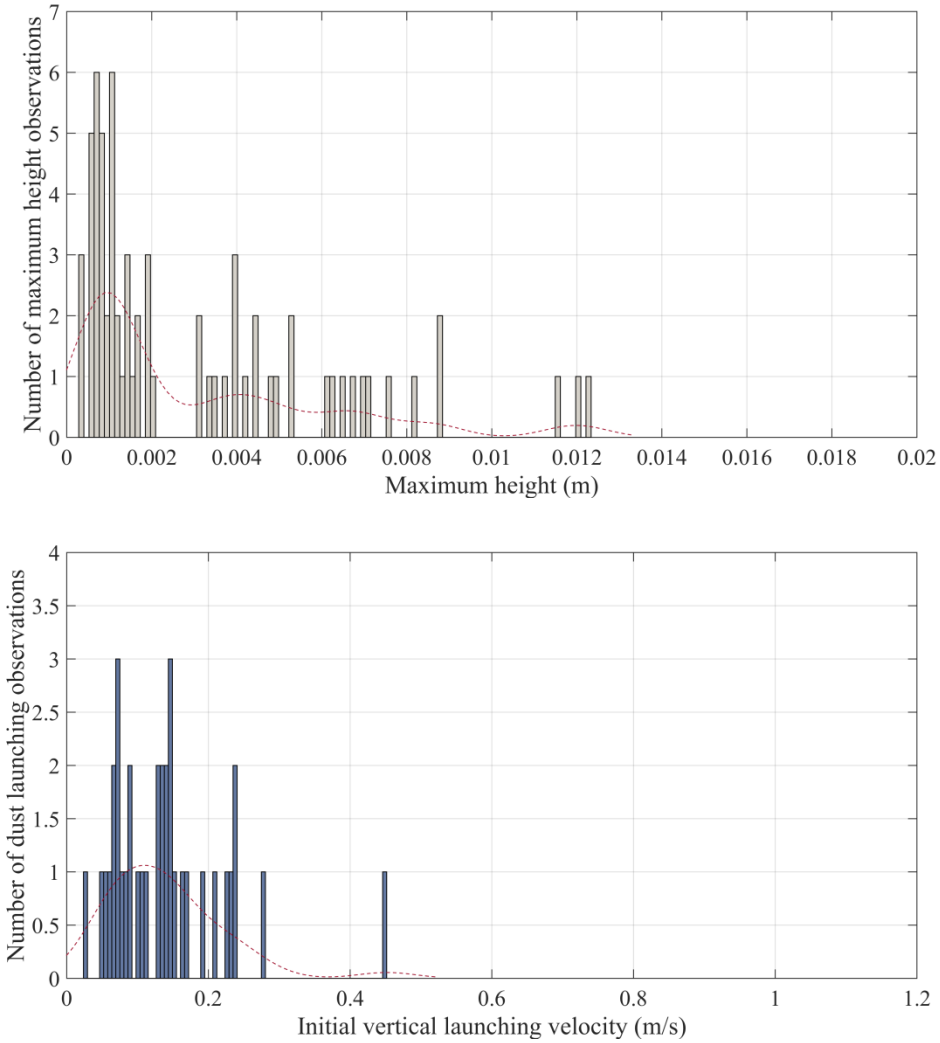

Figure 4.15 : Maximum heights (top) and initial vertical launching velocities (bottom) versus number of lofting dust observations captured with 250 fps speed.

Finally, the dust transportation is recorded with 500 fps speed in order to check the light conditions inside the chamber since the increased camera speed causes lower

integration period for the camera pixel values. It is determined that the brightness condition with the additional reflective surfaces is sufficient for 500 fps speed; however, the camera could record the experiment videos in particularly short intervals due to the internal memory limit. The median values of the height and velocity are measured as 0.0014 m and 0.1213 m/sec, and the mean values are 0.0024 m and 0.1392 m/sec (Fig. 4.16).

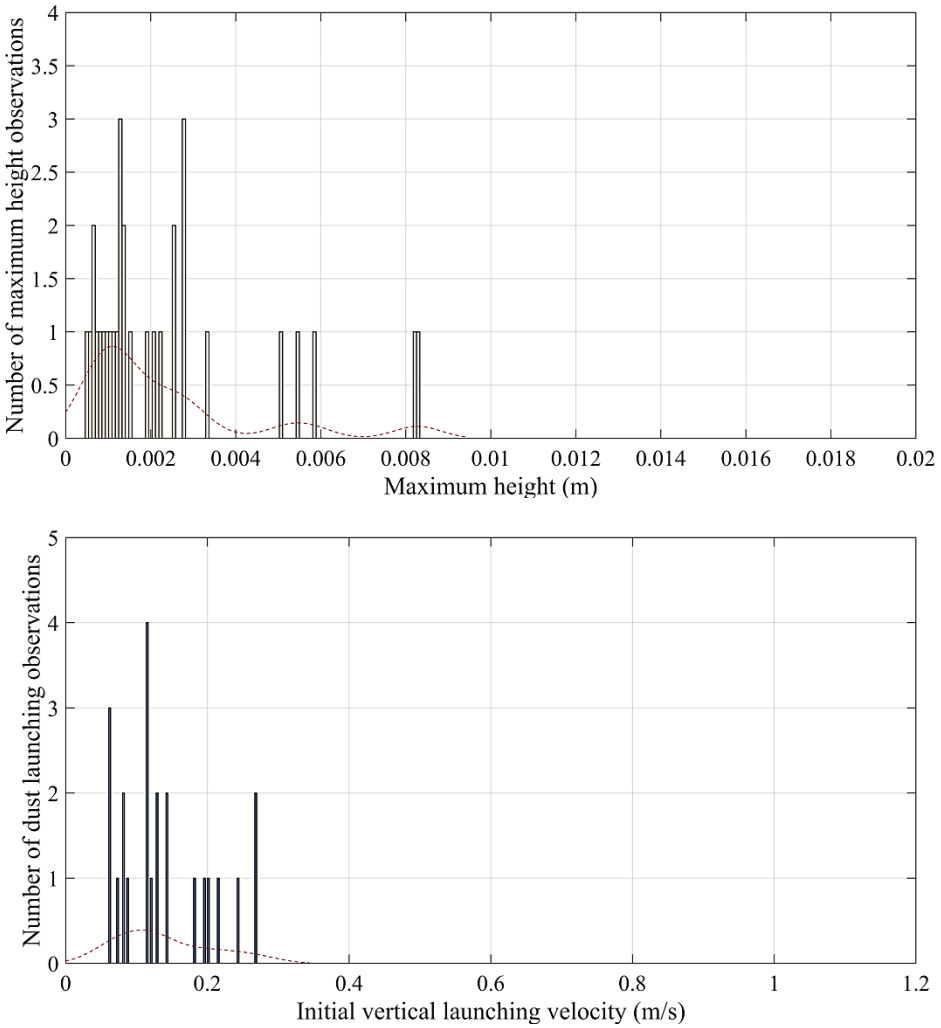

Figure 4.16 : Maximum heights (top) and initial vertical launching velocities (bottom) versus number of lofting dust observations captured with 500 fps speed.

According to the entire experimental results, the number of the velocity measurements is increased within the estimated range (Fig. 4.17), and a high number of the dust grains are lofted up to several millimeters as it is expected. Finally, the median values of the height and velocity measurements can be given as 0.0021 m and 0.1323 m/sec, and the mean values are 0.0036 m and 0.1698 m/sec.

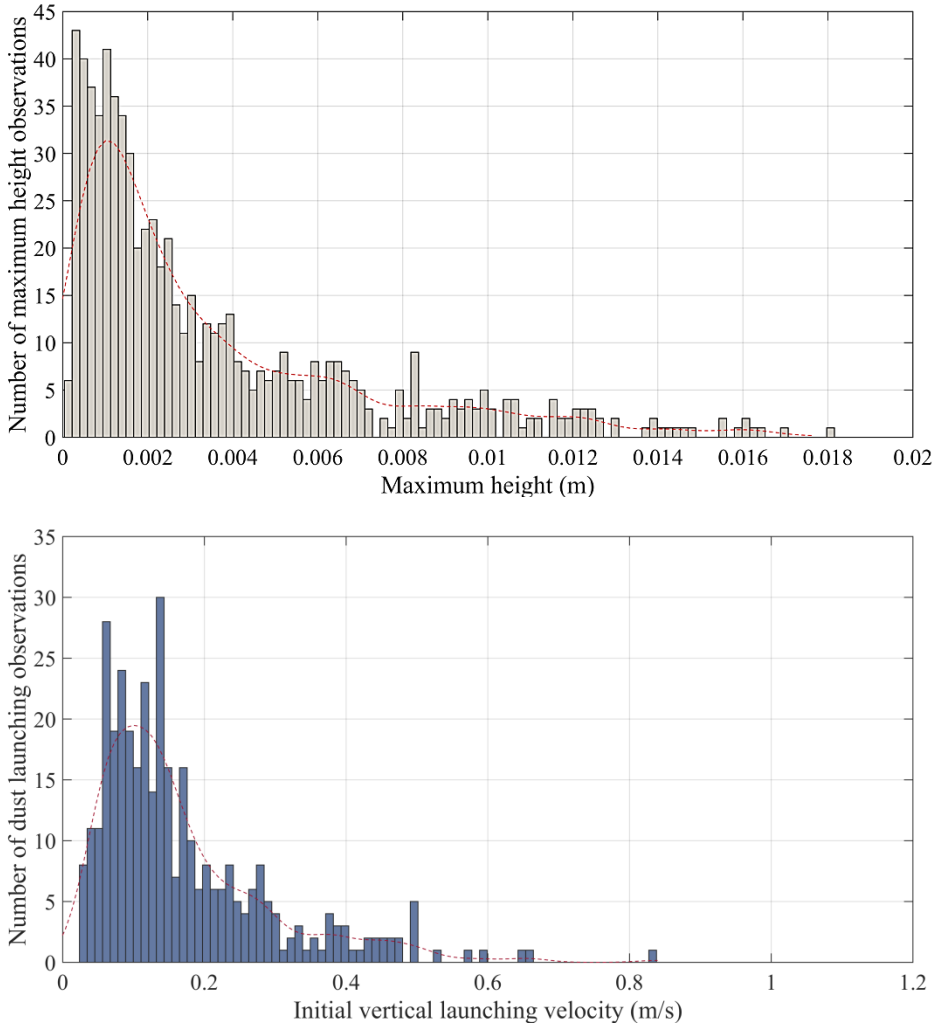

Figure 4.17 : Maximum heights (top) and initial vertical launching velocities (bottom) versus number of lofting dust observations during all experiments.

4.4.2 Experiments with Increased Packing Density

According to the condition given in equation 3.8, a longer charging within the microcavities and/or stronger surface electric field are required to detach the dust grains from the surface when the contact forces are enhanced or the gravity force is increased. It is expected that when the dust grains are pressurized to decrease the distance between the particles, the contact surface areas become larger, whereas the number of the microcavities is reduced (Fig. 4.18). Therefore, the dust grains require to build up higher potential energies in order to be separated from the neighboring particles. As a result, lower number of the dust lofting events must be observed accompanied with higher velocities than the previous experiments.

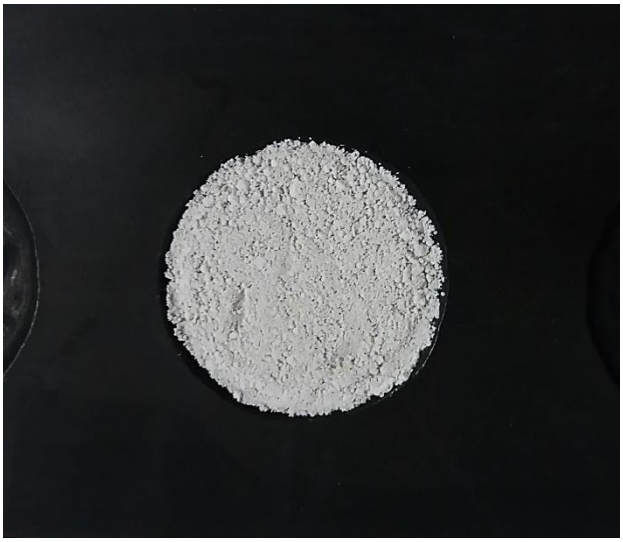

Figure 4.18 : Pressurized silica dust sample.

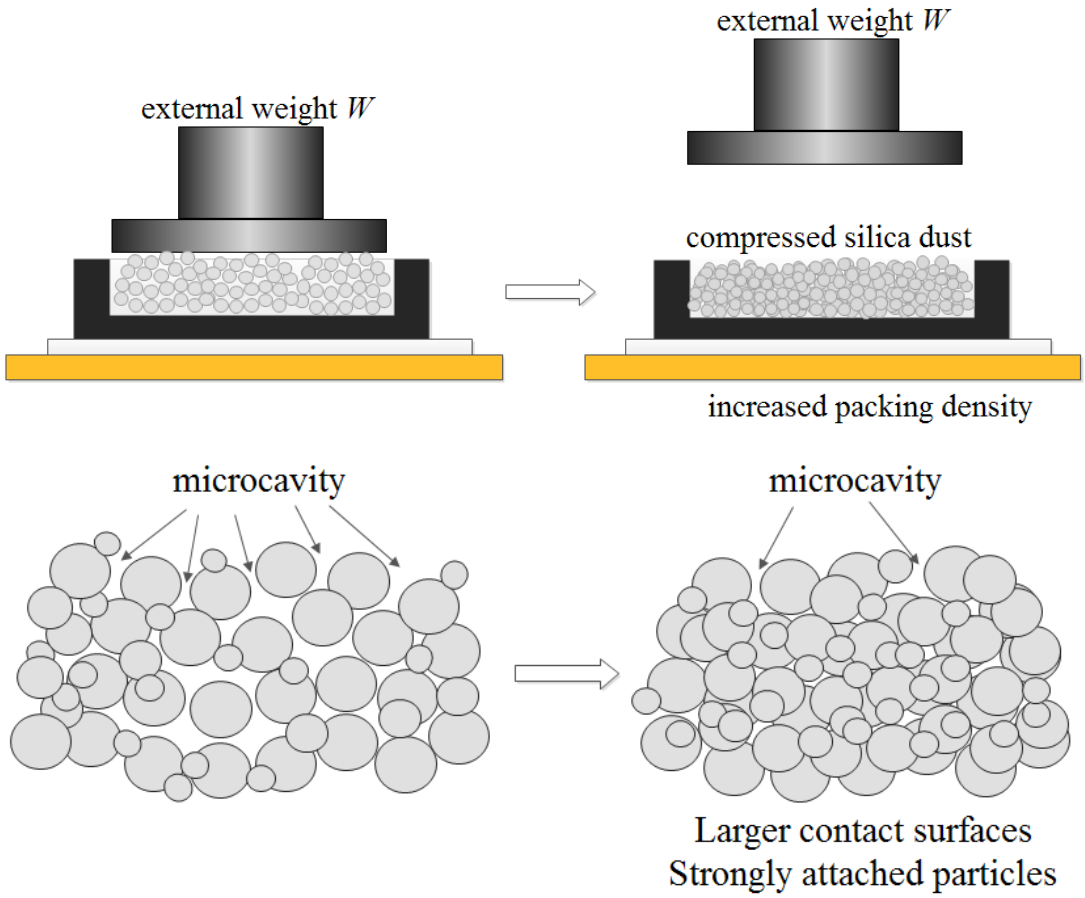

Figure 4.19 : Pressurizing the dust sample (top) and increased packing density (bottom).

The new dust sample is prepared similarly to the previous experiments; however, an external weight with the same diameter of the graphite plate hole is placed on the silica particles. Therefore, the dust grains are pressurized under 25 and 121 gram weights with 2 cm diameter, which corresponds to approximately 780.7 Pa and 3780

Pa (Fig. 4.19). The dust transportation recorded with 250 fps speed and 1024 x 1024 image resolution under the same vacuum condition and the electron beam current with 450 eV energy. In addition, the resolutions are deteremined as 14.07 and 13.33 μm/pixel, respectively.

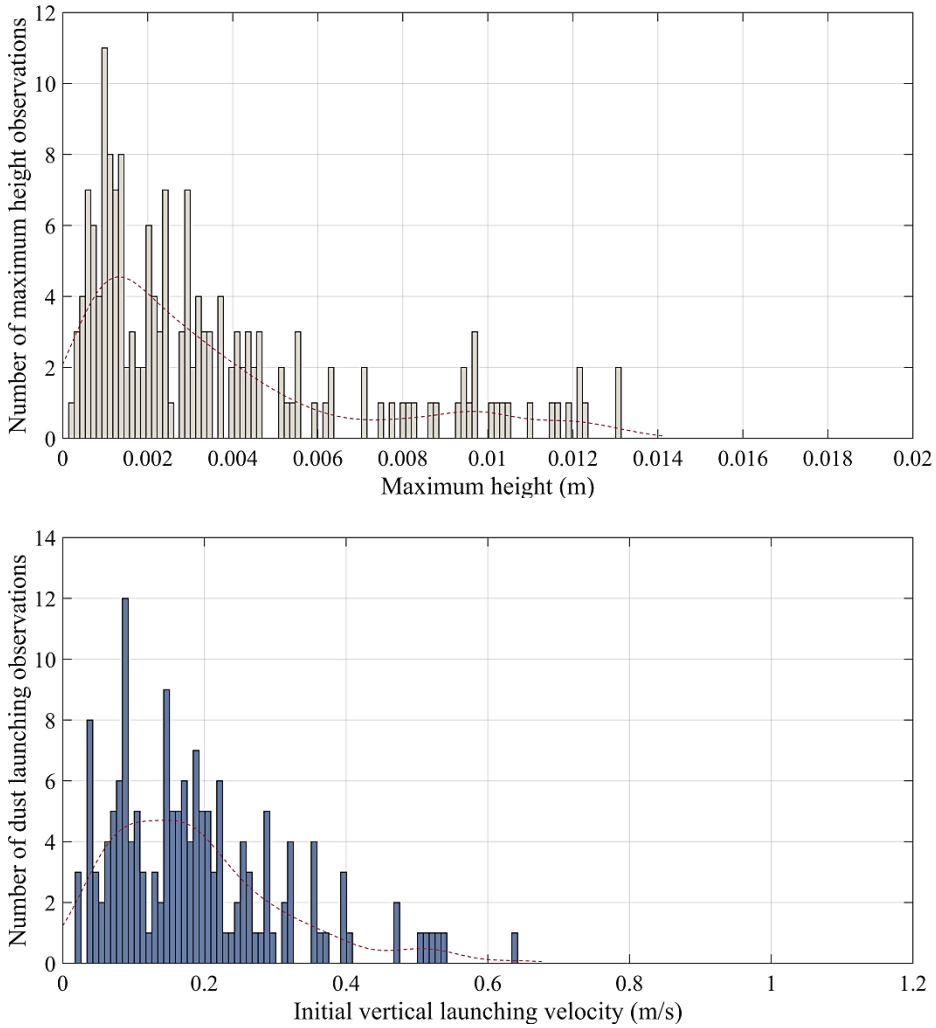

Figure 4.20 : Maximum heights (top) and initial vertical launching velocities (bottom) versus number of lofting dust observations after applying 780.7 Pa pressure.

According to the dust launching observations, some of the dust grains leave the image frame by reaching heights over 2 cm. For this reason, comparing the initial vertical launching velocities is more preferable than the maximum heights. Since the contact forces are enhanced between the neighboring dust grains, a small number of dust launchings are observed, and their initial vertical launching velocities are higher than the predicted values as well as the previous experimental results (Fig. 4.20). According to these measurements, the median value of the velocity is determined as 0.1649 m/sec, and the mean value is 0.1863 m/sec when 780.7 Pa pressure is

applied to the dust particles. On the other hand, the median value of the velocity becomes 0.2300 m/sec, and the mean value is 0.2707 m/sec after 3780 Pa pressure (Fig. 4.21).

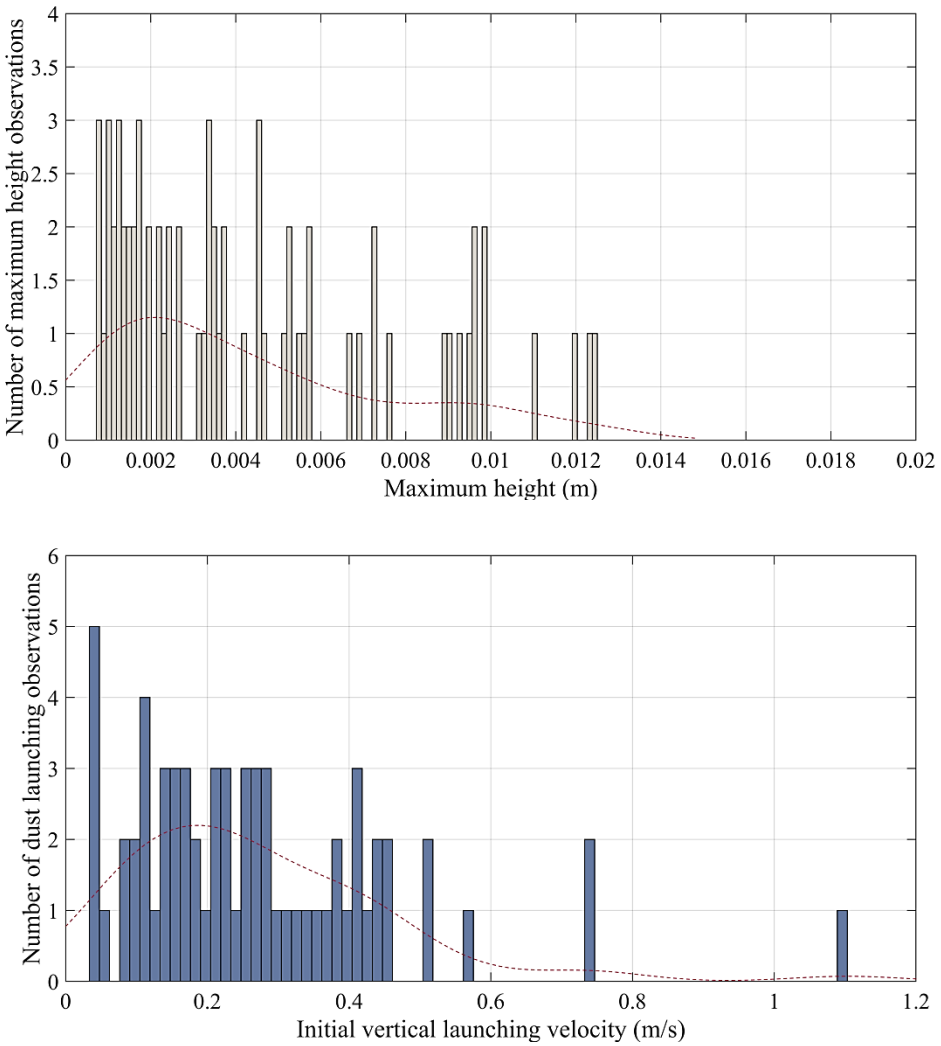

Figure 4.21 : Maximum heights (top) and initial vertical launching velocities (bottom) versus number of lofting dust observations after applying 3780 Pa pressure.

4.4.3 Experiments with Horizontal Electric Field

In the final experiments, the graphite plate is placed between two parallel aluminum plates that are separated by 5 and 12 cm distance and biased to 240 V. Therefore, it is expected to increase the number of the rolling particles over the surface while increasing the number of the inter-particle collisions in order to decrease the microcavity charging requirement to overcome the contact forces when the horizontal electric field becomes stronger. As a result, it is expected to increase the dust launching rates. In addition, lower potential energy is required to build up within

a microcavity to launch a dust grain when inter-particle collisions separate the attached dust grains.

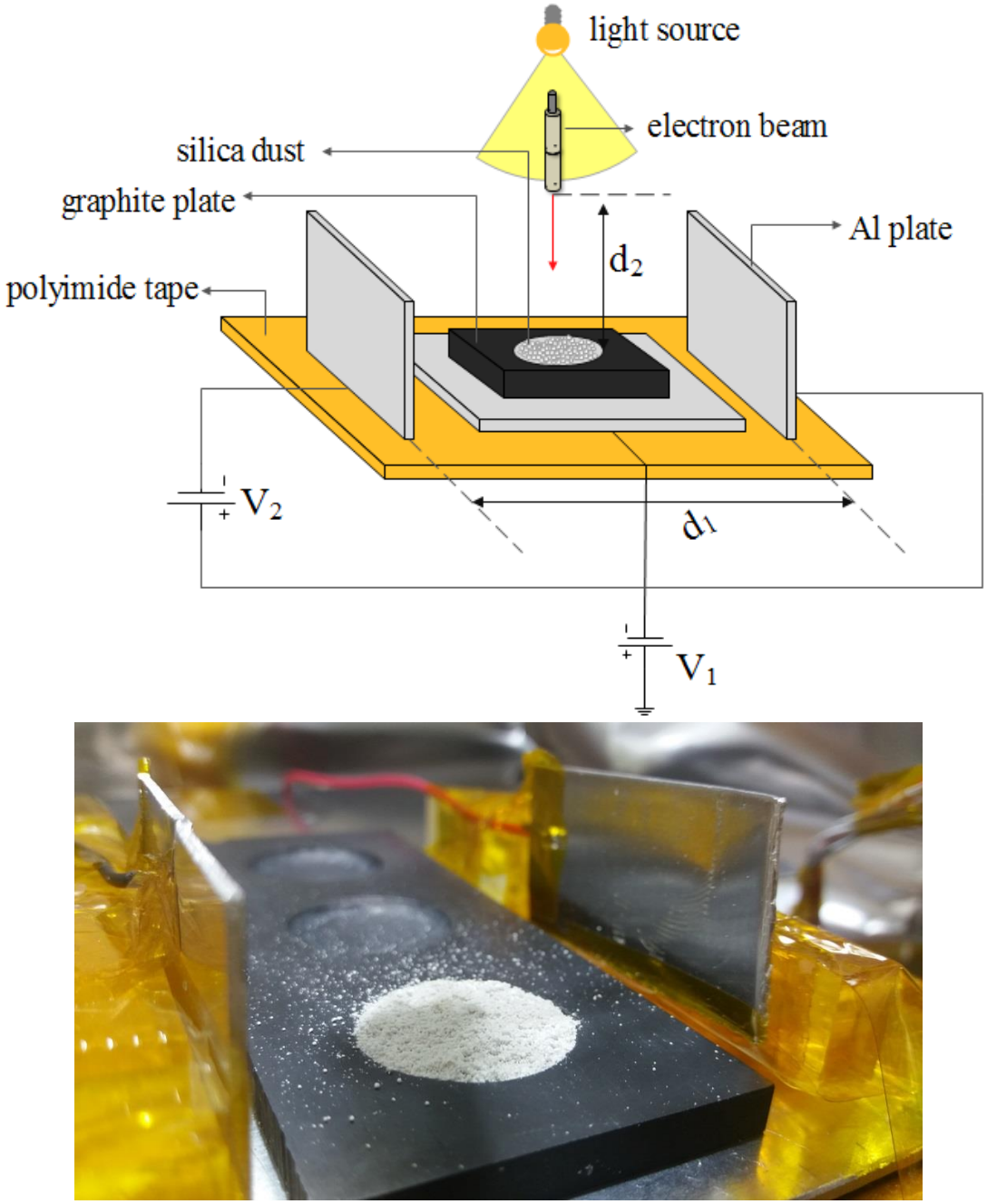

Figure 4.22 : Test environment schematic (top) and dust sample between the parallel aluminum plates (bottom).

According to the dust launching observations, a high number of dust grains are launched from the surface in a significantly short time. In addition, there were a high number of rolling dust grains, which produced inter-particle collisions.

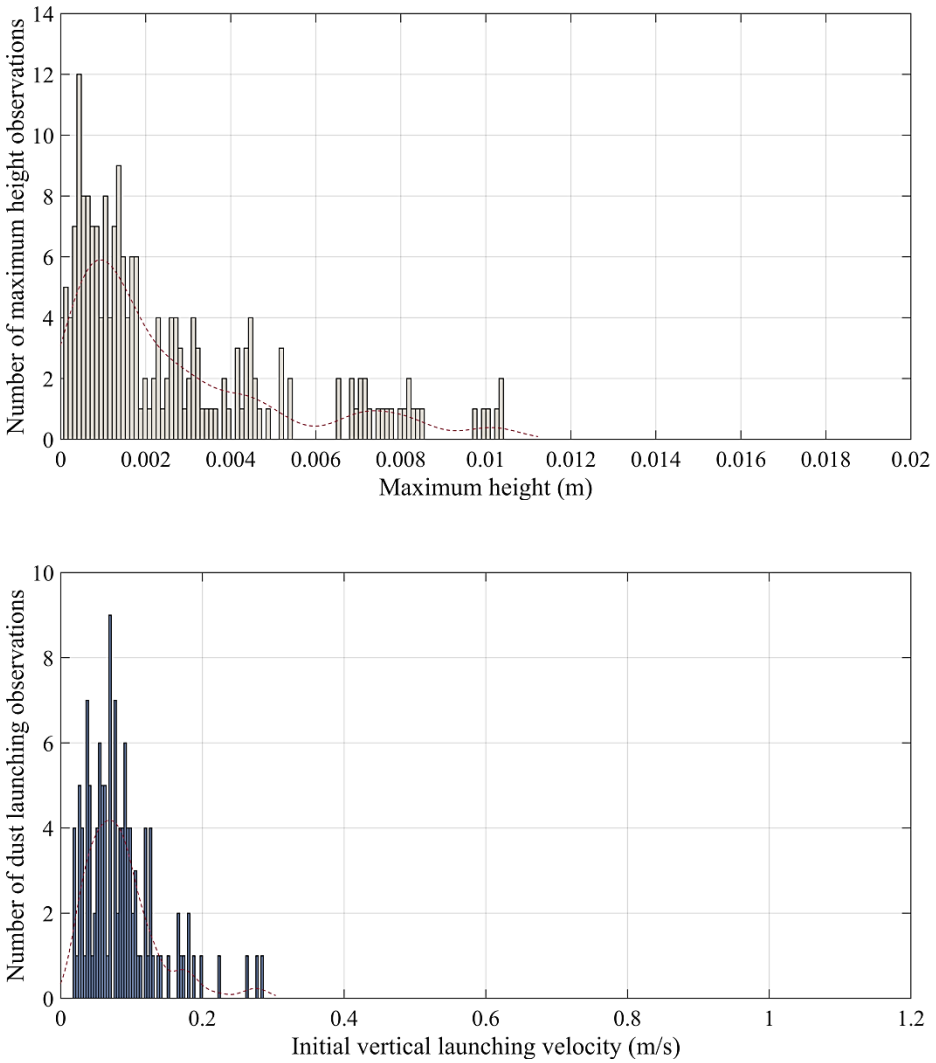

Figure 4.23 : Maximum heights (top) and initial vertical launching velocities (bottom) versus number of lofting dust observations with 2000 V/m.

When approximately 2000 V/m horizontal electric field is applied, the measurements show that the median values of the height and velocity measurements can be given as 0.0016 m and 0.077 m/sec, and the mean values are 0.0026 m and 0.085 m/sec (Fig. 4.23). On the other hand, the median value of the velocity is determined as 0.0738 m/sec, and the mean value is 0.0961 m/sec. In addition, the mean and median values of the heights are measured as 0.0025 m and 0.0016 m, respectively (Fig. 4.24).

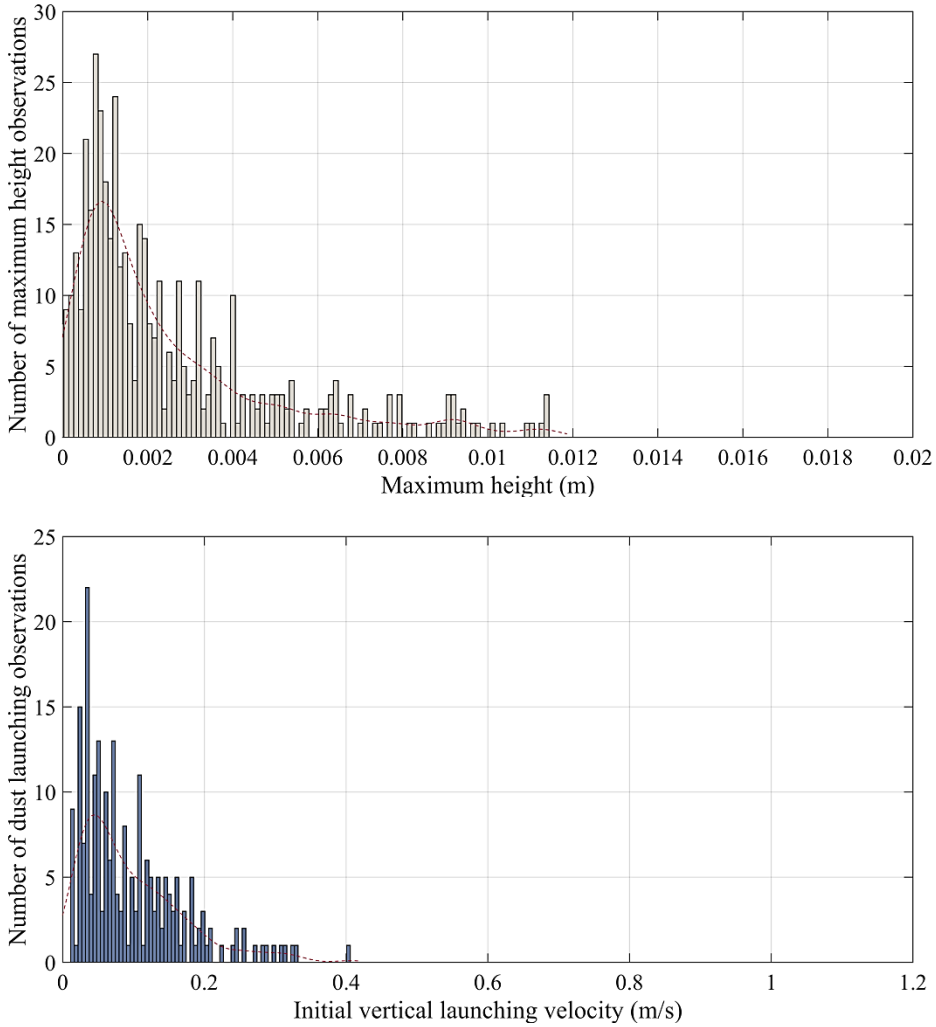

Figure 4.24 : Maximum heights (top) and initial vertical launching velocities (bottom) versus number of lofting dust observations with 4800 V/m.

4.4.4 Separation of Lofted Dust Grains

During the experiments, a trajectory of a tracked particle diverges into several branches in some cases (Fig. 4.25). Even though it is an occasional observation compared to the transportation of single dust grains or aggregates, it is suspected that some of the particles could be transported while being carried by other dust grains (Fig. 4.26). Even though it can explain some of the observations, the detected pixels indicate that the aggregates that are composed of single particles with the comparable sizes could be responsible in addition to the transportation on the larger grains. Furthermore, similar dust sizes are suggested after investigating the number of the pixels over the detected trajectories.

In order to investigate the nature of the lofted dust grains, a polyimide tape is placed near the graphite plate to collect the dust grains with its adhesive surface (Fig. 4.27).

In order to minimize the chances of several particles landing on the same location after being lofted, the electron beam is turned off immediately after the first dust launching observation. When it is investigated under the microscope, single particles were observed on the polyimide tape (Fig. 4.28), whereas the aggregates were present over the graphite plate itself since most of them traveled less distance than the single particles. Therefore, it is probable that obscured surfaces of the aggregates become exposed to the incoming electron current after the initial launching, and the attached particles repulse each other while the rotation motion contributes to cancel the contact force.

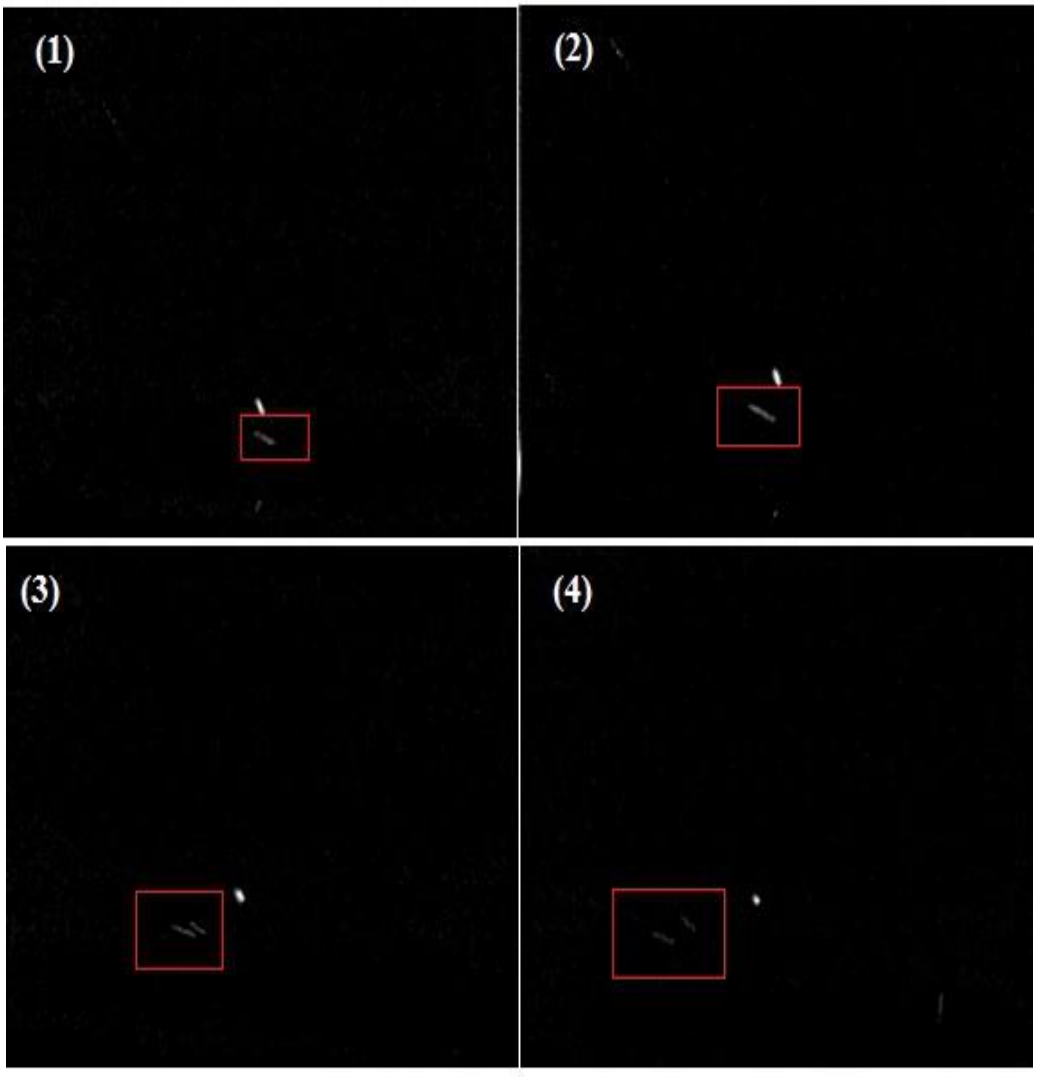

Figure 4.25 : Trajectory branching observation of a potentially separated aggregate with the frame numbers.

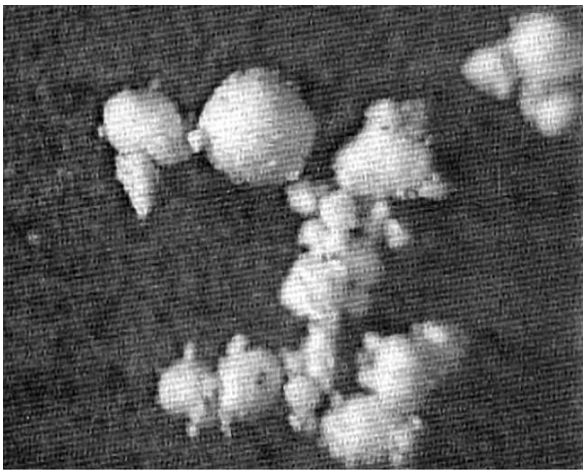

Figure 4.26 : Scattered silica dust grains on the graphite plate after the exposure to the electron beam current.

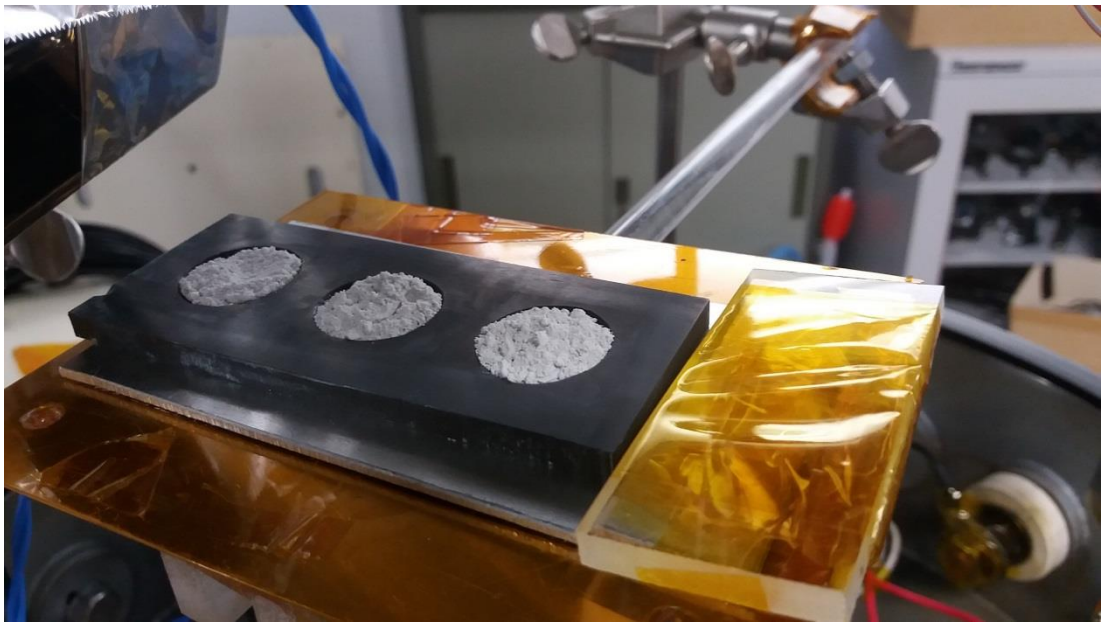

Figure 4.27 : Polyimide tape that is placed next to the graphite plate.

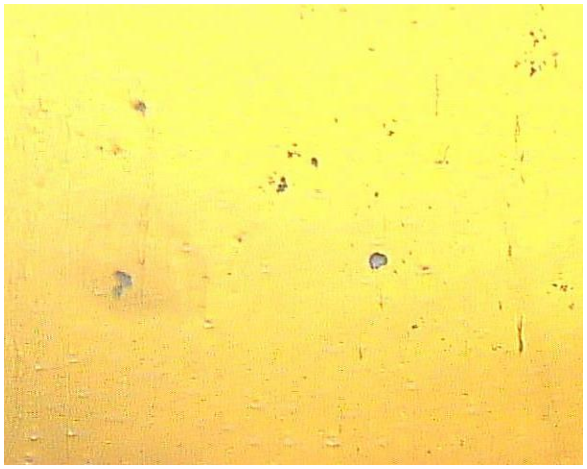

Figure 4.28 : Collected single dust particles on the polyimide tape.

5. DISCUSSION

5.1 Simulation Results

5.1.1 Lunar Terminator Region Results

The results of the terminator region surface charging, the maximum reachable dust heights, and the dead zone location point out that:

- Upstream electron current controls the surface charging and the emitted electrons within the microcavities between the dust grains. Therefore, it determines the charging time of the detached dust particles and the relative maximum heights above the lunar terminator.
- The plasma density is an important parameter to loft the dust particles to higher altitudes since it controls the electron sheath thickness. Higher density produces thinner electron sheath while increasing the electric field; however, a smaller distance for the acceleration of charged dust grains decreases the maximum heights. Therefore, an average density value with higher electron temperature can increase the heights of the charged dust grains as it is seen in the third CME event.
- Debye sheath thickness ranges from 1.656 m to 30.68 m while the electric field is between -13.67 V/m and -0.574 V/m. In addition, the surface potential values are between -131.3 V and -9.393 V during the studied CME events.
- The post-shock plasma passages, which are accompanied with warm and dense plasma, produce stronger surface electric field on the lunar terminator. Furthermore, higher rates of the secondary electron emission can increase the number of the launched dust grains from the surface while electrostatic forces acting on the dust particles are stronger than the other conditions.
- During the early CME passages, low density decreases the electron current to the lunar surface accompanied with colder plasma temperatures. Therefore, the electric field is weaker in these cases, and the secondary electron emission

current decreases significantly. For this reason, the dust grains cannot be detached from the surface for long periods.

- A solar flare event does not influence the terminator region surface charging similar to the SW bulk velocity variations; however, stronger photoemission moves the dead zone location closer to the terminator region. Therefore, the region that negatively charged dust particles are repelled from the surface decreases between the lunar dayside and terminator.
- Upstream electrons become very cold during the late CME passages, and the surface potential is also weaker in all three events even though the density becomes very high. Therefore, the dust heights have lower values than the most cases. On the other hand, the secondary electron emission ratios increase due to high plasma density. As a result, higher rates of dust particles can be launched to lower altitudes.

5.1.2 Variation of Dead Zone Location

The dead zone location shifts between approximately 56^{o} and 90^{o} during the passage of the selected CME events. In addition, there can be a relation between the dead zone location and the lofted dust population above the terminator region in some cases. The following results are given in solar zenith angle for the maximum and minimum values in Table 5.1, which are calculated by the equilibrium of the flowing plasma equations.

Table 5.1 : Dead zone location results.

	min	max
CME Event 1	56.52 ^{o}	89.94 ^{o}
CME Event 2	64.30 ^{o}	89.49 ^{o}
CME Event 3	56.59 ^{o}	89.76 ^{o}

Strong electron current from the upstream plasma, which is controlled by plasma density and electron temperature, expands the negatively charged surfaces to the dayside of the Moon. Since the CME post-shocks are accompanied with warm and dense plasma, they are expected to move the dead zone away from the terminator region while increasing the maximum dust heights. On the other hand, high plasma density has a similar effect on the dead zone during the late CME passages even though it co-occurs with the cold electrons. Therefore, the dust heights are expected

to be low even though the dead zone is moved closer to the subsolar point in those cases.

Equation 2.45 can be used for a quick estimation of the dead zone location when the density and the solar wind flow velocity are not significantly high. The difference between equation 2.45 and the solution of the flowing plasma equations are calculated as low as 6.830×10^{-6} degree, 4.303×10^{-4} degree and 4.781×10^{-5} degree during the early-CME passages of the three CME events, respectively. On the other hand, high values of the SW velocity and plasma density are present during the post-shock plasma and CME-driver gas passages, which contribute to the flowing component of the charging current equations; therefore, the difference between equation 2.45 and the solution of the flowing plasma equations can increase up to approximately 10 degrees. For this reason, the flowing plasma equations are used in the given results and figures in the previous chapters.

5.1.3 Electrostatic Dust Lofting

Electrostatic forces acting on the lunar dust grains are modified considerably during the passage of CMEs; however, the dust heights show that strong electrostatic force due to the electric field enhancement is not able to loft dust particles off the surface to higher altitudes in all cases. The dust particles migrate within the electron sheath quickly, and they do not accelerate to the sufficient vertical velocities. Accordingly, they return to the lunar surface under the gravity force in a shorter time. The maximum heights h_{max} are given together with the surface potential ϕ_s, the initial vertical launching velocities V_{0z}, the enhanced charging number η, the electric field E_0, Debye length λ_D, the plasma density n_0, the electron temperature T_e, the dead zone location θ_{DZ}, the secondary electron emission ratio J_{sec}/J_{secSW} and the solar wind bulk velocity V_{SW} in Table 5.2.

These results show the importance of the combination of several conditions such as the thickness of the plasma sheath above the lunar surface, charging of the dust particles due to emitted electrons and the strength of the electric field above the surface. Maximum heights for the dust particles 5 μm in radius are present when the plasma is significantly dense; therefore, the dead zone has lower solar zenith angles, and the secondary electron emission ratio increases at the same time. Moreover, submicron-sized dust particles reach the maximum altitudes under average plasma

density with warmer electrons in the third event while a strong negative surface potential is accompanied with high secondary electron emission ratio. Therefore, the dust heights can increase together with higher rates of dust launching from the surface in that condition while the dead zone location moves closer to the subsolar point. In addition, the ranges of the estimated heights are given in Table 5.3.

Table 5.2 : The conditions of maximum dust heights over the lunar terminator.

	CME 01			CME 02			CME 03		
	0.1 μm	1 μm	5 μm	0.1 μm	1 μm	5 μm	0.1 μm	1 μm	5 μm
h_{max} (m)	188.5	5.913	0.324	242.5	7.517	0.325	541.2	18.22	0.344
V_{0Z} (m/s)	6.670	2.155	0.964	6.670	2.155	0.964	6.670	2.155	0.964
η	5.817	18.37	41.07	5.817	18.37	41.07	5.817	18.37	41.07
ϕ_s (V)	-43.53	-35.18	-24.54	-56.80	-47.78	-46.59	-131.3	-131.3	-127.1
E_0 (V/m)	-5.208	-6.288	-9.036	-4.493	-9.082	-9.187	-12.75	-12.75	-13.67
λ_D (m)	8.357	5.595	2.716	12.64	5.260	5.071	10.30	10.30	9.301
n_0 (cm^{-3})	7.355	15.81	49.67	5.000	22.90	24.25	16.74	16.74	20.53
T_e (eV)	9.295	8.953	6.630	14.46	11.46	11.28	32.15	32.15	32.14
$\theta_{DZ}(^o)$	82.68	75.57	56.52	83.80	66.19	65.04	62.06	62.06	56.59
J_{sec}/J_{secSW}	0.645	1.359	3.677	0.547	2.229	2.341	2.729	2.729	3.347
V_{SW}(km/s)	380.4	482.5	477.1	463.9	368.1	363.0	737.0	737.0	763.2

Table 5.3 : The maximum and minimum heights for the lofted dust grains with 0.1, 1 and 5 μm radius.

	CME 01		CME 02		CME 03	
	h_{min} (m)	h_{max} (m)	h_{min} (m)	h_{max} (m)	h_{min} (m)	h_{max} (m)
0.1 μm	67.11	188.5	63.53	242.5	50.62	541.2
1 μm	1.565	5.913	1.757	7.517	1.561	18.22
5 μm	0.293	0.324	0.295	0.325	0.293	0.344

5.2 Experimental Results

Several experimental investigations are compared with the predicted values for the spherical silica dust grains with sizes between <6 and 45 μm in radius. Even though the given equations are applied with the basic assumptions, the most of the predictions are in agreement with the experimental results in our laboratory for the simple case. In addition, the initial vertical launching velocities show that there are particles being launched with the higher velocities than the predictions even though the most of the measurements are in the estimated range. Consequently, it could be

the result of two potential sources. First, the dust grains with smaller sizes can be detected near the dust sample due to the enhanced light reflection from the silica dust sample. Second, the contact forces can deviate among the particles remarkably. Therefore, a strongly attached particle can build up a higher potential energy until being detached from the other dust grains, which can be contributed to the increased packing density or a higher surface cleanliness parameter as it is seen in Fig. 4.7. For this reason, two different external pressure levels were applied to increase the packing density of the dust samples, and the vertical launching velocities were measured. As a result, the measurements validated the relationship between the contact forces and the dust launching speeds. Since the number of the micro-cavitities was decreased as well, a smaller number of particles were able to attain sufficient charges to be detached from the surface. Table 5.4 shows the overall experimental results, and n_h and n_v are the number of height and initial vertical launching velocity observations, respectively.

Table 5.4 : The experimental results.

Experiment	Maximum Height (mm)			Initial Vertical Velocity (m/s)			Time (s)
	Mean	Median	n_h	Mean	Median	n_v	
Basic Sample							
Sample 1	3.75	2.15	508	0.19	0.14	221	32.64
Sample 2	3.28	2.51	111	0.14	0.12	81	32.64
Sample 3	3.12	1.57	68	0.14	0.13	36	1.80
Sample 4	2.36	1.38	31	0.14	0.12	23	1.22
Total	3.56	2.15	718	0.17	0.13	361	68.30
Increased Packing Density							
780.7 Pa	3.62	2.41	170	0.19	0.16	159	81.84
3747.1 Pa	4.37	3.41	69	0.27	0.23	66	81.84
Horizontal Electric Field							
2000 V/m	2.65	1.61	200	0.09	0.08	123	24.55
4800 V/m	2.51	1.59	439	0.10	0.07	221	40.92

In all experiments, the mobilized particles demonstrate several types of motions such as lofting, rolling, inter-particle collisions and separation after being launched as a group. In order to observe particle-particle collisions and rolling motion, the microscopic telescope is placed in a closer distance to the dust sample by focusing on a smaller area. Even though it is not convenient to measure the launching velocities and the maximum heights in a significantly small frame size, it showed that rolling

particles are a potential source to cancel contact forces of other dust grains. Therefore, if an external force can detach a particle from the contact forces, the required charge magnitude will be decreased compared to a dust grain that is lofted solely by the electrostatic forces. For this reason, these particles can reach a similar height or lower by the electrostatic forces depending on the current charge state. In order to test this, the graphite plate is placed between two parallel aluminum plates that are separated by 5 and 12 cm distance and biased to 240 V in two different experiments. A higher number of the rolling particles were detected in the particle trajectory tracing code; therefore, it potentially increased the number of the inter-particle collisions. As a result, the vertical launching velocities decreased according to the current results (Table 5.4).

According to the observations with the high-speed camera and the microscopic telescope, the mobilized silica particles are composed of single dust grains, large aggregates and small-sized grains carried on the larger particles, which are also mentioned for Mars simulants in the previous experiments (Schawn et al., 2017). Even though some of the separation observations could be a result of the carried residues, other observations suggested comparable dust sizes since the trajectories and the number of the detected pixels are considerably similar. In conclusion, the measurements during the laboratory experiments points out that:

- According to the laboratory measurements of the heights and the vertical launching velocities, the median values are determined as 0.0021 m and 0.1323 m/sec, and the mean values are 0.0036 m and 0.1698 m/sec for the silica dust grains with sizes between < 6 and 45 μm in radius for the simple case.
- Enhanced packing density of the dust grains limits the particle launching while increasing the launching velocities since the median and mean values of the velocities increase with the applied pressure level.
- Presence of a horizontal electric field enhances the dust mobilization. Even though the horizontal electric field does not influence the vertical motion directly, the median and mean values of the velocity measurements show that the inter-particle collisions and rolling motion decrease the charging requirement for the lofted particles.

- Secondary electron emission and absorption play a determinative role in the dust charging and lofting. Consequently, the charge and the transportation of the lofted dust grains can be estimated with the patched dust-charging model (Wang et al., 2016). As a result, the required charge to loft a single dust particle is estimated above 10^5 e for the most of the spherical silica dust grains with sizes between < 6 and 45 μm in radius, which are in agreement with the measurements.
- The aggregates composed of the spherical particles can be separated after they are launched from the surface as well as the small residues, which can be a result of the particle rotation and the incoming electron current under the electron beam.
- The dust grains can start to roll and/or collide on the dusty surface while the smaller-sized particles are launched due to the additional external forces applied together with the electrostatic repulsion. Therefore, other particle motions can enhance the number of the lofted particles.

6. CONCLUSIONS AND RECOMMENDATIONS

6.1 Conclusions

The lunar dust particles can have a high number of configurations when the microcavity sizes and the number of microcavities that are exposed to the incoming SW electrons are considered. In this work, a simplified version of the dust launching from the surface is presented for the isolated dust particles, which are charged on their patch surfaces within a single microcavity separated by the comparable distances to the dust particle size. The main contributions can be listed as:

1. Charging requirement to launch a dust grain from the surface as a function of microcavity size *s*, the emitted electron temperature T_{ee}, dust grain radius size a, surface cleanliness parameter due to the surface temperature variations *S* and the lunar surface electric field E_0.
2. Initial vertical launching velocities are estimated and expressed as a function for the dust grains on the lunar surface.
3. Microcavity size parameter s is estimated as the particle diameter due to the agreement with the laboratory experiments, producing the same results with the Surveyor observations of the LHG, and considerably similar dust heights with the Lunokhod-2 light-scattering observations.
4. Shock plasma of a CME passage is found to increase the dust launching rates, whereas it does not always increase the maximum reachable heights of the dust grains. Therefore, the electron sheath thickness is a critical factor for the submicron-sized dust grains.
5. It is challenging to launch the smaller-sized dust grains due to the small-scale microcavity size and the limited surface area to collect the emitted electrons in order to be sufficiently charged.
6. Dust lofting is calculated with the time step of 10^{-4} seconds to update the charge, velocity, and height of the launched dust grains, and the simulations easily produce the LHG observations of the Surveyor

missions. Furthermore, the submicron-sized grains reach the similar altitudes with the Lunakhod-2 observations under the regular SW parameters.

For the laboratory experiments, there are several contributions to the field as:

1. Silica dust lofting is measured with a high number of observations, and most of the particles are launched within the estimated range for the simple case.
2. Increased packing density reduces the number of the lofted dust grains; however, their vertical launching velocities are increased due to the higher potential energy built-up between the strongly attached dust particles. Therefore, the influence of decreased number of microcavities and the increased contact forces are demonstrated.
3. A strong horizontal electric field contributes to the dust release from the surface, which could help to explain two peaks for the dust detections by the LEAM instrument on Apollo 17 near the lunar terminator before and after the terminator passage, where strong horizontal electric fields are previously predicted. The current results suggest lower launching velocities than the previous cases. Therefore, it shows the rolling and colliding particles help to cancel the contact forces, and the charged grains can easily overcome the contact and gravity forces with the smaller potential energies within the microcavities.
4. Aggregates are lofted as well as the single particles, and some of them separated during the lofting motion. Therefore, the separation of charged dust grains on the flight can be an additional source for the smaller grains in the lunar exosphere.

According to the results, it can be said that the future observation of the LHG with a CubeSat mission requires detecting the forward-scattering of the sunlight at approximately 200 m altitude under the regular SW condition; however, the presence of CZL would potentially overlap with the LHG. Therefore, a high resolution could help to distinguish between these brightness sources. First, the symmetrical shape of the CZL could be distorted in the vicinity of the lunar surface by the presence of the LHG. Second, gradually changing brightness values could help to detect the contribution of the LHG near the lunar terminator surface. Third, the CZL would be blocked by the lunar horizon while the CubeSat descent to the lunar night; however, the LHG brightness would also diminish due to the increased scattering angle with

respect to the orbital position. Therefore, the sensitivity requirement in order to detect the LHG would be higher in this regard. Finally, the simulations suggest that Apollo observations could be possible under the upstream electrons with high temperatures and the SW-like plasma density.

6.2 Future Work

There are several physical factors to be investigated in the future experiments such as the varying surface cleanliness parameter due to baking in the vacuum condition, and other external forces including the mechanical vibrations and the low-velocity impacts.

A regolith dust can be lofted from an elastic deformation region of a micrometeorite impact (Popel et al., 2016; 2017) if it can be separated from the surface by overcoming the forces of gravity and contact (Fig. 6.1). According to the initial velocity, the surface electric field and the current charge of a dust grain, it can be transported to higher altitudes around an airless planetary body such as the Moon. A laser source is planned to simulate the micrometeorite impacts; however, focusing a laser less than 0.1 mm diameter is a challenging task on a dusty surface unlike a planar surface. If it cannot be achieved, the acoustic wave of the impact shock expansion will be studied in order to check the possibility of applying a similar physical effect with a vibration actuator.

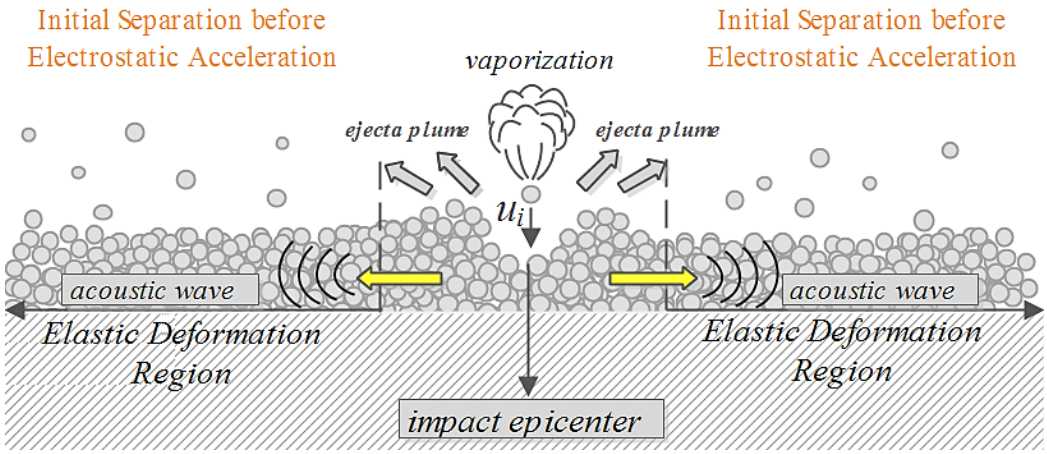

Figure 6.1 : Micrometeorite impact representation and the deformation regions.

For the laboratory experiments, we may provide a better dust detection technique by coding. Due to the planar focus of the microscopic telescope, it represents several challenges to the detection by the software without a human operator due to the

particle detections out of focus, varying light reflections, rotating particles with imperfect spherical shapes, rolling motion over a larger grain etc. Several approaches are already being investigated as vector quantization, clustering algorithms and neural networks.

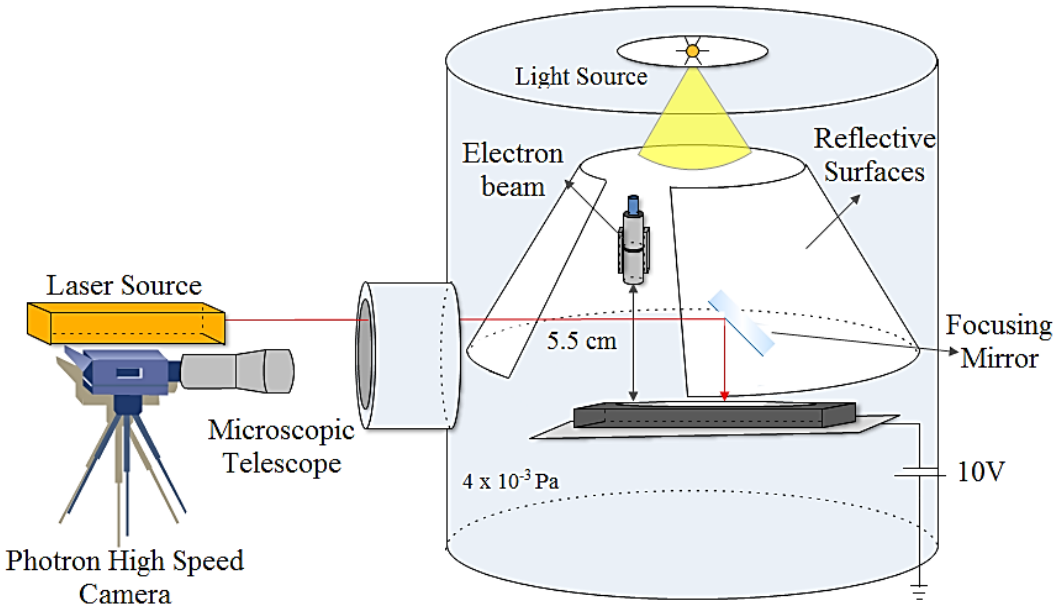

Figure 6.2 : Experiment setup to simulate the micrometeorite impacts.

REFERENCES

Asano, Y., Shinohara, I., Retino, A., Daly, P. W., Kronberg, E. A., Takada, T., Nakamura, R., Khotyaintsev, Y. V., Vaivads, A., Nagai, T., Baumjohann, W., Fazakerley, A. N., Owen, C. J., Miyashita, Y., Lucek, E. A. and Reme, H. Electron acceleration signatures in the magnetotail associated with substorms. *Journal of Geophysical Research: Space Physics*, 115(A5), 2010.

Berg, Otto E. A lunar terminator configuration. *Earth and planetary science letters*, 39(3):377–381, 1978.

Baumjohann, W., and Treumann, R. A. (1997). *Basic space plasma physics*. World Scientific.

Berg, O. E., Wolf, H. and Rhee, J., "2.2.4 lunar soil movement registered by the apollo 17 cosmic dust experiment", *International Astronomical Union Colloquium*, vol. 31, Cambridge University Press, 1976.

Brueckner, G. E., Delaboudiniere, J.-P., Howard, R. A., Paswaters, S. E., St. Cyr, O. C., Schwenn, R., Lamy, P., Simnett, G. M., Thompson, B. and Wang, D. Geomagnetic storms caused by coronal mass ejections (CMEs): March 1996 through June 1997. *Geophysical Research Letters*, 25(15):3019–3022, 1998.

Champlain, A., Mateo-Velez, J. C., Roussel, J.-F., Hess, S., Sarrailh, P., Murat, G., Chardon, J.-P. and Gajan, A. Lunar dust simulant charging and transport under UV irradiation in vacuum: Experiments and numerical modeling, Journal of Geophysical Research: Space Physics 121, 103-116, 2016.

Colwell, J. E., Batiste, S., Horányi, M., Robertson, S. and Sture, S. Lunar surface: Dust dynamics and regolith mechanics. *Reviews of Geophysics*, 45(2):RG2006, 2007.

Cooper, K., Gupta, A. and Beaudoin, S. Simulation of the adhesion of particles to surfaces. *Journal of colloid and interface science*, 234(2):284–292, 2001.

Criswell, D. R. Horizon-glow and the motion of lunar dust. *Photon and Particle Interactions with Surfaces in Space*, pages 545–556. Springer, 1973.

Denton, M. H. et al. "High speed solar wind streams–magnetospheric activity during prolonged driving" *EOS Trans., AGU* 89.7, pp. 62-63, 2008.

Farrell, W. M., Halekas, J. S., Killen, R. M., Delory, G. T., Gross, N., Bleacher, L. V., Krauss-Varben, D., Travnicek, P., Hurley, D., Stubbs, T. J. and Zimmerman, M. I. and Jackson, T. L. Solar-Storm/Lunar Atmosphere Model (SSLAM): An overview of the effort and description of the driving storm environment. *Journal of Geophysical Research: Planets*, 117(E10), 2012.

Farrell, W. M., Poppe, A. R., Zimmerman, M. I., Halekas, J. S., Delory, G. T. and Killen, R. M. The lunar photoelectron sheath: A change in trapping efficiency during a solar storm. *Journal of Geophysical Research: Planets*, 118(5):1114–1122, 2013.

Feldman, P. D., Glenar, D. A., Stubbs, T. J., Retherford, K. D., Gladstone, G. R., Miles, P. F., Greathouse, T. K., Kaufmann, D. E., Parker, J. W. and Stern, S. A. Upper limits for a lunar dust exosphere from far-ultraviolet spectroscopy by LRO/LAMP. *Icarus*, 233:106–113, 2014.

Freeman, J. W. and Ibrahim, M. Lunar electric fields, surface Potential and Associated Plasma Sheaths. *The Moon*, 14(1):103–114, 1975.

French, B. M., Heiken, G., Vaniman, D. and Schmitt, J. *Lunar sourcebook: A user's guide to the Moon*. CUP Archive, 1991.

Glenar, D. A., Stubbs, T. J., Hahn, J. M. and Wang, Y. Search for a high-altitude lunar dust exosphere using Clementine navigational star tracker measurements. *Journal of Geophysical Research: Planets*, 119(12):2548–2567, 2014.

Glenar, D. A., Stubbs, T. J., McCoy, J. E. and Vondrak, R. R. A reanalysis of the Apollo light scattering observations, and implications for lunar exospheric dust. *Planetary and Space Science*, 59(14):1695–1707, 2011.

Goertz, C. Dusty plasmas in the solar system. *Reviews of Geophysics*, 27(2):271–292, 1989.

Halekas, J. S., Delory, G. T., Lin, R. P., Stubbs, T. J. and Farrell, W. M. Lunar surface charging during solar energetic particle events: Measurement and prediction. *Journal of Geophysical Research: Space Physics*, 114(A5), 2009.

Halekas, J.S., Saito, Y., Delory, G.T. and Farrell, W.M. New views of the lunar plasma environment. *Planetary and Space Science*, 59(14):1681–1694, 2011.

Halekas, J.S., Delory, G.T., Lin, R.P., Stubbs, T.J. and Farrell, W. Lunar Prospector observations of the electrostatic potential of the lunar surface and its response to incident currents. *Journal of Geophysical Research: Space Physics*, 113(A9), 2008.

Harada, Y., Machida, S. Halekas, J.S., Poppe, A. R. and McFadden, J. P. ARTEMIS observations of lunar dayside plasma in the terrestrial magnetotail lobe. *Journal of Geophysical Research: Space Physics*, 118(6):3042–3054, 2013.

Hartzell, C. M., Farrell, W. and Marshall, J. Shaking as means to detach adhered regolith for manned Phobos exploration. *Advances in Space Research*, 2017.

Hartzell, C. M. and Scheeres, D. J. The role of cohesive forces in particle launching on the Moon and asteroids. *Planetary and Space Science*, 59(14):1758–1768, 2011.

Heiken, G., Vaniman, D. and French, B. M. *Lunar sourcebook: A user's guide to the Moon*. CUP Archive, 1991.

Horányi, M., Szalay, J.R., Kempf, S, Schmidt, J., Grün, E., Srama, R. and Sternovsky, Z. A permanent, asymmetric dust cloud around the Moon. *Nature*, 522(7556):324–326, 2015.

Jaffe, L. D. Depth of the lunar dust. *Journal of Geophysical Research*, *70*(24), 6129-6138, 1965.

Lianghai, X., Lei, L., Yiteng, Z. and De Zeeuw, D. L. SCIENCE CHINA Three-dimensional MHD simulation of the lunar wake. 56(2):330–338, 2013.

Manka, R. H. Plasma and Potential at the Lunar Surface. pages 347–361. Springer Netherlands, 1973.

McCoy, J. E. Photometric studies of light scattering above the lunar terminator from Apollo solar corona photography. *Lunar and Planetary Science Conference Proceedings*, pages 1087–1112, 1976.

McKay, D. S. et al. "JSC-1: A new lunar soil simulant." *Engineering, construction, and operations in space IV* 2, pp. 857-866, 1994.

Miyake, Y., Funaki, Y., Nishino, M.N. and Usui, H. Particle simulations of electric and dust environment near the lunar vertical hole. *AIP Conference Proceedings*, number 1, pages 020001, 2018. AIP Publishing.

Möstl, C., Amla, K., Hall, J.R., Liewer, P.C., De Jong, E.M., Colaninno, R.C., Veronig, A.M., Rollett, T., Temmer, M., Peinhart, V. and Davies, J.A., 2014. Connecting speeds, directions and arrival times of 22 coronal mass ejections from the Sun to 1 AU. *The Astrophysical Journal*, *787*(2), p.119.

Noble, S. "The Lunar Regolith." (2009), https://ntrs.nasa.gov/archive/nasa/casi.ntrs.nasa.gov/20090026015.pdf

Orger, N. C., Cordova-Alarcon, J. R., Toyoda, K. and Cho, M. Investigation of Electrostatic Transportation of Lunar Dust Grains due to Ambient Plasma Conditions. *JAXA Special Publication: Proceedings of the 14th Spacecraft Environment Symposium Aerospace Exploration Agency Special*, pages 59-62, 2018.

Orger, N. C., Cordova-Alarcon, J. R., Toyoda, K. and Cho, M. Lunar Surface Charging and Electrostatic Lofting of Lunar Dust Particles under Different Solar Wind Conditions and Solar Ultraviolet Radiation. *JAXA Special Publication: Proceeding of the 13th Spacecraft Environment Symposium*, pages 81, 2017.

Park, J. S., Liu, Y., Kihm, K. D. and Taylor, L. A. Micro-morphology and toxicological effects of lunar dust. *37th Annual Lunar and Planetary Science Conference*, 37, 2006.

Perko, H. A., Nelson, J. D.,Sadeh, W. Z. Surface cleanliness effect on lunar soil shear strength. *Journal of geotechnical and geoenvironmental engineering*, 127(4):371–383, 2001.

Pieters, C. M. et al. "Space weathering on airless bodies: Resolving a mystery with lunar samples", *Meteoritics & Planetary Science* 35.5, pp. 1101-1107, 2000.

Popel, S.I., Lisin, E.A., Izvekova, Y.N., Atamaniuk, B., Dolnikov, G.G., Zakharov, A.V. and Zelenyi, L.M.. Meteoroid impacts and dust particles in near-surface lunar exosphere. In *Journal of Physics: Conference Series Journal of Physics: Conference Series*, 774(1):012175, 2016.

Poppe, A. R., Samad, R., Halekas, J. S., Sarantos, M., Delory, G. T., Farrell, W. M., Angelopoulos, V. and McFadden, J. P. ARTEMIS observations of lunar pick-up ions in the terrestrial magnetotail lobes. *Geophysical Research Letters*, 39(17), 2012.

Poppe, A. and Horányi, M. Simulations of the photoelectron sheath and dust levitation on the lunar surface. *Journal of Geophysical Research: Space Physics*, 115(A8), 2010.

Rennilson, J. J. and Criswell, D. R. Surveyor observations of lunar horizon-glow. *The Moon*, 10(2):121–142, 1974.

Schwan, J., Wang, X., Hsu, H.W., Grün, E. and Horányi, M. The charge state of electrostatically transported dust on regolith surfaces. *Geophysical Research Letters*, 44(7):3059–3065, 2017.

Severny, A. B., Terez, E. I., and Zvereva. A. M., "The measurements of sky brightness on Lunokhod-2", *The Moon* 14.1, pp. 123-128, 1975.

Sheeley, N. R., Walters, J. H., Wang, Y.M. and Howard, R. A. Continuous tracking of coronal outflows: Two kinds of coronal mass ejections. *Journal of Geophysical Research: Space Physics*, 104(A11):24739–24767, 1999.

Sheridan, T. E., Goree, J., Chiu, Y. T., Rairden, R. L. and Kiessling, J. A.. Observation of dust shedding from material bodies in a plasma. *Journal of Geophysical Research: Space Physics*, *97*(A3), 2935-2942, 1992.

Sickafoose, A. A., Colwell, J. E., Horányi, M. and Robertson, S., Experimental levitation of dust grains in a plasma sheath. *Journal of Geophysical Research: Space Physics*, *107*(A11), SMP-37, 2002.

Singer, S. F. and Walker, E. H. Electrostatic dust transport on the lunar surface. *Icarus*, *1*(1-6), 112-120, 1962.

Stubbs, T.J., Farrell, W.M., Halekas, J.S., Burchill, J.K., Collier, M.R., Zimmerman, M.I., Vondrak, R.R., Delory, G.T. and Pfaff, R.F. Dependence of lunar surface charging on solar wind plasma conditions and solar irradiation. *Planetary and Space Science*, 90:10–27, 2014.

Stubbs, T. J.,Vondrak, R. R. and Farrell, W. M. A dynamic fountain model for lunar dust. *Advances in Space Research*, 37(1):59–66, 2006.

Szalay, J. R. and Horányi, M. The search for electrostatically lofted grains above the Moon with the Lunar Dust Experiment. *Geophysical Research Letters*, 42(13):5141–5146, 2015.

Tsurutani, B. T. and Lakhina, G. S. An extreme coronal mass ejection and consequences for the magnetosphere and Earth. *Geophysical Research Letters*, 41(2):287–292, 2014.

Vaverka, J., Richterová, I., PavluËš, J., Šafránková, J. and Němeček, Z. Lunar Surface and Dust Grain Potentials during the Earth's Magnetosphere Crossing. *The Astrophysical Journal*, 825(2):133, 2016.

Walbridge, E.W. On "Photoelectric screening of bodies in interplanetary space". *Icarus*, 10(2):342–343, 1969.

Wang, X., Horányi, M. and Robertson, S. Experiments on dust transport in plasma to investigate the origin of the lunar horizon glow. *Journal of Geophysical Research: Space Physics*, *114*(A5), 2009.

Wang, X., Schwan, J., Hsu, H.W., Grün, E. and Horányi, M. Dust charging and transport on airless planetary bodies. *Geophysical Research Letters*, 43(12):6103–6110, 2016.

Whipple, E C. Potentials of surfaces in space. *Reports on Progress in Physics*, 44(11):1197–1250, 1981.

Xie, L., Li, L., Zhang, Y., Feng, Y., Wang, X., Zhang, A. and Kong, L. Three-dimensional Hall MHD simulation of lunar minimagnetosphere: General characteristics and comparison with Chang'E-2 observations. *Journal of Geophysical Research: Space Physics*, 120(8):6559–6568, 2015.

Vyshlov, A. S., "Preliminary results of circumlunar plasma research by the Luna 22 spacecraft", *Space research XVI*, 1976.

Zhang, J., Dere, K. P., Howard, R. A., Kundu, M. R. and White, S. M. On the Temporal Relationship between Coronal Mass Ejections and Flares. *The Astrophysical Journal*, 559(1):452–462, 2001.

Zimmerman, M.I., Farrell, W.M., Hartzell, C.M., Wang, X., Horányi, M., Hurley, D.M. and Hibbitts, K. Grain-scale supercharging and breakdown on airless regoliths. *Journal of Geophysical Research: Planets*, 121(10):2150–2165, 2016.